

AD-A179 794

LASER CLADDING OF NI+CR+AL+RARE EARTH ALLOYS FOR  
IMPROVED OXIDATION AND H. (U) ILLINOIS UNIV AT URBANA  
DEPT OF MECHANICAL AND INDUSTRIAL ENG.

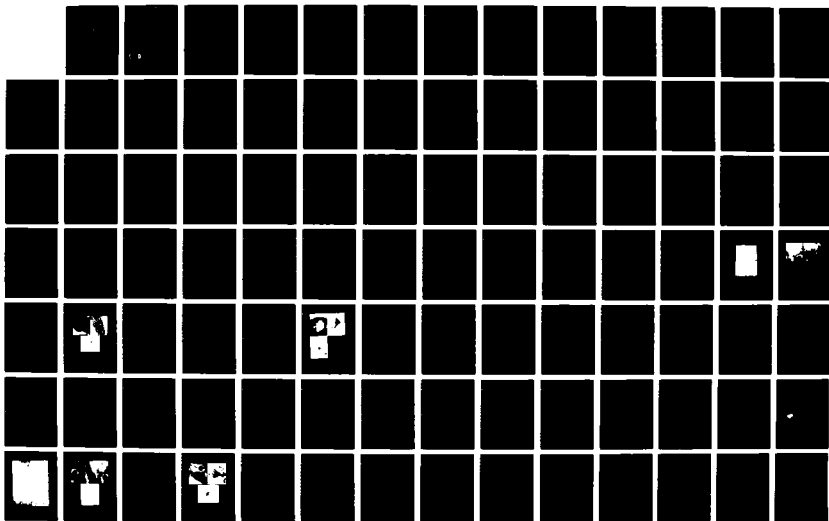
1/2

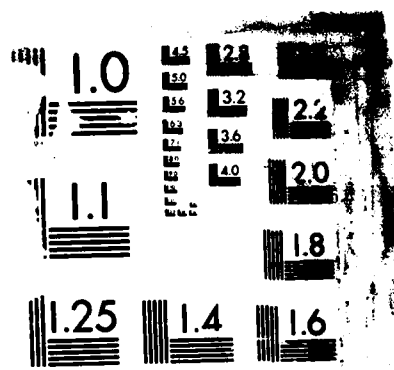
UNCLASSIFIED

J HAZUMDER ET AL. NOV 86 AFOSR-TR-87-0434

F/G 11/6

NL





MI

**Laser Aided Materials Processing Laboratory  
Department of Mechanical and  
Industrial Engineering  
University of Illinois at  
Urbana-Champaign  
Urbana, IL 61801**



**AD-A179 794**

**Annual Progress Report  
(November 1985 through November 1986)**

Approved for public release;  
distribution unlimited.

**LASER CLADDING OF Ni+Cr+Al+RARE EARTH  
ALLOYS FOR IMPROVED OXIDATION  
AND HOT CORROSION**

Approved for public release;  
NOTICE OF REPRODUCTION  
this technical report is hereby  
approved  
distribution  
unlimited

**Contract No. AFOSR 85-0333  
submitted to  
Air Force Office of Scientific Research  
Building 410  
ATTN: Dr. A. Rosenstein and Maj. J. Hagar  
Bolling Air Force Base  
Washington, DC 20332**

**DTIC  
ELECTE  
APR 29 1987  
S D**

**submitted by**

**J. MAZUMDER, A. KAR,  
AND J. SINGH**

## REPORT DOCUMENTATION PAGE

1a. REPORT SECURITY CLASSIFICATION UNCLASSIFIED		1b. RESTRICTIVE MARKINGS	
2a. SECURITY CLASSIFICATION AUTHORITY		3. DISTRIBUTION/AVAILABILITY OF REPORT Unlimited Distribution	
2b. DECLASSIFICATION/DOWNGRADING SCHEDULE			
4. PERFORMING ORGANIZATION REPORT NUMBER(S)		5. MONITORING ORGANIZATION REPORT NUMBER(S) AFOSR-TN- 87-0434	
6a. NAME OF PERFORMING ORGANIZATION University of Illinois	6b. OFFICE SYMBOL (If applicable)	7a. NAME OF MONITORING ORGANIZATION AFOSR	
6c. ADDRESS (City, State and ZIP Code) Dept of Mechanical & Industrial Engineering 1206 West Green St Urbana Illinois 61801		7b. ADDRESS (City, State and ZIP Code) Bolling AFB Wash DC 20332	
8a. NAME OF FUNDING/SPONSORING ORGANIZATION AFOSR	8b. OFFICE SYMBOL (If applicable) NE	9. PROCUREMENT INSTRUMENT IDENTIFICATION NUMBER AFOSR-85-0333	
8c. ADDRESS (City, State and ZIP Code) same as 7b		10. SOURCE OF FUNDING NOS.	
		PROGRAM ELEMENT NO. 61102F	PROJECT NO. 2306
		TASK NO. A2	WORK UNIT NO.
11. TITLE (Include Security Classification) Laser Cladding of Ni+Cr+Al+Rare Earth Alloys		12. PERSONAL AUTHOR(S) Mazumder for Improved Oxidation & Hot Corrosion	
13a. TYPE OF REPORT Annual	13b. TIME COVERED FROM 11/85 TO 11/86	14. DATE OF REPORT (Yr. Mo., Day)	15. PAGE COUNT
16. SUPPLEMENTARY NOTATION			
17. COSATI CODES		18. SUBJECT TERMS (Continue on reverse if necessary and identify by block number)	
FIELD	GROUP	SUB. GR.	
19. ABSTRACT (Continue on reverse if necessary and identify by block number) Alloys and coatings for alloys for improved high temperature service life under aggressive atmosphere are of great contemporary interest. There is a general consensus that addition of reactive elements such as <sup>Hafnium</sup> Hf will provide many beneficial effects for such alloys. The laser cladding technique was used to produce <sup>VICKI IRON CHROME ALUMINUM HAFNIUM</sup> Ni-Fe-Cr-Al-Hf alloys. The laser cladding technique was used to produce Ni-Fe-Cr-Al-Hf alloys with extended solid solution of Hf. A 10 kW <sup>CO<sub>2</sub> LASER</sup> laser with mixed powder feed was used for laser cladding. Optical, scanning electron <sup>SEM</sup> (SEM) and scanning transmission electron (STEM) microscopy were employed for microstructural evolution of alloys produced during laser cladding processes. The electron probe microanalysis and the auger electron spectroscopy were also used for micro-chemical analysis of different phases. Microstructural studies revealed a high degree of grain refinement, considerable increase in solubility of Hf in matrix and Hf rich precipitates and new metastable phases. This paper will report the microstructural development in this laser clad Ni-Fe-Cr-Al-Hf alloy. <sup>RARE EARTH ELEMENTS</sup>			
20. DISTRIBUTION/AVAILABILITY OF ABSTRACT UNCLASSIFIED/UNLIMITED <input checked="" type="checkbox"/> SAME AS RPT <input type="checkbox"/> OTIC USERS <input type="checkbox"/>		21. ABSTRACT SECURITY CLASSIFICATION UUUU	
22a. NAME OF RESPONSIBLE INDIVIDUAL Dr. Alan Rosenstein		22b. TELEPHONE NUMBER (Include Area Code) 767-4931	22c. OFFICE SYMBOL NE

LASER CLADDING OF Ni+Cr+Al+RARE EARTH ALLOYS  
FOR IMPROVED OXIDATION AND HOT CORROSION

J. Mazumder, A. Kar, and J. Singh  
Laser Aided Materials Processing Laboratory  
Department of Mechanical and Industrial Engineering  
1206 West Green Street  
University of Illinois  
Urbana, IL 61801

Progress Report for the Period  
November 1985 through November 1986

Contract No. AFOSR 85-0333

Submitted to  
Air Force Office of Scientific Research

Attn: Dr. A. Rosenstein and Major J. Hagar



Accession For	
NTIS CRA&I	<input checked="checked" type="checkbox"/>
DTIC TAB	<input type="checkbox"/>
Unannounced	<input type="checkbox"/>
Justification	
By	
Distribution /	
Availability Codes	
Dist	Avail and/or Special
A-1	

## SUMMARY

This report summarizes experimental and theoretical studies carried out during the period of November 1985 to November 1986 on laser cladding using a quaternary mixture of nickel, chromium, aluminum and hafnium. The laser clad region has been studied to determine the distribution of undissolved hafnium and hafnium-rich precipitates. Also, the solid solution obtained during laser cladding has been examined to determine the extension of solubility of hafnium in nickel. Because of inherent rapid cooling during laser cladding process, many metastable hafnium-rich phases are formed. These phases have also been studied in this work.

Microstructural evolution of Ni-Cr-Al-Hf clad on AISI 1016 substrate is accepted for publication by Acta Metallurgica. Similar work in IN718 substrate is published in the Proceedings of the "High Temperature Coating" conference held at TMS-AIME 1986 Fall Meeting. Another paper on IN 718 with oxidation data is submitted to the Journal of High Temperature Technology.

For determining the composition of extended solid solution formed due to rapid cooling in laser cladding a mathematical model is presented. This model considers diffusion mechanism for mass transport in a one-dimensional semi-infinite molten pool of the cladding material, from which heat is removed by conduction through a one-dimensional semi-infinite solid substrate. The rate of solidification has been obtained by modeling the cooling process as a composite medium heat transfer problem. The discontinuity of the concentration field has been simulated using a nonequilibrium partition coefficient and then a non-similar exact solution for the mass transport equation has been obtained using a set of similarity variables which can be derived using Lie group theory. Two papers are published on this work; one will appear in the J. of Metals, February 1987 and the other in the J. Appl. Physics, April 1987 issue.

# TABLE OF CONTENTS

	Page
I. INTRODUCTION.....	1
A. Literature Review.....	1
B. Objectives.....	3
II. EXPERIMENTAL STUDIES.....	5
A. Experimental Procedure.....	5
B. Results and Discussion.....	7
III. MATHEMATICAL MODEL.....	11
A. Introduction.....	11
B. Problem Formulations.....	14
C. Method of Solution.....	17
D. Results and Discussion.....	22
IV. CONCLUSIONS.....	24
A. Current Works.....	24
B. Plans for Future Works.....	25
APPENDIX I LASER CLADDING OF Ni-Cr-Al-Hf ON AISI 1016 SUBSTRATE...	29
APPENDIX II LASER CLADDING OF Ni-Cr-Al-Hf ON IN 718 SUBSTRATE.....	58
APPENDIX III MODEL OF DIFFUSION IN LASER CLADDING.....	84

## I. INTRODUCTION

### A. Literature Review

Structural alloys requiring exposure to an aggressive atmosphere at elevated temperature often need protective coatings for oxidation resistance to achieve enhanced service lifetime. M+Cr+Al+RE (M = Ni, Fe, Co; RE = Reactive Elements) systems are widely used for such coatings. These coatings tend to form  $\text{Al}_2\text{O}_3$  rich scales. The  $\text{Al}_2\text{O}_3$  is the protective coating of choice [1,2] since 1) diffusion through the oxide scale is very slow, 2) volatility is limited, 3) growth kinetics is slow, and 4) it is relatively inert in a high temperature oxidation environment.

However, the adhesion of  $\text{Al}_2\text{O}_3$  to the substrate is poor. Attempts to improve the adhesion have largely centered on the reactive element (RE) effect. Y or Hf are mainly used to improve the adherence of  $\text{Al}_2\text{O}_3$  scale on the M Cr Al Y or MCrAlHf alloys and coatings. There are various mechanisms proposed by various authors regarding the beneficial effect of RE addition to MCrAl alloys. Some of these are listed below.

1. The formation of mechanical "pegs" which anchor the scale to the substrate metal alloy [1,3],
2. The rare earth dispersoids provide alternative vacancy coalescence sites and thus prevent the vacancy coalescence at the scale-metal interface [4],
3. Increased bonding forces are formed between the scale and substrate through preferential segregation of the reactive elements at the interface [3],
4. The interaction with trace elements such as sulfur forming refractory phases and thus limiting the sulfur segregation at the scale-substrate interface [2],
5. The reduction of scale growth processes [5],



6. The enhancement of scale plasticity by structure modification [6],
7. The reduction of thermomechanical differences between the scale and the substrate by the formation of graded oxide layers [7], and,
8. Refractory metal (e.g. Re) addition to nickel superalloys inhibits the  $\gamma'$  coarsening process and thus results in higher temperature capabilities [8].

Although there are controversies regarding which particular mechanism or groups of mechanisms are responsible for improved high temperature properties, there is a general consensus that the addition of reactive metals improves the high temperature service life and that they perform best when they are in a finely dispersed form.

Using conventional techniques, it is very difficult to incorporate RE elements in finely dispersed form above 1 wt. percent, which is the solid solubility limit [9]. The inherent rapid heating and cooling rate in laser processing can be effectively used to produce an alloy with extended solid solution and uniform distribution of phases [10-13]. The laser cladding technique was used to produce Ni-Fe-Cr-Al-Hf alloy with high Hf contents compared with alloys produced by conventional techniques such as plasma spraying of prealloyed powders. This is a technique where a mechanical mixture of powders of choice is delivered into a laser melted pool and solidified rapidly [10,11,14]. The increase in solid solubilities of the alloying elements with RE depends upon the processing conditions for laser cladding. The main variables during laser processing are laser power, size and shape of laser beams, scan velocity and the chemistry and metallurgy of the substrate. The overall composition and microstructure of the laser clad materials was also determined by the degree of mixing and cooling rate. For determining the effects of various laser processing conditions and to understand the process physics of laser cladding mathematical modeling was also done.

During laser cladding the alloy is formed at the surface at a non-equilibrium cooling rate. There are not very many theoretical studies published in the literature to model laser surface cladding and alloying at a nonequilibrium cooling rate. A three-dimensional heat transfer model for CW laser material processing was developed by Mazumder and Steen [15]. Convection arising due to surface tension in a laser melted pool was considered by Chan, et al. [16]. They studied its effect on surface velocity, surface temperature, pool shape, and the cooling rate. The distribution of matter by diffusion and convection, after it is delivered to such a pool was examined by Chande and Mazumder [13]. There has also been some efforts to predict the formation of extended solid solution under rapid cooling using thermodynamic variables such as free energy and chemical potential. The thermodynamic approach to solidification has been examined very well by Baker and Cahn [17]. Boettinger and Perepezko [18] have discussed the process of rapid solidification from the point of view of thermodynamics. Boettinger et al. [19] have used the response function approach of Baker and Cahn [17] and stability analysis for microsegregation-free solidification. More about rapidly solidified materials can be found in Refs. [14,20]. The mathematical model of the present study is concerned with the determination of composition of the extended solid solution formed due to rapid cooling in laser cladding using space-time variable approach.

## B. Objectives

The objectives of the project for which this report is prepared are to develop Ni-based superalloys of Ni-Cr-Al-Hf with a maximum solid solubility of Hf in it by laser cladding technique in order to generate stable and protective films which should provide improved oxidation resistance. It is also

expected that these alloys with extended solid solution of Hf will increase the high temperature stability by retarding the  $\gamma'$  coarsening kinetics and provide fine precipitates and thus improve the intermediate and high temperature strength.

In order to understand the high temperature service behavior of these alloys, it is necessary to know about the crystal structure, stability and chemical composition of the different phases developed during the laser cladding process and correlate this structure with the laser processing conditions. Moreover, to the best of the authors' knowledge nobody has reported the microstructure evolution of the rapidly solidified Ni-Fe-Cr-Al-Hf alloy with extended solid solution of Hf.

Besides these, the goal of the present work is to develop mathematical model to study the effects of various laser processing conditions on the extension of solid solubility observed during laser cladding. These objectives include the following:

(i) Effect of

- (a) Laser power
- (b) Laser beam diameter
- (c) Laser-cladding interaction time
- (d) Cladding thickness
- (e) Cladding powder feed rate
- (f) Cooling rate
- (g) Speed of the substrate relative to the laser beam
- (h) Convection in the cladding melt

on the extension of solid solubility in the cladding alloy.

(ii) Development of nonequilibrium phase diagrams.

## II. EXPERIMENTAL STUDIES

### A. Experimental Procedure

Three different substrates (AISI 1016, Inconel 718 and GTD111 a modified version of Rene-80) were used for laser cladding. Ni, Cr, Al, and Hf powders in the ratio of 10:5:1:1 were used as mixed powder feed for cladding. The size of Ni, Cr, Al powder was about 5  $\mu\text{m}$  in diameter whereas Hf powder was of 44  $\mu\text{m}$  in maximum diameter. The average chemical analysis of the laser clad region was found by electron probe micro analysis to be 70% Ni, 10% Cr, 10% Fe, 5% Al, and 5% Hf (all in weight percents). The cladding treatments were carried out using an AVCO HPL 10 kW CW  $\text{CO}_2$  laser with F7 cassegrain optics (as shown in Fig. 1(a)). The laser was operated in the  $\text{TEM}_{01}^*$  mode\*. The beam focused by cassegrain optics was reflected downward toward the substrate by a flat mirror. The laser was operated at the range of 5 to 9 kW. Specimens (approximately 6.4 mm thick) were traversed relative to the laser beam at a speed of 6.35 to 25.4 mm per second. The powder was delivered to the area of interaction by a pneumatic powder delivery system with a feed screw. The powder flow was regulated by varying the speed and changing the size of the feed screw. The flow rate for the present study was approximately 0.2 gm/second. Argon gas with a flow rate of 7.7 gm/sec was used to maintain a steady powder flow through the copper tubing leading to the substrate. Powder was placed on the substrate just prior to its contact with the laser.

A shielding of argon gas with a shielding box was used to minimize surface contamination during laser processing. The argon gas which directed the powder flow into the molten pool of substrate was also used in plasma suppression at the laser-substrate interaction point. The function of the

\*Donut-shaped laser beam with a Gaussian power distribution in the outer ring and none at the hole of the donut.

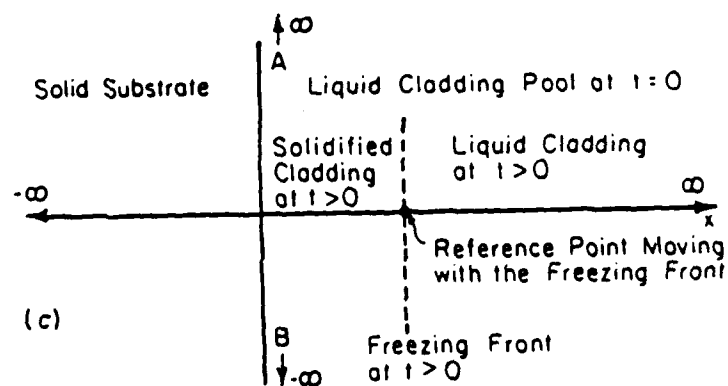
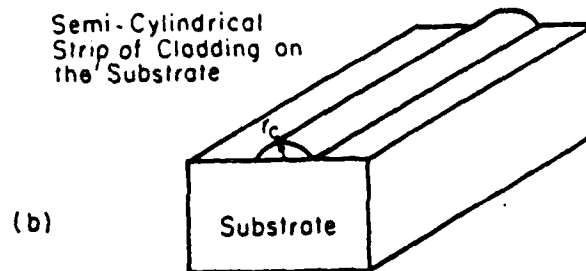
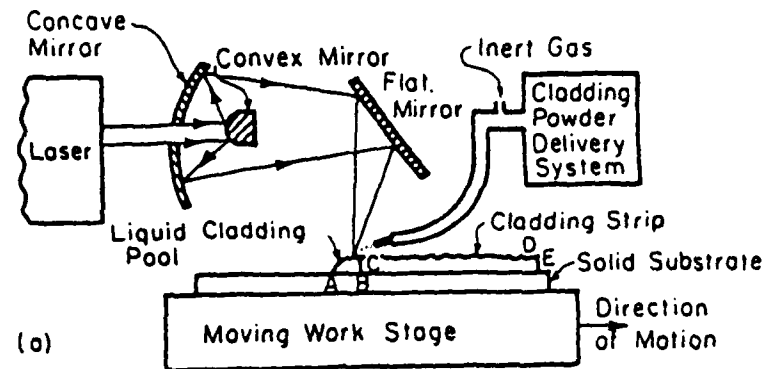


Figure 1(a) Schematic diagram of laser surface cladding

(b) Three-dimensional view of the cladding and the substrate

(c) Geometric configuration used in the present model. (The model substrate and the solidification of the model cladding have been shown after rotating the pool ABCA (see Fig. 1(a)) by 90 degrees clockwise)

shielding box was to provide the inert environment near the laser-substrate interaction point which also reduced clad porosity [10].

Microstructural observation of clad specimens was carried out by Auger electron spectroscopy, optical, and scanning electron microscopy. After mechanical and chemical polishing to a thickness of 0.3 mm, 3 mm discs were punched from the clad material. Specimens for the TEM observations were prepared by the jet polishing technique with an electrolyte of 200 c.c. 2-Butoxy-ethanol, 400 c.c. methanol, 50 c.c. perchloric acid at 35 volts with the electrolyte at a temperature of  $-15^{\circ}\text{C}$ . Samples were observed using a Phillips EM 430 microscope (equipped with an EDAX) operated at 300 kV.

## B. Results and Discussion

### Iron Substrate

Optical microstructure of the laser clad Ni-Cr-Al-Hf alloy has been studied in this work. It shows uniform distribution and formation of second phase in the laser clad matrix as well as at the grain boundaries. At low magnification it is difficult to resolve the undissolved Hf particles. The second phase appeared to be spherical in nature. The concentration of each of the elements (Ni, Cr, Al, Hf, Fe) in the laser clad region was found by the electron probe microanalysis. The concentration profile of each alloying element across the laser clad/substrate region was also determined and found to be uniform.

In order to see the presence and distribution of undissolved Hf in the laser clad region, Scanning Electron Microscopy (SEM) was carried out. The SEM micrograph shows undissolved Hf particles dispersed throughout the matrix and also few at grain boundaries. The undissolved Hf particles were confirmed by the SEM x-ray microanalysis and this is discussed in the next section.

To see the detailed internal structure of the laser clad region, STEM investigation was carried out. A general survey of the thin foils shows uniformly distributed undissolved Hf particles of 1 to 9  $\mu\text{m}$  size, and Hf-rich precipitates in the nickel rich matrix containing high density of dislocations and  $\gamma'$  precipitates. STEM microanalysis from the undissolved Hf revealed only Hf peaks.

The size and volume of the  $\gamma'$  precipitates in  $\gamma$  matrix depend upon the laser processing conditions i.e. cooling rates. There is linear increase in the size of  $\gamma'$  precipitates with increasing laser power for a constant traverse speed. Similarly, the volume fraction of the  $\gamma'$  precipitate increases with increase in laser power. The volume fraction of  $\gamma'$  precipitate is higher at low traverse speed as compared with high traverse speed for a given set of laser power. This could be explained on the basis of laser beam interaction time with the alloy, i.e. rate of cooling during rapid solidification. For a given laser beam diameter, there would be less interaction time for an alloy made at a traverse speed of 14.8 mm/s as compared with an alloy made at a traverse speed of 6.25 mm/s. Therefore, the rate of cooling would be faster in the former case (14.8 mm/s) as compared with the latter case (6.35 mm/s).

At this stage it is difficult to comment about the solid solubility of Fe in the matrix and of Hf in the  $\gamma'$  phase as the precipitates were very small. But, it has been found that by increasing the cooling rates (particularly in laser processing technique), there was an increase in solid solubility of the alloying additions in the matrix as well as in the precipitates. The cooling rates attainable by this process are known to enhance elemental homogeneity and to extend, in some cases, elemental concentrations in the alloy beyond the normal saturation limits of the equilibrium phase

diagrams. Furthermore, under normal rapid quenching of Ni-based superalloys (e.g., Ni-Cr-Al), the  $\gamma'$  precipitation could only be seen after suitable long aging heat treatments. In spite of a high cooling rate ( $\sim 10^5$ °C/s) occurred during laser cladding process,  $\gamma'$  precipitates have been observed in the laser clad Ni-Cr-Al-Hf alloys. It clearly indicates that the addition of Hf to the Ni-Cr-Al alloy enhances the activation energy or driving force for the precipitation of  $\gamma'$  precipitates. The volume fraction of  $\gamma'$  precipitation depends upon the solid solubility of Hf in the matrix. Thus, the initial size and volume fraction of  $\gamma'$  precipitates and increase in solid solubility of Fe and Hf have an influence on the oxidation resistance properties. On the basis of STEM microanalysis of the matrix, the possible composition of  $\gamma'$  precipitates would be  $(\text{Ni, Cr, Fe})_3(\text{Al, Hf})$ .

The general survey of the thin foil from the laser clad samples (under different laser processing conditions) shows the formation of many unknown meta-stable phases with different microchemistry. Since the equilibrium phase diagram for this quaternary Ni-Cr-Al-Hf is not available, and the volume fraction of each phase developed was very small, there is difficulty in identifying each of the phases.

The size of the undissolved Hf particles varied from 0.5  $\mu\text{m}$  to 10  $\mu\text{m}$  in diameter depending on the traverse speed and laser power. The undissolved Hf particle size increases with traverse speed and laser power. It is expected that the undissolved Hf particle size will be higher for higher speed since increased speed leads to decreased interaction time. Interaction time is critical for dissolution of high melting point (2423°K) material such as Hf. The increase of undissolved Hf particle diameter with the increase of power is not obvious. However, this can be explained on the basis of specific energy input for laser cladding [14]. For constant traverse speed and powder feed-



rate, increased power leads to slower cooling rate which results in reduced surface tension driven convection [16]. Mass transport in laser surface modification with mixed powder feed depends primarily on convection [13]. Therefore reduced convection will cause reduced dissolution leading to higher undissolved Hf particle size. Scatter in particle size distribution data is also higher for higher laser power. This is because of the fact that higher power increases the width of the molten pool [16,21] resulting in a wide range of cooling rates depending on the position in the pool. This variation of cooling rate also leads to variation of undissolved Hf particle size due to variation of convection. Similar studies have been carried out for Inconel 718 substrate. For details and micrographs of these studies see the Ref. [22] for Iron substrate and Ref. [31] for IN 718 substrate. They are enclosed on APPENDICES I and II, respectively.

### III. MATHEMATICAL MODEL

#### A. Introduction

The physical process of laser cladding involves pouring of cladding material powder onto the substrate to be clad by using a powder delivery system and simultaneously melting the powder using a laser beam. The pool of the cladding melt which is formed just below the laser beam solidifies by losing heat to the surrounding air, adjacent cladding and the solid substrate as it moves away from the laser beam due to the motion of the substrate. This produces a layer of cladding on the solid substrate and a liquid cladding pool below the laser beam (see Fig. 1(a)). Figure 1(a) shows an experimental set-up for laser surface cladding. The area ABCA shows the liquid pool of cladding melt which is in contact with the solid substrate along AB. It is also in contact along BC with the cladding formed on the substrate and the portion CA of the pool is exposed to an inert atmosphere to avoid oxidation of the cladding material. The shape of the strip of cladding will depend on the properties and the temperature of the cladding melt and the substrate, relative motion of the cladding with respect to the substrate and the characteristics of the cladding powder delivery system. In the present model the strip of cladding BCDEB (see Fig. 1(a)) has been considered to have semi-cylindrical shape (see Fig. 1(b)) and based on this the cladding radius ( $r_c$ ) is determined (see Eq. (18)). This paper is concerned with heat and mass transfer in the cladding melt ABCA to model extended solid solution during laser cladding. This liquid pool solidifies by conducting away heat to the substrate and to the solid cladding across AB and BC, respectively. Also, it loses some energy to the ambient inert gas across the free surface CA. But the loss of energy to the inert gas across the surface CA will be smaller than the heat loss due to conduction in the substrate and the cladding BCDEB.

However, the cladding BCDEB is formed from the liquid cladding melt just solidified and hence its temperature distribution is almost uniform and much higher than the temperature of the substrate which is immediately below the pool ABCA. So the heat loss across BC is much less compared to that across AB. Therefore, we can consider that the pool of cladding melt (ABCA) loses energy only in one direction through the surface at AB and to simplify the heat transfer calculations we assume that the pool extends up to infinity along AB as well as BC. Due to this assumption the cladding melt solidifies along AB and this freezing front moves upward in the direction of BC. The solid substrate has also been taken to be semi-infinite. The geometric configuration of this pool has been shown in Fig. 1(c) by rotating the pool 90 degrees in the clockwise direction. In this figure the freezing front has been shown to be planar. This is true when a pure metal solidifies. For a cladding melt of an alloy system, the freezing front develops curvature due to surface tension and also there could be dendrite and cellular growth at the solid-liquid interface. Moreover, rapid quenching may lead to growth due to spinodal decomposition and nucleation in the bulk of the liquid phase. The stability criterion of Mullins and Sekerka [23] of a planar interface during solidification of a dilute binary alloy shows that the planar interface will be unstable for both the nickel-hafnium and the nickel-aluminum systems considered in this study. It was found that there are dendritic growths for both cases, although the dendrites are less prominent for the nickel-aluminum alloy compared to those of nickel-hafnium system. Thus the solid-liquid interface for nickel-aluminum system can be considered planar. Also for those systems where the size of dendrites is extremely small, the interface can be taken to be planar. Nevertheless, the dendrites will affect the diffusion of solute atoms at the freezing front. To simplify the mass transfer analysis,

the freezing front has been assumed to be planar because the dendrite size is negligible for systems such as nickel-aluminum. Moreover, the trend predicted by the model is more important than the exact numerical values due to the paucity of high temperature materials data and simplifying assumptions. Besides this the present model has been developed based on a few more assumptions listed below.

- (1) The thermal conductivity and the thermal diffusivity for a mixture is the sum of the volume-averaged value of the respective transport properties of each element of the mixture,
- (2) The mass diffusivity of each element in the liquid phase is the average value of self-diffusivity over the room temperature and the initial temperature with modified activation energy for the mixture,
- (3) There is no diffusion of mass in the solid phase,
- (4) The solute segregated at the solid-liquid interface moves in the liquid phase by diffusion only,
- (5) The concentration of solute in the liquid alloy is equal to the nominal composition of the cladding powder mixture.
- (6) Change in solute concentration in the liquid phase does not alter its freezing point but it affects the heat flux across the solid-liquid interface, and
- (7) Only 50 percent of the laser energy has been assumed to be absorbed by the cladding material. Studies<sup>13</sup> show that the amount of laser energy absorbed by different materials is 37-60 percent.

Under these assumptions it is required to solve the one-dimensional heat conduction equation to obtain the speed of the freezing front which is then utilized to solve for the distribution of solute in the liquid phase. In

laser processing of material usually the laser beam or the workpiece moves at a certain speed and when the laser melted pool is fully developed the speed of the freezing front and that of the laser beam or the workpiece are identical. This eliminates the need for solving the energy transport equation to determine the speed of solidification for fully developed pool. In the case of laser surface alloying the solidification progresses with segregation of solute atoms from the solid to the liquid phase and this alters the concentration of solute at the solid-liquid interface. This will affect the speed of the freezing front as well as the freezing point of the liquid. To take the former effect into account the energy transport equation has been solved while the latter one has been ignored in this model.

#### B. Problem Formulations

The governing equations for energy transport are:

(i) Region 1 (solid substrate)

$$\frac{\partial^2 T_1}{\partial x^2} = \frac{1}{\alpha_1} \frac{\partial T_1}{\partial t}; \quad t \geq 0, \quad -\infty < x \leq 0 \quad (1)$$

(ii) Region 2 (solidified cladding)

$$\frac{\partial^2 T_2}{\partial x^2} = \frac{1}{\alpha_2} \frac{\partial T_2}{\partial t}; \quad t > 0, \quad 0 \leq x \leq S(t) \quad (2)$$

(iii) Region 3 (liquid cladding)

$$\frac{\partial^2 T_3}{\partial x^2} = \frac{1}{\alpha_3} \frac{\partial T_3}{\partial t}; \quad t \geq 0, \quad S(t) \leq x < \infty \quad (3)$$

Here  $T_1$ ,  $T_2$ , and  $T_3$  are the temperatures and  $\alpha_1$ ,  $\alpha_2$ , and  $\alpha_3$  are thermal diffusivities of regions 1, 2, and 3, respectively.  $S(t)$  is the location of the solid-liquid interface at time  $t$ . If  $k_1$ ,  $k_2$ , and  $k_3$  are taken to be thermal conductivities of the regions 1, 2, and 3, respectively and if the ambient temperature, the freezing point of the cladding melt and the initial cladding pool mean temperature are denoted by  $T_0$ ,  $T_m$ , and  $T_f$ , respectively then the auxiliary conditions for the above heat transfer problem can be written as

$$T_1(-\infty, t) = T_0 \quad (4a)$$

$$T_1(x, 0) = T_0 \quad (4b)$$

$$\frac{\partial T_1}{\partial x} = \frac{k_2}{k_1} \frac{\partial T_2}{\partial x} \text{ at } x = 0 \quad (4c)$$

$$T_1(0, t) = T_2(0, t) \quad (4d)$$

$$T_2(x, t) = T_3(x, t) = T_m \text{ at } x = S(t) \quad (4e)$$

$$k_2 \frac{\partial T_2}{\partial x} - k_3 \frac{\partial T_3}{\partial x} = \rho L \frac{dS}{dt} \text{ at } x = S(t) \quad (4f)$$

where  $\rho$  is the density of the cladding melt and  $L$  its latent heat of solidification. Note that the change in density due to solidification has been neglected here.

$$T_3(\infty, t) = T_f \quad (4g)$$

$$T_3(x,0) = T_f \quad (4h)$$

$$S(0) = 0 \quad (4i)$$

The amount of solute rejected by the solidifying cladding and its transport in the liquid phase are governed by the following diffusion equation.

$$\frac{\partial C}{\partial t} - \frac{\gamma\sqrt{\alpha_3}}{\sqrt{t}} \frac{\partial C}{\partial x} = D \frac{\partial^2 C}{\partial x^2} \quad (5)$$

where  $c$  is the concentration of solute in the liquid phase,  $D$  is the mass diffusion coefficient and  $\gamma$  is a root of the transcendental Eq. (12). If  $C_0$  is the initial concentration of solute in the liquid phase and  $k_e$  denotes the equilibrium partition coefficient at the solid-liquid interface then the auxiliary conditions for the above mass transfer problem are

$$C(x,0) = C_0 \quad (6a)$$

$$C(\infty,t) = C_0 \quad (6b)$$

$$D(1 + \frac{\gamma\sqrt{\alpha_3}}{\sqrt{t}} \beta) \frac{\partial C}{\partial x} = \frac{\gamma\sqrt{\alpha_3}}{\sqrt{t}} (k_e - 1)C \text{ at } x = 0 \quad (6c)$$

in a coordinate frame of reference moving with the solid-liquid interface. In the expression (6c),  $\beta = \lambda/D^*$ , where  $\lambda$  is the interatomic spacing and  $D^*$  is the inter-diffusivity. This expression is obtained by incorporating into the mass balance equation at the solid-liquid interface an expression for non-equilibrium partition coefficient derived by Aziz [25].

### C. Method of Solution

The multi-region heat transfer problem can be solved by the method used by Carslaw and Jaeger [24]. The temperature distributions in various regions are given by

$$T_1(\eta_1) = T_o + \frac{\alpha_1 k_2 (T_m - T_o)}{\alpha_2 k_1 [1 + \text{Erf}(\gamma)]} [1 + \text{Erf}(\eta_1)] \quad (7)$$

$$T_2(\eta_2) = T_o + \frac{\alpha_1 k_2 (T_m - T_o)}{\alpha_2 k_1 [1 + \text{Erf}(\gamma)]} [1 + \frac{\alpha_2 k_1}{\alpha_1 k_2} \text{Erf}(\eta_2)] \quad (8)$$

$$T_3(\eta_3) = T_f + \frac{T_m - T_f}{\text{Erfc}(\gamma)} \text{Erfc}(\eta_3) \quad (9)$$

where

$$\eta_i = x/2\sqrt{\alpha_i t}, \quad i = 1, 2, 3$$

and the location and the speed of the freezing front are given by

$$S(t) = 2\gamma (\alpha_3 t)^{1/2} \quad (10)$$

$$\dot{S}(t) = \gamma \sqrt{\alpha_3} / \sqrt{t} \quad (11)$$

Here  $k_2$  and  $\alpha_2$  are taken to be equal to  $k_3$  and  $\alpha_3$  respectively and  $\gamma$  is obtained from the following transcendental equation:

$$\frac{T_m - T_o}{1 + \text{Erf}(\gamma)} + \frac{T_m - T_f}{1 - \text{Erf}(\gamma)} = \sqrt{\pi} \rho \frac{\alpha_3}{k_3} L \gamma e^{\gamma^2} \quad (12)$$



After knowing the rate of formation of the solid phase the distribution of solute in the liquid phase can be obtained by solving the mass diffusion problem described by Eq. (5) and the associated conditions (6a-c). An exact solution for the above problem can be obtained by using similarity variables which are determined using Lie group theory. Details of this theory and its application for the solution of differential equations can be found [29,30]. Using this group theoretic approach the similarity variables can be found to be (See Refs. [26,27,28]).

$$y = \frac{x}{\sqrt{t}} \text{ and } \psi_n = \frac{C(\sqrt{t})^n}{A_n}, \quad n = 0, 1, 2, \dots, \infty \quad (13)$$

where  $A_n$ 's are constants to be determined later. To satisfy the boundary condition (6c) using these new variables the principle of superposition will be used by defining the concentration  $C$  as

$$C = \sum_{n=0}^{\infty} A_n \psi_n \frac{1}{(\sqrt{t})^n} \quad (14)$$

Using (13) and (14) the Eq. (5) and the auxiliary conditions (6a-c) can be written as

$$2D \frac{d^2 \psi_n}{dy^2} + (y + 2\gamma\sqrt{\alpha_3}) \frac{d \psi_n}{dy} + n \psi_n = 0 \quad (15)$$

$$\psi_n (y \rightarrow \infty) = C_0 \delta_{no} \quad (16a)$$

$$\frac{d\psi_n}{dy} - \frac{\gamma\sqrt{\alpha_3} (k_e - 1)}{D} \psi_n = (1 - \delta_{no}) \frac{\gamma\sqrt{\alpha_3} (k_e - 1)}{D} \sum_{j=0}^{n-1} (-1)^{n-j} \psi_j \quad (16b)$$

where  $\delta_{no}$  is the Kronecker delta and  $A_n$ 's of expression (14) are given by

$$A_n = (8r/\alpha_3)^n, n = 0, 1, 2, \dots, \infty$$

For this problem four terms of the series (14) were computed by determining  $\psi_0$ ,  $\psi_1$ ,  $\psi_2$  and  $\psi_3$  from Eq. (15). These solutions are (see Ref. [26,27,28]).

$$\psi_0(r) = C_0 \left[ 1 - \frac{G \operatorname{Erfc}(\sqrt{2} r)}{(\sqrt{8/\pi}) \operatorname{Exp}(-4\gamma^2 \alpha_3/D) + G \operatorname{Erfc}(2\gamma\sqrt{\alpha_3/D})} \right]$$

$$\psi_1(r) = - \frac{G \psi_0(r_0)}{r_0 + G} e^{-(r^2 - r_0^2)/2}$$

$$\psi_2(r) = - \frac{G[\psi_0(r_0) - \psi_1(r_0)]}{r_0 G + (r_0^2 - 1)} \cdot r e^{-(r^2 - r_0^2)/2}$$

$$\psi_3(r) = - \frac{G[\psi_0(r_0) - \psi_1(r_0) + \psi_2(r_0)]}{(r_0^2 - 1)G + r_0(3 - r_0^2)} (r^2 - 1) e^{-(r^2 - r_0^2)/2}$$

where

$$G = \gamma\sqrt{\alpha_3} (k_e - 1) \sqrt{2/D}, r = (y + 2\gamma\sqrt{\alpha_3})/\sqrt{2D} \text{ and } r_0 = \gamma\sqrt{2\alpha_3/D}$$

Using these expressions for  $\psi_0$ ,  $\psi_1$ ,  $\psi_2$  and  $\psi_3$  the concentration of solute in the liquid phase was computed using the Eq. (14) and then the corresponding

concentration in the solid phase ( $C_s$ ) was obtained using the following expression derived by Aziz [25] for nonequilibrium partition coefficient.

$$\frac{C_s}{C} = \frac{\dot{S}(t)\beta + k_e}{\dot{S}(t)\beta + 1} \quad (17)$$

In the present model the inter-diffusivity  $D^*$  is taken to be equal to the mass diffusivity and the interatomic spacing  $\lambda$  is taken to be  $4\text{\AA}$  which is the average diameter of an atom. Other physical properties for the alloy were computed at its nominal composition using the following relationships:

$$\rho = 1 / \sum_{j=1}^n W_j / \rho_j$$

where  $n$  = total number of elements present in the liquid pool of cladding

$$L = \sum_{j=1}^n W_j L_j$$

$$\bar{k}_i(T) = \rho \sum_{j=1}^n \frac{W_j}{\rho_j} \bar{k}_{ij}(T)$$

$$k_i = \int_{T_0}^{T_f} \bar{k}_i(T) dT / (T_f - T_0)$$

$$\bar{C}_p(T) = \sum_{j=1}^n W_j \bar{C}_{pj}(T)$$

$$C_p = \int_{T_0}^{T_m} \bar{C}_p(T) dT / (T_m - T_0)$$

$$\bar{\alpha}_i(T) = \rho \sum_{j=1}^n \frac{W_j}{\rho_j} \bar{\alpha}_{ij}(T)$$

$$\alpha_i = \int_{T_0}^{T_f} \bar{\alpha}_i(T) dT / (T_f - T_0)$$

and the diffusion coefficient for the  $j$ -th solute in the liquid phase is

$$D_j = \int_{T_0}^{T_f} D_{0j} e^{-\frac{\bar{Q}}{RT}} dT / (T_f - T_0)$$

where  $D_{0j}$  is the self-diffusion coefficient of the  $j$ -th element and  $\bar{Q}$  is the activation energy for the mixture given by

$$\bar{Q} = \sum_{j=1}^n w_j Q_j$$

In all these expressions for thermophysical properties of the cladding powder mixture, the index  $i = 1, 2, 3$  refers to the solid substrate, solidified cladding and the liquid cladding region, respectively, and  $j = 1, 2, 3, \dots$ , refers to the  $j$ -th element of the cladding powder mixture. Here,  $W_j$  and  $w_j$  are the weight fraction and the mole fraction of the  $j$ -th element, respectively.  $\bar{k}_{ij}$  and  $\bar{\alpha}_{ij}$  denote respectively the thermal conductivity and the thermal diffusivity of the  $j$ -th element in the  $i$ -th region.  $C_{pj}$  is the specific heat of the  $j$ -th element. The thickness of the cladding can be determined by taking an over-all energy balance which yields the following expression for the radius ( $r_c$ ) of the semi-cylindrical strip of cladding:

$$r_c = \left[ \frac{2fP}{\{(T_f - T_0) C_p + L\} \pi v \rho} \right]^{\frac{1}{2}} \quad (18)$$

where  $f$  is the fraction of laser energy absorbed by the cladding material,  $P$  is the power of the laser beam incident on the material, and  $v$  is the speed of the workpiece which can be related to the volumetric rate ( $q$ ) of powder delivery by

$$q = \frac{1}{2} \pi r_c^2 v \quad (19)$$

assuming that all of the delivered powder form cladding on the substrate.

#### D. Results and Discussion

The results of the above model was compared with experimental data. Laser cladding was performed on nickel substrate with two different cladding materials of nominal composition 74% Ni and 26% Hf in one case and 74% Ni and 26% Al in the other case. The solid substrate was clad with these cladding materials which take the shape of an approximately semi-cylindrical strip of metal on the substrate (see Fig. 1(b)). Electron Probe Micro Analysis of these samples shows the concentration of Hf and Al in the matrix of Ni in excess of what is predicted by the equilibrium phase diagram. The present model predicts the composition of the extended solid solution quite well. These results have been presented in the Table I for  $T_f = 2035^\circ\text{K}$  for the Ni-Hf alloy and  $T_f = 1907^\circ\text{K}$  for Ni-Al alloy.

Table I Comparison of Theoretical Results with Experimental Results of Extended Solid Solution

Laser Power (Kw)	Laser Beam Diameter (mm)	Speed of the Work-piece (Inch/min)	Nominal Composition of the cladding material (wt. %)	Composition in the solid solution (wt. %)	
				Theoretical Results	Experimental Results
5	3	50	74 Ni, 26 Hf	3.05 Hf	3.58-6.50 Hf
5	3	50	74 Ni, 26 Al	27.3 Al	22 Al

Note that there is large fluctuation in Hf data based on two analytical techniques used; Electron probe microanalysis and x-ray dispersive analysis. Fine distribution of Hf particles and beam diameter of two instruments are

probably the source of fluctuation. The prediction of composition of the extended solid solution based on the present model is within 30% of the experimental results. This discrepancy may be due to some of the assumptions of this model. For example, solidification has been assumed to take place at a constant temperature which has been taken to be the freezing point of the cladding material at its nominal composition. But it is well known that the change in composition in the liquid phase will alter its freezing point. Also the present model utilizes an expression (17) for nonequilibrium partition coefficient which is applicable to dilute solution. Apart from these the presence of a two-phase zone between the solidus and the liquidus lines and the surface tension driven flow causing convection in the liquid pool will affect the mixing of solute in the liquid phase and thus alter its composition in the solid phase. Paucity of high temperature liquid metal data also contributes to the numerical error. However, the objective of this study is to determine the trend and thus understand the underlying process physics.

The above model was used to study the effect of various important process parameters such as the cooling rate, cladding powder delivery rate on the composition of hafnium in nickel and aluminum matrices. Details of these studies can be found in [26,27,28]. Ref. [26] is enclosed on APPENDIX III.

#### IV. CONCLUSIONS

##### A. Current Works

By laser cladding process uniform and fine distribution of undissolved Hf, Hf rich precipitates and matrix with extended solid solution of Hf in the laser clad region could be achieved. These are supposed to contribute towards an increase in the oxidation resistance properties of Ni base alloys at elevated temperatures due to various mechanisms as discussed earlier. The volume fraction and size of  $\gamma'$  precipitates depend upon the laser processing conditions. Because of inherent rapid cooling during laser cladding process, many meta-stable Hf rich phases are formed. The formation of many meta-stable Hf rich phases would also contribute toward an increase in the oxidation resistance properties. The overall oxidation resistance properties of the laser clad alloy produced by under-focused laser beam was found to be better than the alloy produced by over-focused laser beam as well as Inconel 718 substrate. The present results suggest that the reactive elements would change the mechanism of the scale formation as a competitive reaction is taking place for the oxidation. These reactive oxidized particles will act as sinks for excess vacancies thus inhibiting their condensation at the scale/matrix interface and possibly enhancing scale adhesion.

The mathematical model of this study examines the extension of solid solubility based on the transport of energy and mass. Solute transport has been considered to take place only in the liquid phase while the energy transport has been considered in both solid and liquid phases. Effect of nonequilibrium cooling rate on solute segregation at the freezing front has been taken into account by considering a nonequilibrium partition coefficient. Using this the mass transfer problem has been solved analytically in a frame of reference moving with the freezing front with a

velocity determined from the heat transfer problem. These mathematical solutions have been utilized to study the effect of various process parameters on the concentration of solute in an alloy. The cooling rate is found to drop sharply within one second after the solidification starts and it is also higher for lower initial pool mean temperature. The hafnium concentration in the nickel-hafnium alloy is found to be higher for higher cooling rate. Also, it was found that more laser energy is required to obtain an alloy of a given composition at a higher powder delivery rate than that for a lower rate of powder delivery.

#### B. Plans for Future Works

A parallel laser cladding has been done on GTD 111 substrate and microstructural evolution of the laser clad samples are under progress. Under a laser processing conditions, microstructural changes in the laser clad alloys made on three different substrates would be compared and will provide an additional information about the effect of alloying elements on the microstructure. Similarly, the oxidation properties and thermal stability of the alloys would be compared and optimum condition would be set up for the best oxidation resistance properties.

We will also carry out the following tasks to develop mathematical models which will allow us to predict the composition of the alloy formed due to nonequilibrium cooling in laser cladding:

- (1) To develop an expression for nonequilibrium partitioning for real solution.
- (2) Develop a one-dimensional model for nonequilibrium phase diagram by using temperature-dependent equilibrium partition coefficient in the expression of nonequilibrium partition coefficient.



- (3) We will extend the above models to two- and three-dimensional cases of heat and mass transport and to multi-component alloy systems.

## REFERENCES

1. Allam, I. M., D. P. Whittle, and J. Stringer, "Corrosion and Erosion of Metals," K. Nateson (ed.), pp. 103-117, published by TMS-AIME, 1980.
2. Smeggil, J. G., and A. W. Funkenbusch, "A Study of Adherent Oxide Scale," United Technologies Research Center Report #R85-916564-1, May 1985.
3. Whittle, D. P., and J. Stringer, Philos. Trans. R. Soc. Lond, Ser. Vol. A295, p. 309, 1980.
4. Tien, J. K., and F. S. Pettit, Metal. Trans., Vol. 3, pp. 1587-1599, 1972.
5. Golightly, F. A., F. H. Stott, and G. C. Wood, Oxide. Met., Vol. 10, pp. 163-187, 1976.
6. Antill, J. E., and K. A. Peakall, J. Iron Steel Inst., Vol. 205, pp. 1136-1142, 1967.
7. Pfeiffer, H., Werkst. Korros., Vol. 8, p. 574, 1957.
8. Giamci, A. F., and D. L. Anton, Metallurgical Trans. A, Vol. 16A, pp. 1997-2005, Nov. 1985.
9. Nash, P., and R.F. West, Metal Science, Vol.
10. Singh, J., and J. Mazumder, "Microstructural Evolution in Laser Clad Fe-Cr-Mn-C Alloy," Material Sciences and Technology, Vol. 2, p. 709, 1986.
11. Singh, J., and J. Mazumder, "Laser Clad Fe-Cr-Mn-C Alloy for Improved Wear Properties," Met. Trans. A, to appear in Feb. 1987.
12. Chande, T., and J. Mazumder, Applied Physics Letter, Vol. 41, p. 42, 1982.
13. Chande, T., and J. Mazumder, J. Appl. Physics, p. 2226, Vol. 57, March 1985.
14. Li, L. J., and J. Mazumder Laser Processing of Materials, K. Mukherji and J. Mazumder (eds.), pp. 35-50, published by TMS-AIME, 1985.
15. J. Mazumder, and W. M. Steen, J. Appl. Phys., 51, 941 (1980).
16. Chan, C., J. Mazumder, and M. M. Chen, Met. Trans., Vol. 15A, 1984, p. 2175.
17. J. C. Baker, and J. W. Cahn, in Solidification, papers presented at a seminar of the American Society for Metals, Seminar Coordinated by T. J. Hughel, and G. F. Bolling (American Society for Metals, Metals Park, OH, 1971) pp. 23-58.
18. W. J. Boettinger, and J. H. Perepezko, in Proceedings of Rapidly Solidified Crystalline Alloys, edited by S. K. Das, B. H. Kear, and C. M. Adam (Metallurgical Society of American Institute of Metallurgical Engineers, Warrendale, PA, 1986), pp. 21-58.

19. W. J. Boettinger, S. R. Coriell, and R. F. Sekerka, R. F., Mat. Sci. Eng., **65**, 27 (1984).
20. W. J. Boettinger, in Proceedings of Rapidly Solidified Amorphous and Crystalline Alloys, edited by B. H. Kear, B. C. Giessen, and M. Cohen (North-Holland, New York, 1982), Vol. 8, pp. 15-31.
21. Chan, C., J. Mazumder, and M. M. Chen, J. of Mat. Sci. and Tech., to appear in 1987.
22. J. Singh, and J. Mazumder, "Effect of Extended Solid Solution of Hf on the Microstructure of the Laser Clad Ni-Fe-Cr-Al-Hf Alloys," Acta Met. accepted for publication.
23. W. W. Mullins, and R. F. Sekerka, J. Appl. Phys., **35**, 444 (1964).
24. H. S. Carslaw, and J. C. Jaeger, Conduction of Heat in Solids, 2nd. Ed., (Clarendon Press, London, 1959), pp. 282-296.
25. M. J. Aziz, J. Appl. Phys., **53**, 1158 (1982).
26. A. Kar, and J. Mazumder, J. Applied Phys., April (1987) to appear.
27. J. Mazumder, and A. Kar, J. Metals, Feb. (1987) to appear.
28. A. Kar, and J. Mazumder, ASME/JSME Conf., Hawaii, March 22-27 (1987).
29. G. W. Bluman, and G. D. Cole, Similarity Methods for Differential Equations, (Springer-Verlag, New York, 1974).
30. L. V. Ovsiannikov, Group Analysis of Differential Equations, (Translation edited by W. F. Ames), 1st ed. (Academic Press, New York, 1982).
31. J. Singh, K. Nagarathnam, and J. Mazumder, High Temperature Coating, M. Khobaib and R. C. Kruntenant (Eds.), published by TMS-AIME (1987).

## APPENDIX I

Effect of Extended Solid Solution of Hf on the  
Microstructure of the Laser Clad Ni-Fe-Cr-Al-Hf Alloys

Jogender Singh and J. Mazumder  
Laser Aided Materials Processing Laboratory  
Department of Mechanical Engineering  
1206 West Green Street  
University of Illinois  
Urbana, IL 61801

### ABSTRACT

Alloys and coatings for alloys for improved high temperature service life under aggressive atmosphere are of great contemporary interest. There is a general consensus that addition of reactive elements such as Hf will provide many beneficial effects for such alloys. The laser cladding technique was used to produce Ni-Fe-Cr-Al-Hf alloys with extended solid solution of Hf. A 10 kW CO<sub>2</sub> laser with mixed powder feed was used for laser cladding. Optical, scanning electron (SEM) and scanning transmission electron (STEM) microscopy were employed for microstructural evolution of alloys produced during laser cladding processes. The electron probe microanalysis and the auger electron spectroscopy were also used for micro-chemical analysis of different phases. Microstructural studies revealed a high degree of grain refinement, considerable increase in solubility of Hf in matrix and Hf rich precipitates and new metastable phases. This paper will report the microstructural development in this laser clad Ni-Fe-Cr-Al-Hf alloy.

### INTRODUCTION

Structural alloys requiring exposure to an aggressive atmosphere at elevated temperature often need protective coatings for oxidation resistance to achieve enhanced service lifetime. MCrAl.R.E. (M = Ni, Fe, Co) systems are widely used for such coatings. These coatings tend to form Al<sub>2</sub>O<sub>3</sub> rich scales. The Al<sub>2</sub>O<sub>3</sub> is the protective coating of choice (1,2) since: 1) diffusion through the oxide scale is very slow, 2) volatility is limited, 3) growth kinetics is slow, and 4) it is relatively inert in a high temperature oxidation environment.

However, the adhesion of Al<sub>2</sub>O<sub>3</sub> to the substrate is poor. Attempts to improve the adhesion have largely centered on the reactive element (RE)

effect. Y or Hf are mainly used to improve the adherence of  $\text{Al}_2\text{O}_3$  scale on the M Cr Al Y or MCrAlHf alloys and coatings. There are various mechanisms proposed by various authors regarding the beneficial effect of R.E. addition to MCrAl alloys. Some of these are listed below.

1. The formation of mechanical "pegs" which anchor the scale to the substrate metal alloy [1,3],
2. The rare earth dispersoids provide alternative vacancy coalescence sites and thus prevent the vacancy coalescence at the scale-metal interface [4],
3. Increased bonding forces are formed between the scale and substrate through preferential segregation of the reactive elements at the interface [3],
4. The interaction with trace elements such as sulfur forming refractory phases and thus limiting the sulfur segregation at the scale-substrate interface [2],
5. The reduction of scale growth processes [5],
6. The enhancement of scale plasticity by structure modification [6],
7. The reduction of thermomechanical differences between the scale and the substrate by the formation of graded oxide layers [7], and,
8. Refractory metal (e.g. Re) addition to nickel superalloys inhibits the  $\gamma'$  coarsening process and thus results in higher temperature capabilities [8].

Although there are controversies regarding which particular mechanism or groups of mechanisms are responsible for improved high temperature properties, there is a general consensus that the addition of reactive metals improves the high temperature service life and that they perform best when they are in a finely dispersed form.

Using conventional techniques, it is very difficult to incorporate RE elements in finely dispersed form above 1 wt. percent, which is the solid solubility limit [9]. The inherent rapid heating and cooling rate in laser processing can be effectively used to produce an alloy with extended solid solution and uniform distribution of phases [10-13]. The laser cladding technique was used to produce Ni-Fe-Cr-Al-Hf alloy with high Hf contents compared with alloys produced by conventional techniques such as plasma spraying of prealloyed powders. This is a technique where a mechanical mixture of powders of choice is delivered into a laser melted pool and solidified rapidly [10,11,14]. The increase in solid solubilities of the alloying elements with RE depends upon the processing conditions for laser cladding. The main variables during laser processing are laser power, size and shape of laser beams, scan velocity and the chemistry and metallurgy of the substrate. The overall composition and microstructure of the laser clad materials was also determined by the degree of mixing and cooling rate. For the optimum laser processing condition and possible application, a scheme is needed to select the best combination for a given workpiece. The main objective is to develop Ni-based superalloys of Ni-Cr-Al-Hf with a maximum solid solubility of Hf in it by laser cladding technique in order to generate stable and protective films which should provide improved oxidation resistance. It is also expected that these alloys with extended solid solution of Hf will increase the high temperature stability by retarding the  $\gamma'$  coarsening kinetics and provide fine precipitates and thus improve the intermediate and high temperature strength.

In order to understand the high temperature service behavior of these alloys, it is necessary to know about the crystal structure, stability and chemical composition of the different phases developed during the laser cladding process and correlate this structure with the laser processing

conditions. Moreover, to the best of the knowledge of the authors nobody has reported the microstructure evolution of the rapidly solidified Ni-Fe-Cr-Al-Hf alloy with extended solid solution of Hf.

#### EXPERIMENTAL PROCEDURE

AISI 1016 steel was used as the substrate material. Ni, Cr, Al, and Hf powders in the ratio of 10:5:1:1 were used as mixed powder feed for cladding. Size of Ni, Cr, Al powders used were about 5  $\mu\text{m}$  in diameter whereas Hf powder was of 44  $\mu\text{m}$  in maximum diameter. The average chemical analysis of the laser clad region was found by electron probe micro analysis to be 70% Ni, 10% Cr, 10% Fe, 5% Al, and 5% Hf (all in weight percents). The cladding treatments were carried out using an AVCO HPL 10 kW CW  $\text{CO}_2$  laser with F7 cassegrain optics (as shown in Fig. 1). The laser was operated in the  $\text{TEM}^*_{01}$  mode\*. The beam focused by cassegrain optics was reflected downward toward the substrate by a flat mirror. The laser was operated typically at approximately 5, 6 and 7 kW. Specimens (approximately 6.4 mm thick) were traversed relative to the laser beam at a speed of approximately 6.35 and 14.8 mm per second. The powder was delivered to the area of interaction by a pneumatic powder delivery system with a feed screw. The powder flow was regulated by varying the speed and changing the size of the feed screw. The flow rate for the present study was approximately 0.2 gm/second. Argon gas with a flow rate of 7.7 gm/sec was used to maintain a steady powder flow through the copper tubing leading to the substrate. Powder was placed on the substrate just prior to its contact with the laser.

---

\*Donut-shaped laser beam with a Gaussian power distribution in the outer ring and none at the hole of the donut.



A shielding of argon gas with a shielding box was used to minimize surface contamination during laser processing. The argon gas which directed the powder flow into the molten pool of substrate was also used in plasma suppression at the laser-substrate interaction point. The function of the shielding box was to provide the inert environment near the laser-substrate interaction point which also reduced clad porosity [10].

Microstructural observation of clad specimens was carried out by Auger electron spectroscopy, optical, and scanning electron microscopy. After mechanical and chemical polishing to a thickness of 0.3 mm, 3 mm discs were punched from the clad material. Specimens for the TEM observations were prepared by the jet polishing technique with an electrolyte of 200 c.c. 2-Butoxy-ethanol, 400 c.c. methanol, 50 c.c. perchloric acid at 35 volts with the electrolyte at a temperature of  $-15^{\circ}\text{C}$ . Samples were observed using a Phillips EM 430 microscope (equipped with an EDAX) operated at 300 kV.

### RESULTS AND DISCUSSION

Optical microstructure of the laser clad Ni-Cr-Al-Hf alloy is presented in Fig. 2. It shows uniform distribution and formation of second phase in the laser clad matrix as well as at the grain boundaries. At low magnification it is difficult to resolve the undissolved Hf particles. The second phase appeared to be spherical in nature. The concentration of each of the elements (Ni, Cr, Al, Hf, Fe) in the laser clad region was found by the electron probe microanalysis. Figure 3 represents the concentration profile of each alloying elements across the laser clad/substrate region. The distribution of each alloying elements in the laser clad region was found to be uniform.

In order to see the presence and distribution of undissolved Hf in the laser clad region, Scanning Electron Microscopy (SEM) was carried out. The

SEM micrograph shows undissolved Hf particles dispersed throughout the matrix and also few at grain boundaries as indicated by arrows in Fig. 4. The undissolved Hf particles were confirmed by the SEM x-ray microanalysis and this is discussed in the next section.

To see the detailed internal structure of the laser clad region, STEM investigation was carried out. The general survey of the thin foils show the fine and uniform distribution of undissolved Hf particles with 1 to 9  $\mu\text{m}$  size, and Hf rich precipitates in the nickel rich matrix containing high density of dislocations and  $\gamma'$  precipitates (Fig. 5). STEM microanalysis from the undissolved Hf revealed only Hf peaks, Fig. 6. The detailed microstructural analysis would be discussed below. Figures 7(a) and 7(b) represent bright field (bf) and dark field (df) electron micrographs of the laser clad matrix region. The dark field micrograph from one of the (001) reflections show the presence of ordered precipitates in the f.c.c. matrix. The precipitate has been identified as  $\gamma'$  type precipitate which is an ordered f.c.c. phase. The corresponding diffraction pattern from the matrix is presented in Fig. 7(c). Figure 7(c) shows the superlattice reflections from the precipitates in addition to the major reflections from the gamma matrix. The local zone axis of both gamma ( $\gamma$ ) and gamma prime ( $\gamma'$ ) grains was [100]. This suggests that the growth of the  $\gamma'$  precipitate was along the cube direction of the matrix, i.e.  $[100]_{\gamma} // [100]_{\gamma'}$ . From the dark field image, it is difficult to deduce conclusively the shapes as the precipitates are very small. However, it is believed that they are  $\gamma'$  precipitates with rectangular shape. The size and volume of the  $\gamma'$  precipitates depends upon the laser processing conditions i.e. cooling rates, which will be discussed later. The composition of the matrix was determined by EDX and is displayed in Fig. 8. The matrix is mainly Ni with small amounts of Cr, Fe, Al, and Hf in it. From

the microchemical analysis it is possible to comment on the substitution of Ni and Al by Cr, Fe, and Hf, respectively. The Ni-Al-Hf phase diagram is the most significant as it supplies the only information available on the substitution behavior of Hf. In this diagram, the  $\gamma'$  phase field is extended towards  $\text{Ni}_3\text{Hf}$ , indicating that Hf substitutes for Al. Rawlings and Bevan [15] reported that Si, V, Mn, Nb, Hf, and Ta alloying additions substitute for the aluminum; Co and Cu substitute for nickel and Cr, Fe, W, and Mo substitute for both species of the gamma prime ( $\text{Ni}_3\text{Al}$ ) phase. The Mossbauer investigation by Nicholls [16] also reported an interesting result. The proportion of Fe atoms on aluminum and nickel sites was found to be a function of Fe concentration. At low concentrations (2.5 at %) approximately three-quarters of the Fe atoms were on aluminum sites, whereas at high concentrations (10 at %Fe), there were approximately equal numbers of Fe atoms on aluminum and nickel sites. The substitution behavior is determined by electronic rather than size factor considerations [15]. The addition of these alloying element has also an influence on the mechanical properties of  $\gamma'$  precipitate. Considerable strengthening is obtained in the  $\gamma'$  precipitate when the alloying addition substitute for aluminum and has a large misfit parameter [17]. Thus the addition of Hf and Fe to the nickel-base alloys, i.e., Ni-Cr-Al, would modify both mechanical properties as well as oxidation resistance properties.

In order to determine the size and volume fraction of the  $\gamma'$  precipitates present in the matrix, series of dark field TEM micrographs were taken under strong two-beam condition (operating one of the  $\langle 100 \rangle$  reflections) at high magnifications. In order to minimize the error, TEM of all laser processed samples were carried out at the same high magnifications (130,000X and 160,000X). The volume fraction  $V_v$  of the precipitates have been determined by quantitative transmission electron microscopy utilizing approximate corrections for overlap as follows [18,19]:

$$V_v = V'_v / 1 + \frac{3}{2} \cdot \frac{t}{D}$$

where the foil thickness  $t$  of each samples were estimated and the apparent volume fraction  $V'_v$  and the average precipitate size  $D$  were measured in each case.

The size and volume of the  $\gamma'$  precipitate in  $\gamma$  matrix depends upon the laser processing conditions. Figure 9 shows that there is linear increase in the size of  $\gamma'$  precipitates with increasing laser beam power for a constant traverse speed. The size of the  $\gamma'$  precipitate is comparatively larger at low traverse speed (6.35 mm per sec) as compared with the high traverse speed (14.8 mm per sec). Similarly, the volume fraction of the  $\gamma'$  precipitate also increases with the function of laser beam power (Fig. 10). The volume fraction of  $\gamma'$  precipitate is higher at low traverse speed as compared with high traverse speed for a given set of laser beam power. This could be explained on the basis of laser beam interaction time with the alloy, i.e. rate of cooling during rapid solidification. At a given laser beam power (e.g. 6 kW), there would be less interaction time for an alloy made at a traverse speed of 14.8 mm/s as compared with an alloy made at a traverse speed of 6.25 mm/s. Therefore, the rate of cooling would be faster in the former case (e.g. 6 kW, 14.8 mm/s) as compared with the later case (e.g. 6 kW, 6.35 mm/s).

At this stage it is difficult to comment about the solid solubility of Fe in the matrix and of Hf in the  $\gamma'$  phase as the precipitates were very small. But, it has been found that by increasing the cooling rates (particularly in laser processing technique), there was an increase in solid solubility of the alloying additions in the matrix as well as in the precipitates. The cooling rates attainable by this process are known to enhance

elemental homogeneity and to extend, in some cases, elemental concentrations beyond normal saturation limits. Furthermore, under the normal rapid quenching of Ni-based superalloys (e.g., Ni-Cr-Al), the  $\gamma'$  precipitation could only be seen after suitable long aging heat treatments. In spite of such a high cooling rate ( $\sim 10^5$ °C/s) occurred during laser melting and solidification process,  $\gamma'$  precipitates have been observed in the laser clad Ni-Cr-Al-Hf alloys. It clearly indicates that the addition of Hf to the Ni-Cr-Al alloy enhances the activation energy or driving force for the precipitation of  $\gamma'$  precipitates. The volume fraction of  $\gamma'$  precipitation depends upon the solid solubility of Hf in the matrix. Thus, the initial size and volume fraction of  $\gamma'$  precipitate and increase in solid solubility of Fe and Hf has an influence on the oxidation resistance properties. On the basis of STEM microanalysis of the matrix, the possible composition of  $\gamma'$  precipitate would be  $(\text{Ni, Cr, Fe})_3(\text{Al, Hf})$ .

The general survey of the thin foil from the laser clad samples (under different laser processing conditions) shows the formation of many unknown meta-stable phases with different microchemistry. Since the equilibrium phase diagram for this quaternary Ni-Cr-Al-Hf is not available, and the volume fraction of each phase developed was very small, there is difficulty in identifying each of the phases.

Figure 11 displays an electron micrograph of the laser clad region showing the blocky type of precipitate in matrix. Figure 12(b) is the dark field electron micrograph taken from one of the precipitate reflections. The corresponding selected area diffraction pattern and indexing (considering pseudo cubic crystal structure) is presented in Figs. 12(c) and 12(d), respectively. Because of inherent rapid solidification during laser process, meta-stable phases contained distortions and strains, therefore, identification of

phase is complex. In addition, the phase diagram of this complex alloy system is not available and volume fraction of each phase is very small.

The corresponding x-ray micro analysis from the precipitate is presented in Fig. 12. It revealed that the precipitate is rich in Hf with relatively small amounts of Ni, Cr and Fe in it. As the precipitate contains mainly Hf and Ni with very small amount of Cr, Fe and Al, thus pseudo binary Ni-Hf diagram can be considered. Based on the diffraction analysis and micro-chemistry of the precipitate, it appeared that the precipitate is having tetragonal crystal structure. Detailed convergent-beam microdiffraction diffraction analysis of this precipitate will be reported in the future.

The size of the undissolved Hf particles varied from 0.5  $\mu\text{m}$  to 10  $\mu\text{m}$  in diameter depending on the traverse speed and laser power as shown in Fig. 13. Figure 13 shows that undissolved Hf particle size increases with traverse speed and laser power. It is expected that the undissolved Hf particle size will be higher for higher speed since increased speed leads to decreased interaction time. Interaction time is critical for dissolution of high melting point (2423°K) material such as Hf. The increase of undissolved Hf particle diameter with the increase of power is not obvious. However, this can be explained on the basis of specific energy input for laser cladding [14]. For constant traverse speed and powder feedrate, increased power leads to slower cooling rate which results in reduced surface tension driven convection [20]. Mass transport in laser surface modification with mixed powder feed depends primarily on convection [13]. Therefore reduced convection will cause reduced dissolution leading to higher undissolved Hf particle size. Scatter in particle size distribution data is also higher for higher laser power. This is because of the fact that higher power increases the width of the molten pool [20,21] resulting in a wide range of cooling

rates depending on the position in the pool. This variation of cooling rate also leads to variation of undissolved Hf particle size due to variation of convection.

It would be appropriate to comment here that by increasing the RE addition to the Ni based supper alloys it is expected that it would contribute to the improvement of the oxidation resistance properties following many of the mechanisms as described earlier.

SUMMARY

By laser cladding process uniform and fine distribution of undissolved Hf, Hf rich precipitates and matrix with extended solid solution of Hf in the laser clad region could be achieved. These are supposed to contribute towards an increase in the oxidation resistance properties of Ni base alloys at elevated temperatures due to various mechanisms as discussed earlier. The volume fraction and size of  $\gamma'$  precipitates depend upon the laser processing conditions. Because of inherent rapid cooling during laser cladding process, many meta-stable Hf rich phases are formed. The formation of many meta-stable Hf rich phases would also contribute toward an increase in the oxidation resistance properties. Thus, overall oxidation resistance properties of the alloy developed by the laser cladding process would be expected to be better than Ni base alloy made by the conventional technique.



ACKNOWLEDGMENT

This work was made possible by a grant from the Air Force Office of Scientific Research (Grant No. AFOSR-85-0333). The authors wish to thank Dr. A. Rosenstein and Major Hagar of AFOSR for their continued encouragement. The studies involving electron microscopy were performed in the Center for Microanalysis of Materials in the MRL of University of Illinois at Urbana-Champaign.

## REFERENCES

1. Allam, I. M., D. P. Whittle, and J. Stringer, "Corrosion and Erosion of Metals," K. Nateson (ed.), pp. 103-117, published by TMS-AIME, 1980.
2. Smeggil, J. G., and A. W. Funkenbusch, "A Study of Adherent Oxide Scale," United Technologies Research Center Report #R85-916564-1, May 1985.
3. Whittle, D. P., and J. Stringer, Philos. Trans. R. Soc. Lond, Ser. Vol. A295, p. 309, 1980.
4. Tien, J. K., and F. S. Pettit, Metal. Trans., Vol. 3, pp. 1587-1599, 1972.
5. Golightly, F. A., F. H. Stott, and G. C. Wood, Oxide. Met., Vol. 10, pp. 163-187, 1976.
6. Antill, J. E., and K. A. Peakall, J. Iron Steel Inst., Vol. 205, pp. 1136-1142, 1967.
7. Pfeiffer, H., Werkst. Korros., Vol. 8, p. 574, 1957.
8. Giamci, A. F., and D. L. Anton, Metallurgical Trans. A, Vol. 16A, pp. 1997-2005, Nov. 1985.
9. Nash, P., and R.F. West, Metal Science, Vol. 1.
10. Singh, J., and J. Mazumder, "Microstructural Evolution in Laser Clad Fe-Cr-Mn-C Alloy," Material Sciences and Technology (in press), Vol. 2, p. 709, 1986.
11. Singh, J., and J. Mazumder, "Laser Clad Fe-Cr-Mn-C Alloy for Improved Wear Properties," Met. Trans. A, accepted for publication in Feb. 1987.
12. Chande, T., and J. Mazumder, Applied Physics Letter, Vol. 41, p. 42, 1982.
13. Chande, T., and J. Mazumder, J. Appl. Physics, p. 2226, Vol. 57, March 1985.
14. Li, L. J., and J. Mazumder Laser Processing of Materials, K. Mukherji and J. Mazumder (eds.), pp. 35-50, published by TMS-AIME, 1985.
15. Rawlings, R. D., and A. S. Bevan, "The Alloying Behavior and Mechanical Properties of Polycrystalline  $\text{Ni}_3\text{Al}$  ( $\gamma'$  Phase) with Ternary Additions," J. of Material Science, Vol. 10, pp. 505-514, 1975.
16. Nicholls, J. R., Ph.D. Thesis, London University, 1974.
17. Ahmet Baldan, "Some Effects of Ta and Hf Additions on the Room Temperature Mechanical Properties of Ni-Base Ni-Al-Ta and Ni-Al-Hf Super Alloys," Z. Metallike, p. 24, 1985.
18. Underwood, E. E., "Quantitative Stereology," Addison-Wesley, Reading, MA, 1970.

19. Kelly, P. M., Metals Forum, Vol. 5, No. 1, 1982, p. 13.
20. Chan, C., J. Mazumder, and M. M. Chen, Met. Trans., Vol. 15A, 1984, p. 2175.
21. Chan, C., J. Mazumder, and M. M. Chen, J. of Mat. Sci. and Tech., to appear in 1987.

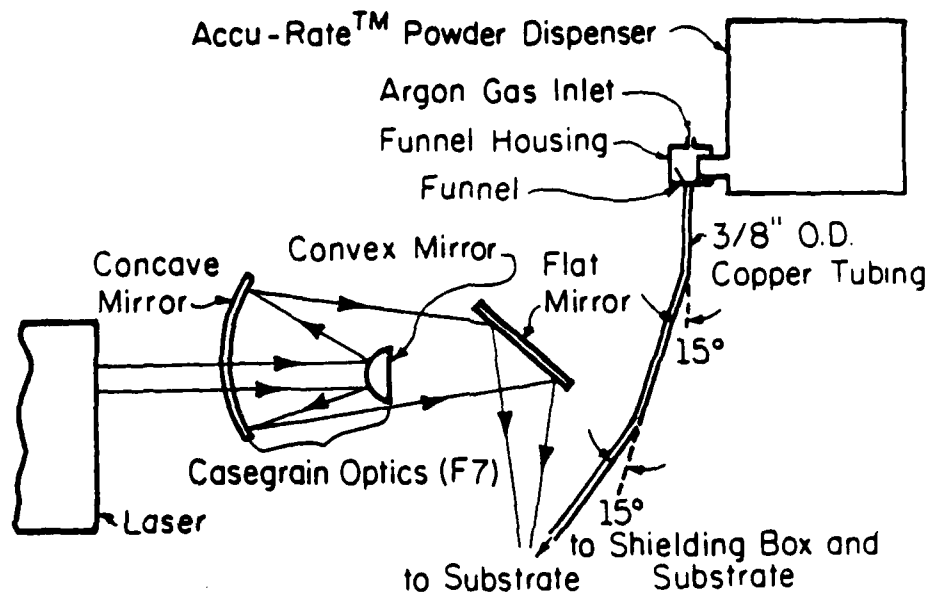
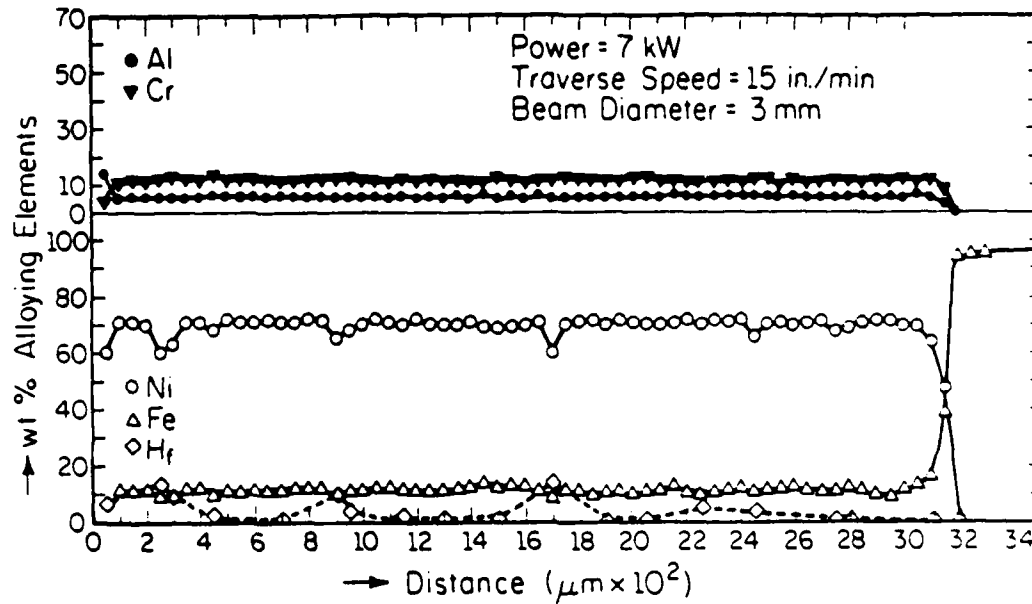


Fig. 1 Optics used for laser cladding.



**Fig. 2** Optical micrograph of laser clad Ni-Cr-Fe-Al-Hf alloy (7 KW, 14.8 mm/sec) shows the uniform distribution and formation of second phase in the nickel matrix.



Fig. 3 Electron micro probe analysis of laser clad region and substrate showing the uniform distribution of alloying elements.

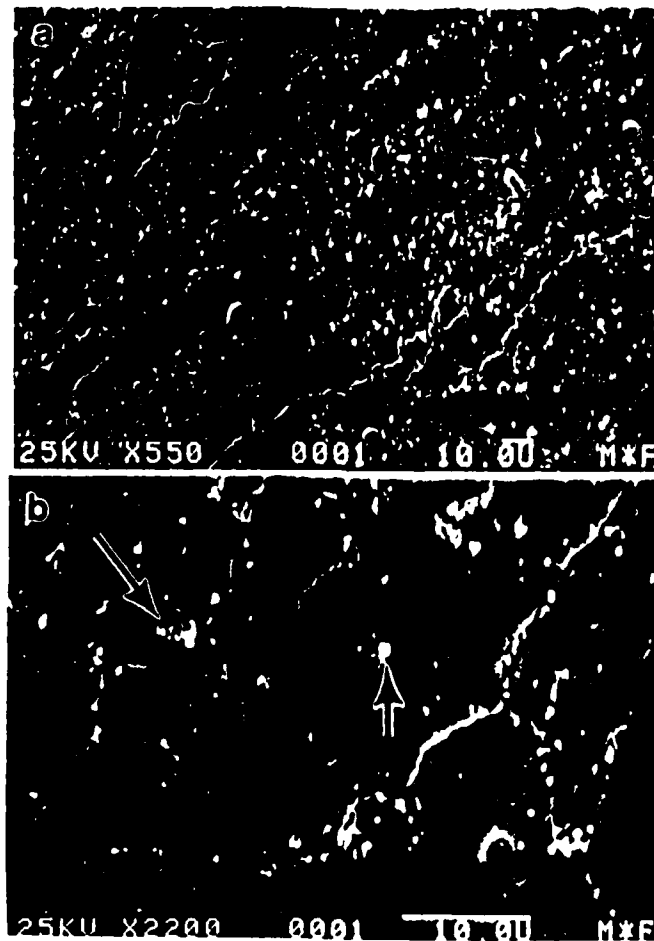


**Fig. 4** Scanning electron micrograph (a) and (b) showing the uniform distribution of undissolved Hf in the laser clad region

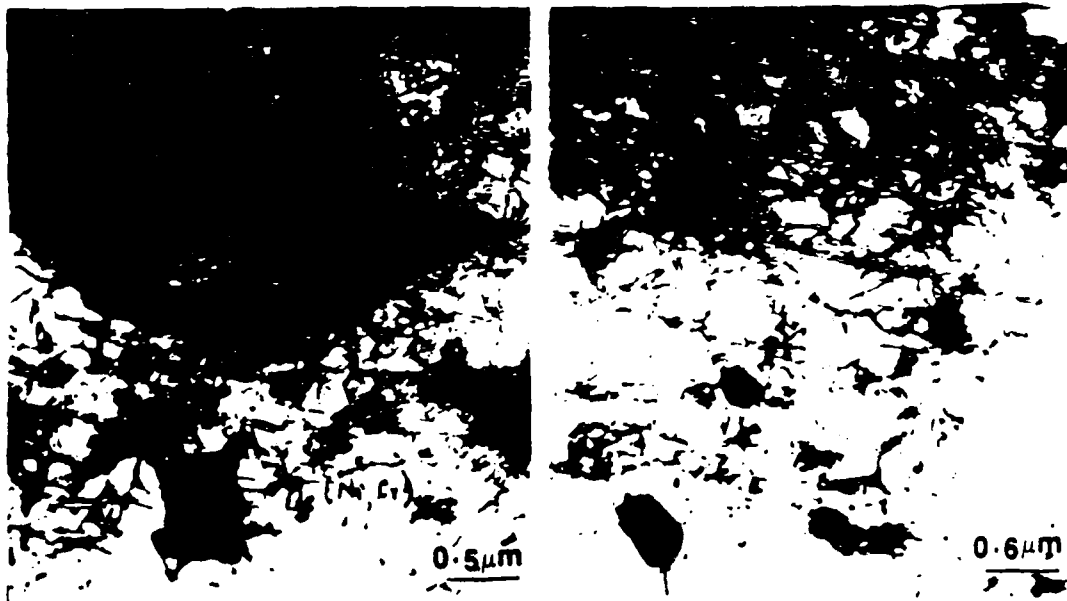


Fig. 5 General survey of TEM sample showing the undissolved Hf particles, Hf rich precipitates and high density of dislocations in the matrix of laser clad alloy.



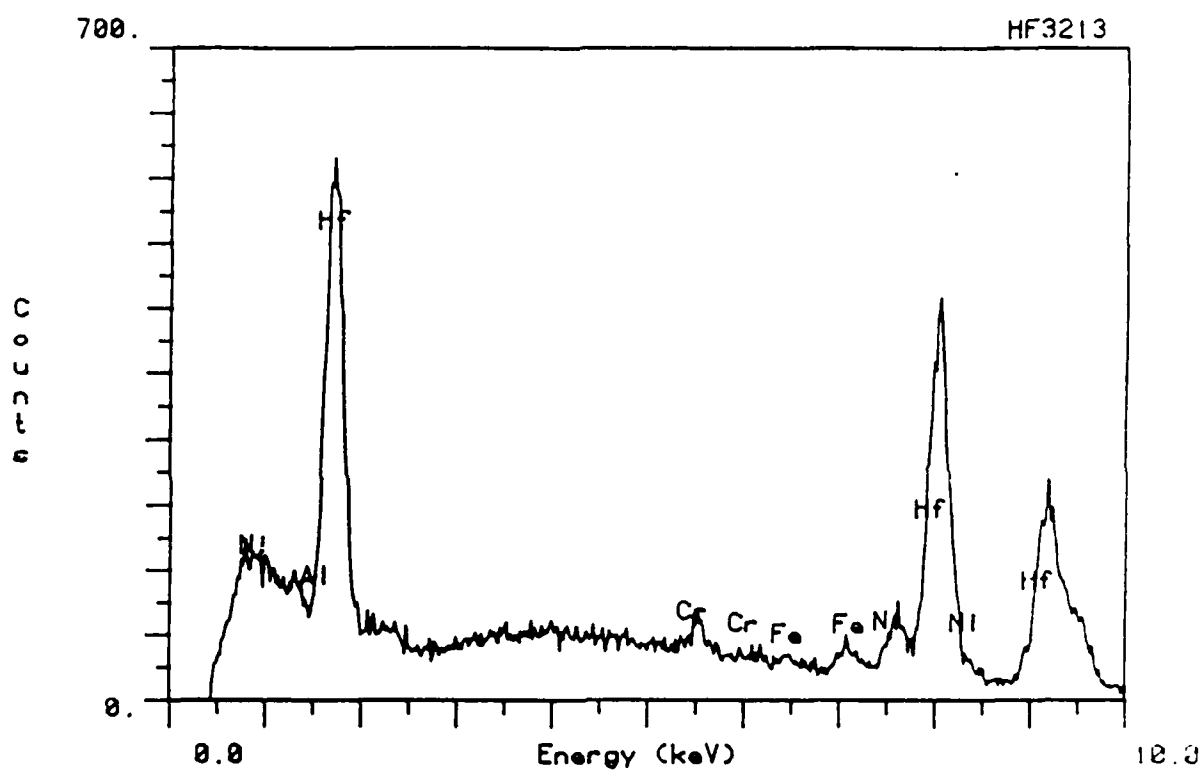
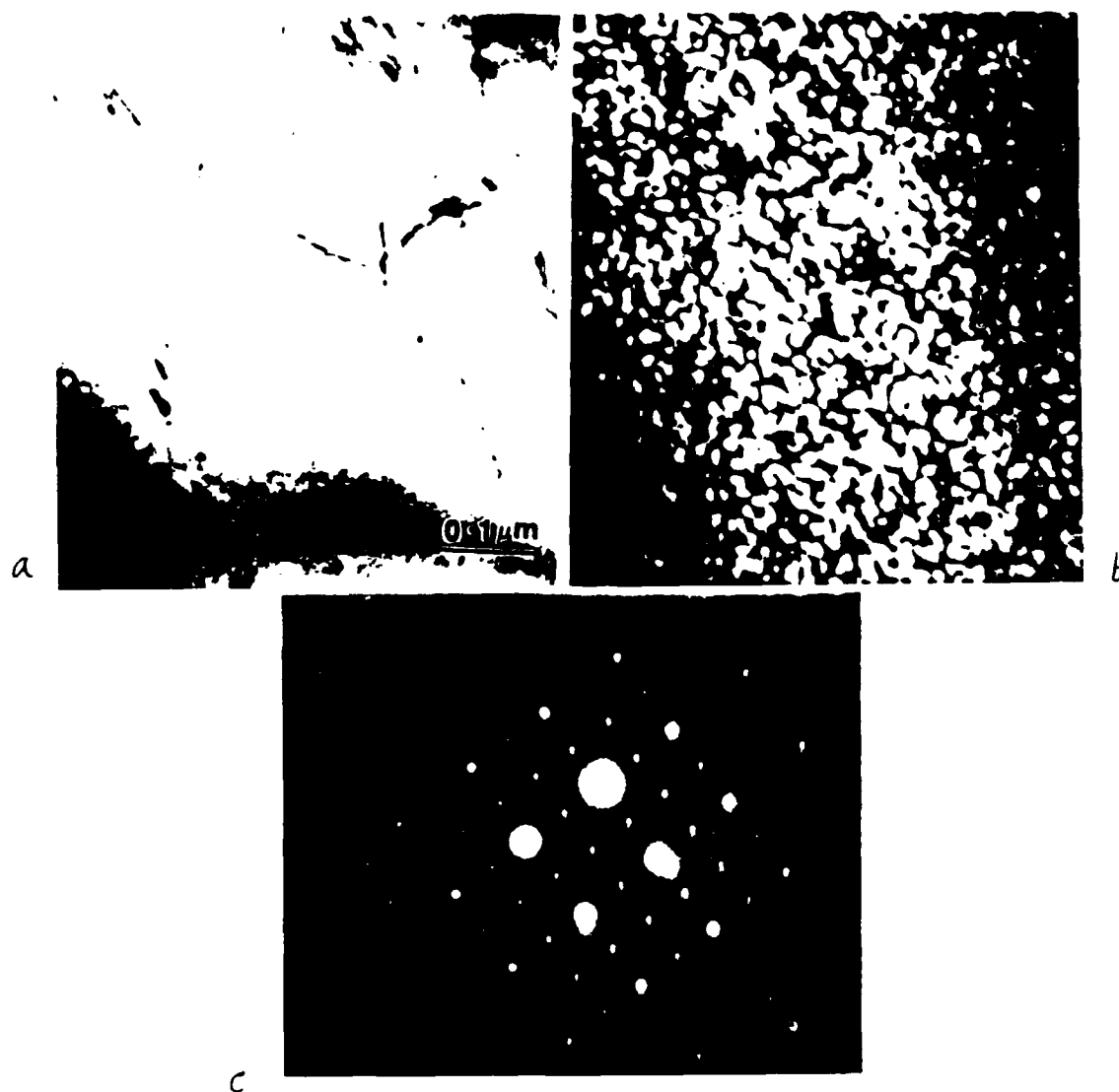
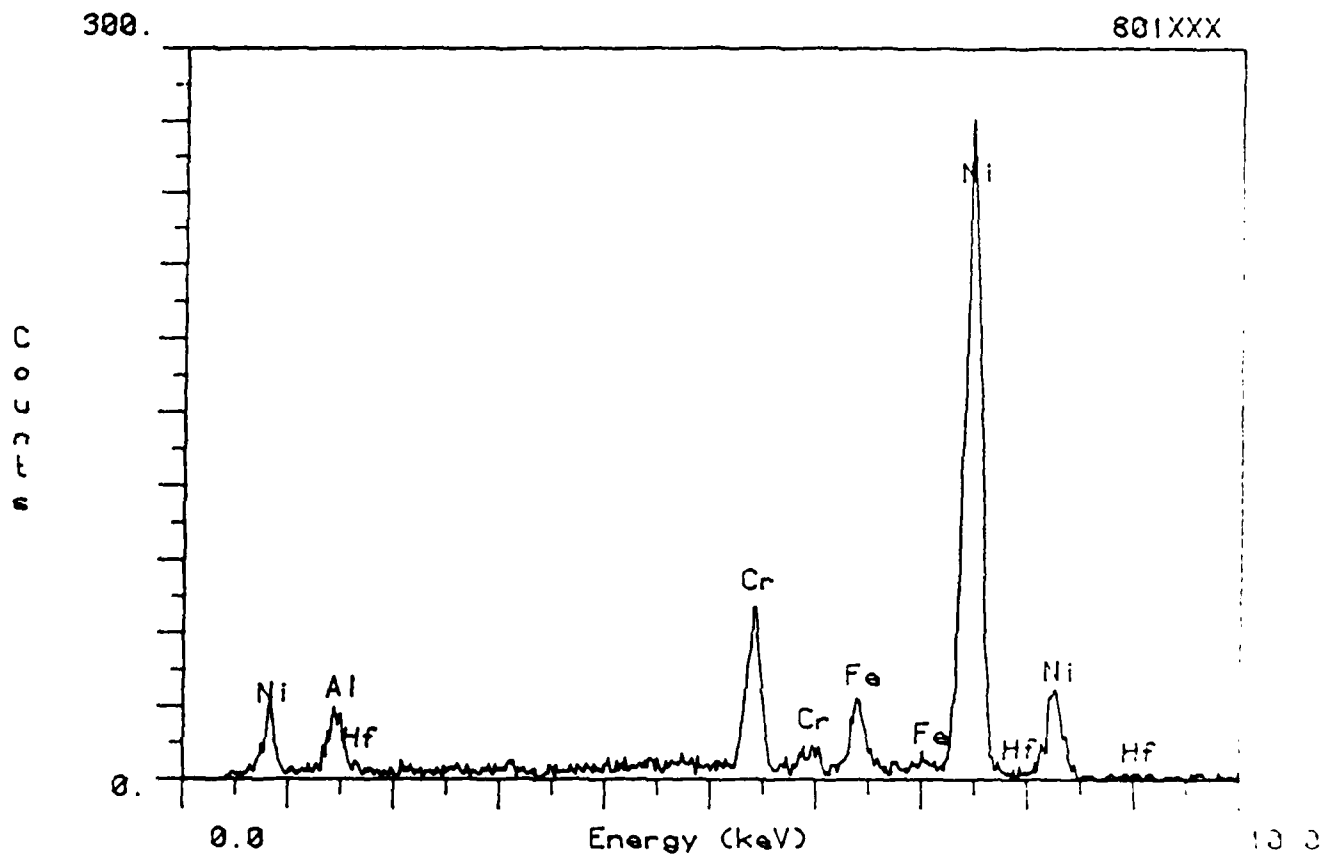


Fig. 6 STEM X-ray microanalysis from undissolved Hf particles showing mainly Hf peaks.



**Fig. 7** Electron micrographs from laser clad region showing that matrix is having  $\gamma'$  ( $\text{Ni}_3\text{Al}$ ) type precipitate. (a) bright field, (b) dark field, and (c) is corresponding diffraction pattern.



**Fig. 8** STEM X-ray microanalysis from the matrix showing that matrix is rich in Ni with small amount of Cr, Fe, Al and Hf alloying elements in it.

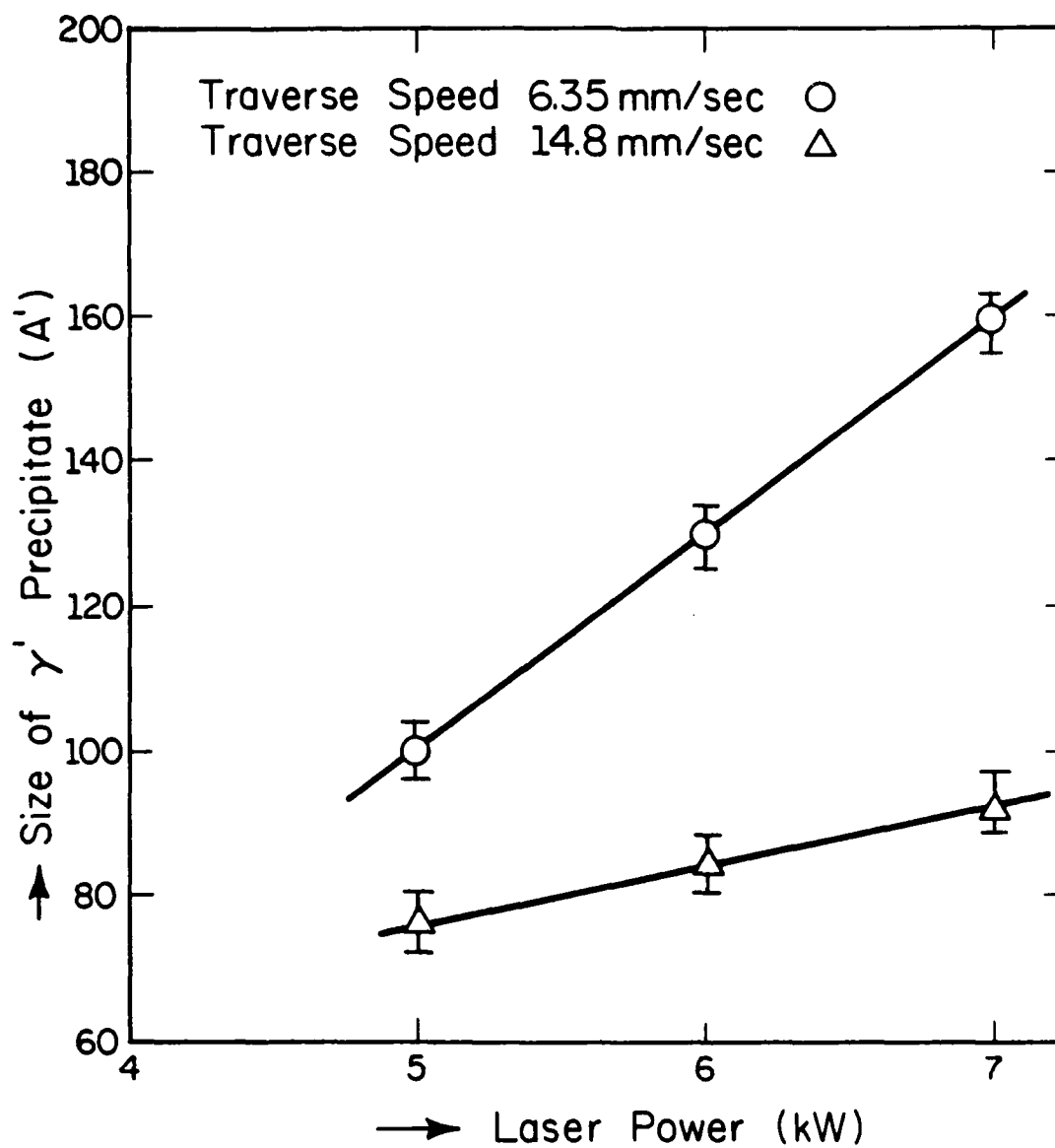


Fig. 9 A plot of size of  $\gamma'$  precipitate with the function of laser power and traverse speed.

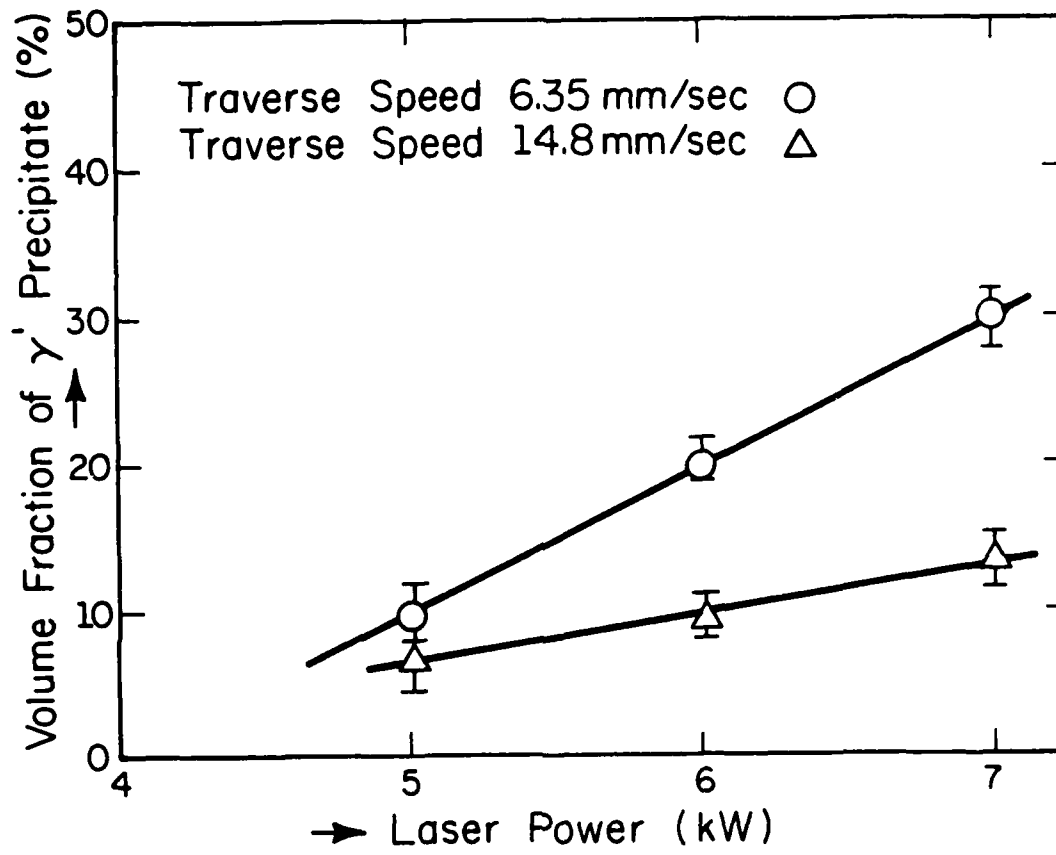
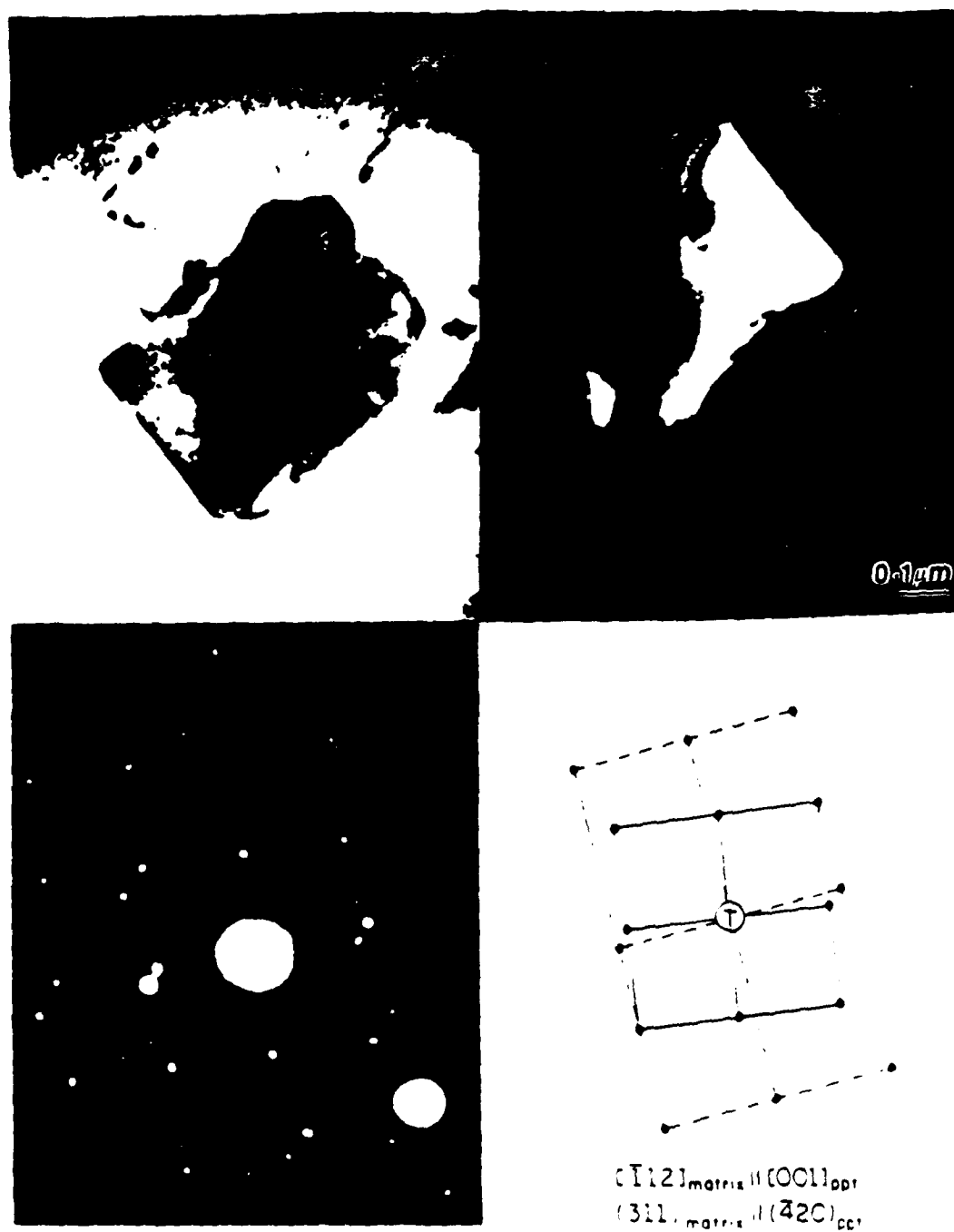


Fig. 10 A plot of volume fraction of  $\gamma'$  precipitate with the function of laser power and traverse speed.



**Fig. 11** Transmission electron micrograph of the laser clad sample showing the blocking type meta-stable phase. (a) bright field (b) dark field, (c) diffraction pattern, and (d) indexing.

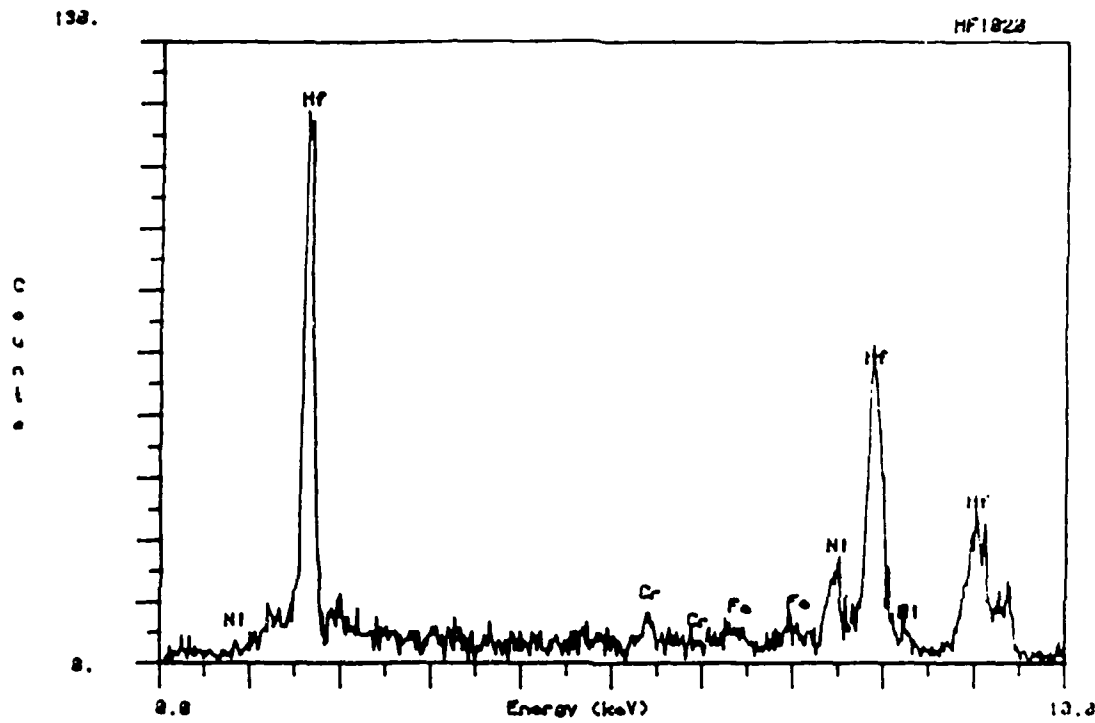


Fig. 12 STEM X-ray microanalysis of the precipitate indicating that the precipitate is Hf rich phase with small amount of Ni, Cr, and Fe in it.

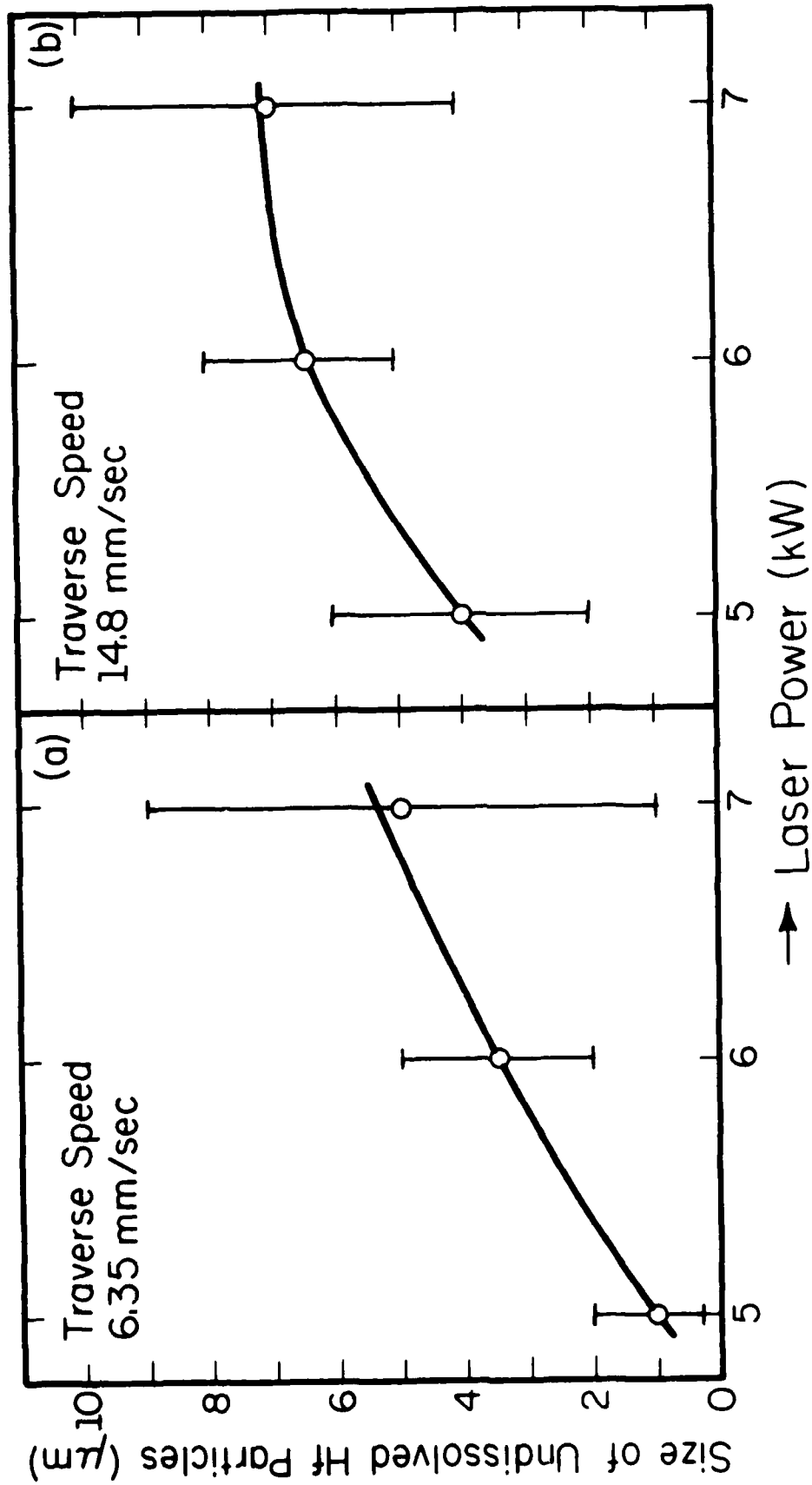


Fig. 13 A plot of size of undissolved Hf in the laser clad matrix with the function of laser power and traverse speed.



APPENDIX II

Laser Cladding of Ni-Cr-Al-Hf on Inconel 718  
for Improved High Temperature Oxidation Resistance

J. Singh, K. Nagarathnam, and J. Mazumder

Laser Aided Materials Processing Laboratory  
Department of Mechanical and Industrial Engineering  
University of Illinois at Urbana-Champaign  
1206 West Green Street  
Urbana, IL 61801

## Abstract

In situ Ni-Cr-Al-Hf alloy has been developed by laser surface cladding with mixed powder feed for improved high temperature oxidation resistance. The oxidation resistant materials for service at elevated temperatures must satisfy two requirements: diffusion through oxide scale must occur at the lowest possible rate and oxide scale must resist spallation. The formation of an  $\text{Al}_2\text{O}_3$  protective scale fulfills the former requirements but its adherence is poor. Reactive metal such as Hf is added to improve adhesion. A 10 kw  $\text{CO}_2$  laser was used for laser cladding. Optical, SEM and STEM microanalysis techniques were employed to characterize the different phases produced during laser cladding process. Microstructural studies showed a high degree of grain refinement, increased solid solubility of Hf in matrix and Hf rich precipitates. Thermo gravimetric analysis was carried out to determine the oxidation properties of these clad alloys with extended solid solution of Hf. Considerable improvement over the base metal was observed. This paper discusses the microstructural development in this laser clad alloy and its effect on oxidation.

Keywords: laser cladding, oxidation properties, high temperature coating.

### Introduction

Alloy selection for gas turbine materials application is to ensure superior mechanical properties and good corrosion and oxidation properties at elevated temperatures. In recent years, attention has been focused on developing suitable coatings to enhance service lives and are applied over less-oxidation resistant but mechanically stronger alloy substrates. MCrAl (M = Ni, Fe, Co) systems are widely used for such coatings. These coatings tend to form  $Al_2O_3$  rich scale which acts as a protective coating because:

- 1) diffusion of oxygen through the oxide scale is very slow,
- 2) volatility is limited,
- 3) growth kinetics is slow, and
- 4) it is relatively inert in a high temperature oxidation environment.

It has been well established that the addition of trace level of reactive elements such as yttrium, hafnium, etc. to coating alloy composition greatly enhances oxide scale adherence [1-3].

There are various mechanisms proposed by various authors regarding the beneficial effect of R.E. addition to MCrAl alloys. Some of these are listed below.

1. The formation of mechanical "pegs" which anchor the scale to the substrate metal alloy [1,3],

2. The rare earth dispersoids provide alternative vacancy coalescence sites and thus prevent the vacancy coalescence at the scale-metal interface [4],
3. Increased bonding forces are formed between the scale and substrate through preferential segregation of the reactive elements at the interface [3],
4. The interaction with trace elements such as sulfur forming refractory phases and thus limiting the sulfur segregation at the scale-substrate interface [5],
5. The reduction of scale growth processes [6],
6. The enhancement of scale plasticity by structure modification [7],
7. The reduction of thermomechanical differences between the scale and the substrate by the formation of graded oxide layers [8], and,
8. Refractory metal (e.g. Re) addition to nickel superalloys inhibits the  $\gamma'$  coarsening process and thus results in higher temperature capabilities [9].

Using conventional techniques, it is very difficult to incorporate rare earth (RE) elements in finely dispersed form above 1 wt%, which is the solid solubility limit [10]. The inherent rapid heating and cooling rates in laser processing can be effectively used to produce an alloy with extended solid solution and uniform distribution of phases [11-14]. The laser cladding technique was employed to produce Ni-Cr-Al-Hf alloy with high Hf contents compared with alloys produced by conventional techniques. The over all composition and microstructure of the laser clad materials was determined by the degree of mixing, cooling rate, and other laser processing variables [11].

The objective of this study was to develop an alloys of Ni-Cr-Al-Hf with increased Hf content which can provide better high temperature oxidation resistance properties. To the authors best knowledge, no one has reported the development of such coatings by laser cladding process.

### Experimental Procedure

The main objective of the laser cladding process is to clad a substrate with another material having a different chemistry by melting a thin interfacial layer to produce a metallurgical bond with minimum dilution of the clad layer by the substrate to provide improved surface properties. The clad material can be added either by predeposition techniques (e.g. preplacing a powder on the substrate, plasma spraycoat, electroplating) or co-deposition techniques (e.g. pneumatic delivery of powder into the laser melted pool, wire feed and ribbon feed). In this study a mixture of powders were pneumatically delivered into the laser melted pool. This technique is more energy efficient and provides higher cooling rate [15] which is needed to achieve extended solid solution.

Inconel 718 plate was used as a substrate material. Ni, Cr, Al, and Hf powders in the ratio of 10:5:1:1 were used as mixed powder feed for cladding. The cladding treatments were carried out using an AVCO HPL 10 kW CW CO<sub>2</sub> laser with F7 cassegrain optics (as shown in Fig. 1). The laser was operated in the TEM\*<sub>01</sub> mode\*. The beam focused by cassegrain optics was reflected downward toward the substrate by a flat mirror. The laser was operated typically at approximately 5, 6, and 7 kW. Specimens (approximately 6.0 mm thick) were traversed relative to the laser beam at a speed of approximately 6.35 and 10.6 mm per second. The powder was delivered to the area of interaction by a pneumatic powder delivery system with a feed screw. The powder flow was regulated by varying the speed and changing the size of the feed screw. The flow rate for the present study was approximately 0.2 gm/second.

---

\*Donut-shaped laser beam with a Gaussian power distribution in the outer ring and none at the hole of the donut.

Argon gas with a flow rate of 0.017 lb./s was used to maintain a steady powder flow through the copper tubing leading to the substrate. Powder was placed on the substrate just prior to its contact with the laser.

A shielding of argon gas with a shielding box was used to minimize surface contamination during laser processing. The argon gas which directed the powder flow into the molten pool of substrate was also used in plasma suppression at the laser-substrate interaction point. The function of the shielding box was to provide the inert environment near the laser-substrate interaction point which also reduced clad porosity.

Microstructural observation of clad specimens was carried out by optical and transmission electron microscopy. After mechanical and chemical polishing to a thickness of 0.3 mm, 3 mm discs were punched from the clad material. Specimens for the TEM observations were prepared by the jet polishing technique with an electrolyte of 200 c.c. 2-Butoxy-ethanol, 400 c.c. methanol, 50 c.c. perchloric acid at 35 volts with  $-15^{\circ}\text{C}$  temperature of electrolyte. Samples were observed using a Phillips 430 microscope (attached with an EDAX) operated at 300 kV.

Oxidation was performed on a Thermo Gravimetric Analyzer (TGA) of Dupont 1090 system. Test was carried out up to temperature  $1050^{\circ}\text{C}$  with air flow rate between 45-50 cc/min for a duration of 60 minutes.

### Results

Figure 2 represents a plot of weight gain with function of time for a period of 60 minutes at three temperatures ( $700^{\circ}\text{C}$ ,  $900^{\circ}\text{C}$ , and  $1050^{\circ}\text{C}$ ) of the laser clad samples (laser power 5 kW and traverse speed 6.35 mm/sec). It revealed that there is parabolic weight gain of the sample at oxidation temperature  $700^{\circ}\text{C}$ , and then it decreases at oxidation temperature  $900^{\circ}\text{C}$ . There was not

any significant change in the weight of sample observed at high oxidation temperature 1050°C. Figure 3 represents the oxidation data of the laser clad sample operated at different laser power and traverse speed. It shows that the maximum weight gain was observed in the laser clad sample with 5 kW laser power and 6.35 mm/sec traverse speed (with over focused laser beam) compared with the other samples of 5, 6, and 7 kW laser power, and traverse speed of 6.35 and 10.58 mm/sec (with under focused laser beam). Figure 3 also revealed that keeping the traverse speed constant (i.e., 6.35 mm/sec), with increasing laser power for under focused laser beam results decrease in weight gain. Table I gives the oxidation data for Inconel 718 at oxidation temperature 900°C for 1 hour. On comparing the oxidation data, the laser clad alloys show better oxidation resistance properties. In addition, the alloys prepared by under focused laser beam shows a dramatic increase in the oxidation resistance properties as compared with the substrate and alloys prepared by over focused laser beam. This will be discussed more in the next section.

The average composition of each elements was found to be uniform throughout the laser clad region except Hf. Hf distribution was found to be uniform through the laser clad matrix with compositional fluctuations. This depends upon the location of the microprobe analysis on either of Hf rich precipitates, Hf in the matrix or undissolved Hf particles in the matrix, thus the composition of the other alloying elements changes accordingly. This would be discussed in more detail in the next section.

On comparing the oxidation properties of the substrate with laser clad samples, it was found that all laser clad samples show better oxidation properties and especially under focused laser clad samples at oxidation temperature 1050°C. In order to understand the high temperature oxidation behavior of these alloys, microstructural investigation of the laser clad

samples were carried out. The optical micrographs of the laser clad sample are presented in Fig. 4. It shows uniform distribution and formation of second phase in the laser clad matrix. As there was not any sharp interface boundary between the laser clad region and substrate matrix, it suggests a good mixing and strong metallurgical bonding between the laser clad region and substrate. Figures 5a and b are the optical and SEM micrographs of the laser clad sample (at 5 kW, 6.35 mm/sec with over focused laser beam) reveals the uniform distribution of undissolved Hf and Hf rich precipitates throughout the matrix. The segregation of undissolved Hf particles were not observed at the grain boundaries. By changing the laser processing conditions (i.e. laser power 6 kW and traverse speed 6.5 mm/sec with under focused laser beam), the size and volume of second phase precipitate were also changed, Fig. 5c and d. Relatively large volume fraction with fine distribution of second-phase precipitate as well as undissolved Hf particles were observed. This is due to mainly laser optics interaction with the substrate during melting which would be discussed in the next section. To see the detailed internal structure of the laser clad region, STEM investigation was carried out. The general survey of the thin foils show fine and uniform distribution of undissolved Hf particle as marked by arrows, and also Hf rich precipitates in the nickel matrix (Fig. 6a and b). In addition, very fine gamma prime ( $\gamma'$ ) precipitates were also observed in the matrix (Fig. 6c). The average size of  $\gamma'$  precipitate is about  $\sim 70 \text{ \AA}$ . The  $\gamma'$  precipitates are coherent with the matrix and can only be seen in the dark field micrograph using one of the  $\gamma'$  precipitate super lattice reflections (Fig. 6c). The average composition of the matrix is displayed in Fig. 7. Figure 8 displays an electron micrograph of the laser clad region showing the precipitates containing high density of stacking faults, (Fig. 8a and b) and corresponding diffraction pattern from the precip-



itate is presented in Fig. 8c. The average composition of precipitate is presented in Fig. 9, which reveals that the precipitate is rich in Hf. As the equilibrium phase diagram of the Ni-Cr-Al-Hf quaternary system is not available and often metastable phases are formed during rapid solidification process [11], so it is difficult to comment about the exact crystal structure of this Hf rich phase. As the precipitates contains mainly Hf and Ni elements with very small amount of Cr and Al, thus pseudo binary Ni-Hf diagram can be considered. Based on the diffraction analysis (Fig. 8c) and microchemistry of the precipitate (Fig. 9), it appeared that the precipitate is having hexagonal crystal structure [11].

#### Discussion

It has been observed that inherent rapid melting and solidification during laser cladding process produces very fine grained microstructure with increased the solid solubility of Hf in matrix. The clad alloys were found to have better oxidation resistance properties as compared with the substrate and this is due to the combined effect of increased solid solubility of Hf, Hf rich precipitate and undissolved Hf in the Ni matrix (Fig. 3 and Table I). At this stage, it is difficult to comment about which particular mechanism or groups of mechanisms are responsible for improving high temperature oxidation resistance properties, as various mechanisms were proposed by various authors for the MCrAlRE alloys [3-8]. The most beneficial effect of laser cladding process was found to produce fine microstructure, uniform distribution of Hf rich precipitate and undissolved Hf particles. In addition, the undissolved Hf was in the form of hafnium and not the oxide of hafnium i.e., hafnia [11]. During oxidation, the undissolved Hf will form its oxide which will probably act as a pegs, which will increase the bonding between the oxide scale and

substrate [16]. Similarly, Hf rich intermetallic precipitates would decompose at high temperature and would form its oxide during oxidation process. Same behavior would be expected with Hf in the matrix. Therefore, there would be always a competitive reaction for the formation of oxide of hafnium among the hafnium present at different states. It is believed that these reactive-element oxide colonies provide excellent sinks for excess vacancies in the metal lattice that may have otherwise condensed at the scale/metal interface [17]. Condensation of vacancies at the scale/metal interface would promote spallation of the scale. Addition of Hf to the Ni based super alloys, not only improves the oxidation resistance properties, but it also improves the mechanical properties (especially creep properties) and controls the growth of gamma prime precipitates during high temperature cyclic treatments [18].

Theoretical calculations have shown that, in nickel based alloys containing aluminum with RE additions (Y or Hf), the RE atoms have a strong binding energy to the aluminum atoms [19], because of charge transfer from their high-lying valence orbitals to lower-lying Ni s-d bands. Thus, the outward diffusion of cations would apparently be suppressed because Cr atoms are tied up by RE (Hf) atoms. Therefore, the mechanism of scale growth may be controlled by the inward transport of oxygen. Further, as mentioned above, that the reactive elements provides an excellent sites to condense excess vacancies, it also acts as nucleation site for the continuous formation of  $\text{Cr}_2\text{O}_3$  layer thus prevent the depletion of Cr content in the alloy adjacent to the interface [19].

At this stage, it is difficult to comment about the extent of contribution of the size and volume fraction of  $\gamma'$  precipitate present in matrix towards the oxidation resistance properties. It has been observed that the volume fraction and size of  $\gamma'$  precipitate increases with increasing the laser

power or decreasing the traverse speed [20]. In the  $\gamma'$  ( $\text{Ni}_3\text{Al}$ ) precipitate, Al would be replaced by Hf where as Ni would be replaced by Cr, Co, Fe, etc. [11]. In order to have good binding energy between Hf with Al, Ni, Cr, it would be an ideal to have optimum size and volume fraction of  $\gamma'$  precipitate present in the matrix; which would probably suppress the outward diffusion of cations and increases the oxidation resistance properties.

The oxidation properties of under focused laser clad alloys were found to be better than over focused laser clad alloys. This is due to concentration difference of alloying elements present in a given volume of melt pool region which would be discussed in detail as follows. The laser beam diameter (3 mm) is the same as over focused and under focused position (Fig 10a), but their interaction with the substrate is different. Figure 10a represents a simple laser beam optics. When the substrate is positioned at over focused laser beam location with 3 mm beam diameter (Fig. 10b), the laser beam is in the converging mode. Once the laser beam is incident on the substrate, it would like to penetrate inside the substrate up to the focal point. The laser beam would melt the substrate up to focal point i.e. depth  $d_1$  of substrate and mix with melted powder to form a clad layer. If the substrate is located at the under focused laser beam with 3 mm diameter (Fig. 10c), the interaction of laser beam with substrate would be always with diverging beam with lower power density. The depth of penetration of laser beam inside the substrate would be low ( $d_2$ ) and would mix with same volume of melted powder to form a clad layer. Since the melt depth ( $d_1$ ) for over focused laser beam is more than  $d_2$  for under focused condition, melted volume for the over focused laser beam will be higher. This suggests that laser clad alloy produced by over focused laser beam would be more diluted with alloying elements such as Cr, Al and Hf. This will also directly control the total volume fraction of Hf rich

precipitates formed, solid solubility of Hf in the matrix and undissolved Hf particles present in the total volume of solidified melt pool region. Figure 5 supports the above statement that total volume fraction of Hf rich precipitates and undissolved Hf particles are more in case of under focused laser clad alloys as compared with over focused laser clad alloys because they were rich in alloying contents present in the less solidified melt pool region. Therefore, better oxidation properties are expected for laser clad alloys produced by under-focused laser beam.

#### Summary

By laser cladding process, fine microstructure with uniform distribution of undissolved hafnium, Hf rich intermetallic precipitates and matrix with extended solid solubility of Hf in the laser clad region was achieved. The overall oxidation resistance properties of the laser clad alloy produced by under-focused laser beam was found to be better than the alloy produced by over-focused laser beam as well as Inconel 718 substrate. The present results suggest that the reactive elements would change the mechanism of the scale formation as a competitive reaction is taking place for the oxidation. These reactive oxidized particles will act as sinks for excess vacancies thus inhibiting their condensation at the scale/matrix interface and possibly enhancing scale adhesion.

#### Acknowledgment

This work was made possible by a grant from the Air Force Office of Scientific Research (Grant No. AFOSR-85-0333). The authors wish to thank Dr. Rosentein and Major Hagar of AFOSR for their continued encouragement. The studies involving electron microscopy were performed in the Center for

Microanalysis of Materials in the MRL of University of Illinois at Urbana-Champaign.

### References

1. G. C. Wood and F. H. Stott, "High Temperature Corrosion," Rapp R. A. ed., Conference held at San Diego, California, March 1981, International Corrosion Conference Series, NACE-6, published by National Association of Corrosion Engineers, Houston, Texas (1983), 227.
2. D. P. Whittle, and D. H. Boone, "Surface and Interface in Ceramic and Ceramic-Metal Systems," Pask, J. and Evans, A. ed., Material Science Research, 14, Plenum press, New York, 487.
3. D. P. White and J. Stringer, Phil. Trans. Roy. Soc. London., A295 (1980) 309.
4. J. K. Tien and F. S. Pettit, Metal Trans., 3, (1972) 1587-1599.
5. J. G. Smeggil and A. W. Funkenbusch, "A Study of Adherent Oxide Scale," United Technologies Research Center Report #R85-916564-1, May 1985.
6. F. A. Golightly, F. H. Stott, and G. C. Wood, Oxide Met., 10, (1976) 163-187.
7. J. E. Antill and K. A. Peakall, J. Iron Steel Inst., 205, (1967) 1136-1142.
8. H. Pfeiffer, Werkst. Korros., 8, (1957) 574.
9. A. F. Giami and D. L. Anton, Met. Trans. A., Vol. 16A, Nov. 1985, pp. 1997-2005.
10. P. Nash and D. R. F. West, Metal Science, 15 (1981) 347.
11. J. Singh, and J. Mazumder, "Effect of Extended Solid Solution of Hf on the Microstructure of the Laser Clad Ni-Fe-Cr-Al-Hf Alloys," Acta Met., accepted for publication.
12. J. Singh and J. Mazumder, "Microstructural Evolution in Laser Clad Fe-Cr-Mn-C Alloys," Material Science and Technology, 2 (1986) 709.
13. T. Chande and J. Mazumder, J. App. Physics, 57 (1985) 2226.
14. I. M. Allam, D. P. Whittle, and J. Stringer, "Corrosion and Erosion of Metals," K. Nateson (ed.) 103-117, published by TMS-AIME, 1980.
15. L. J. Li, and J. Mazumder, Laser Processing of Materials, K. Mukherji and J. Mazumder (eds.), published by TMS-AIME, 1985, pp. 35-50.
16. W. E. King, N. L. Peterson, and J. F. Reddy, J. of Physics (1985) 423.
17. J. G. Smeggil, A. W. Funkenbusch, and N. S. Bornstein, High Temperature Science, 12 (1985) 163.
18. E. L. Hall and S. C., Huang, Met. Trans., 17 (1986) 407.

19. H. Yang, G. E. Welsch, and T. E. Mitchell, Mat. Sci. and Eng. 69, (1985) 351.
20. J. Singh and J. Mazumder, unpublished research work.

Table I Oxidation Data for Inconel 718  
(60 minutes at 900°C)

<u>No. of OBS</u>	<u>Initial Wt., grams</u>	<u>Final Wt., grams</u>	<u>Wt. Change, grams</u>
1	2.2856	2.2843	$-1.3 \times 10^{-3}$
2	0.6618	0.6594	$-2.4 \times 10^{-3}$



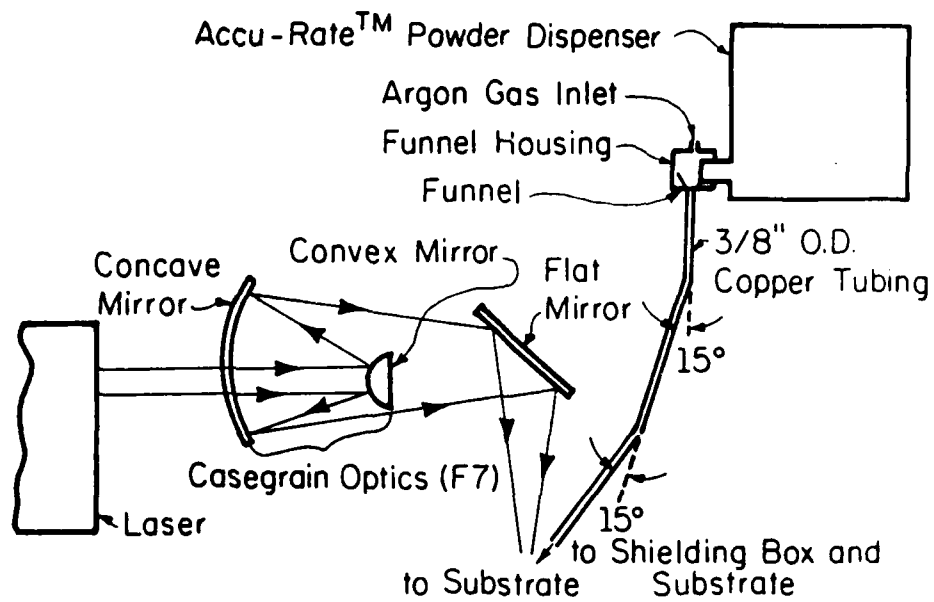


Figure 1 - Optics used for laser cladding.

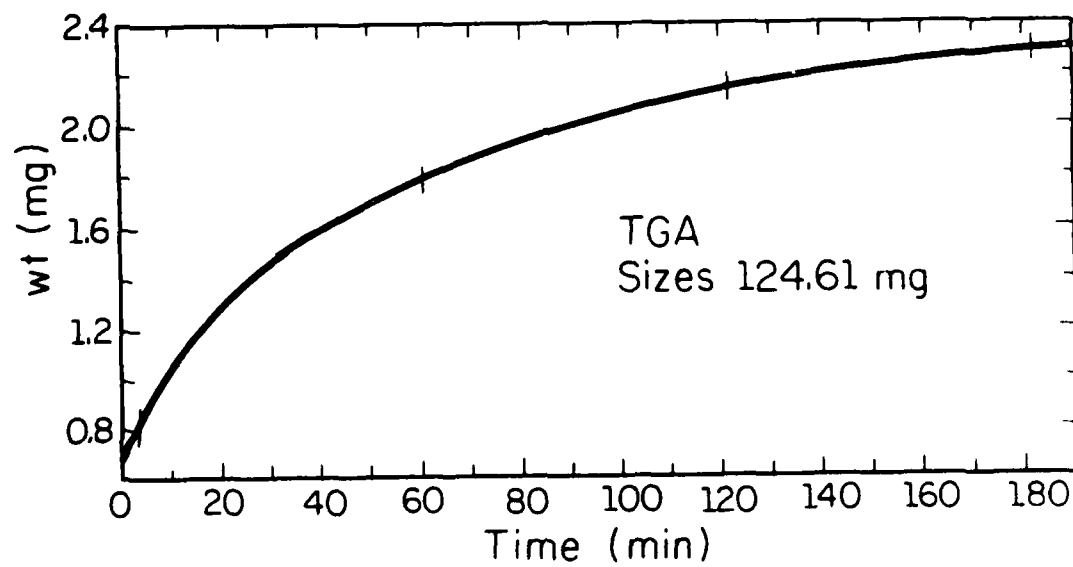


Figure 2 - TGA plot of laser clad sample at three temperatures 700°C, 900°C, and 1050°C with function of time.

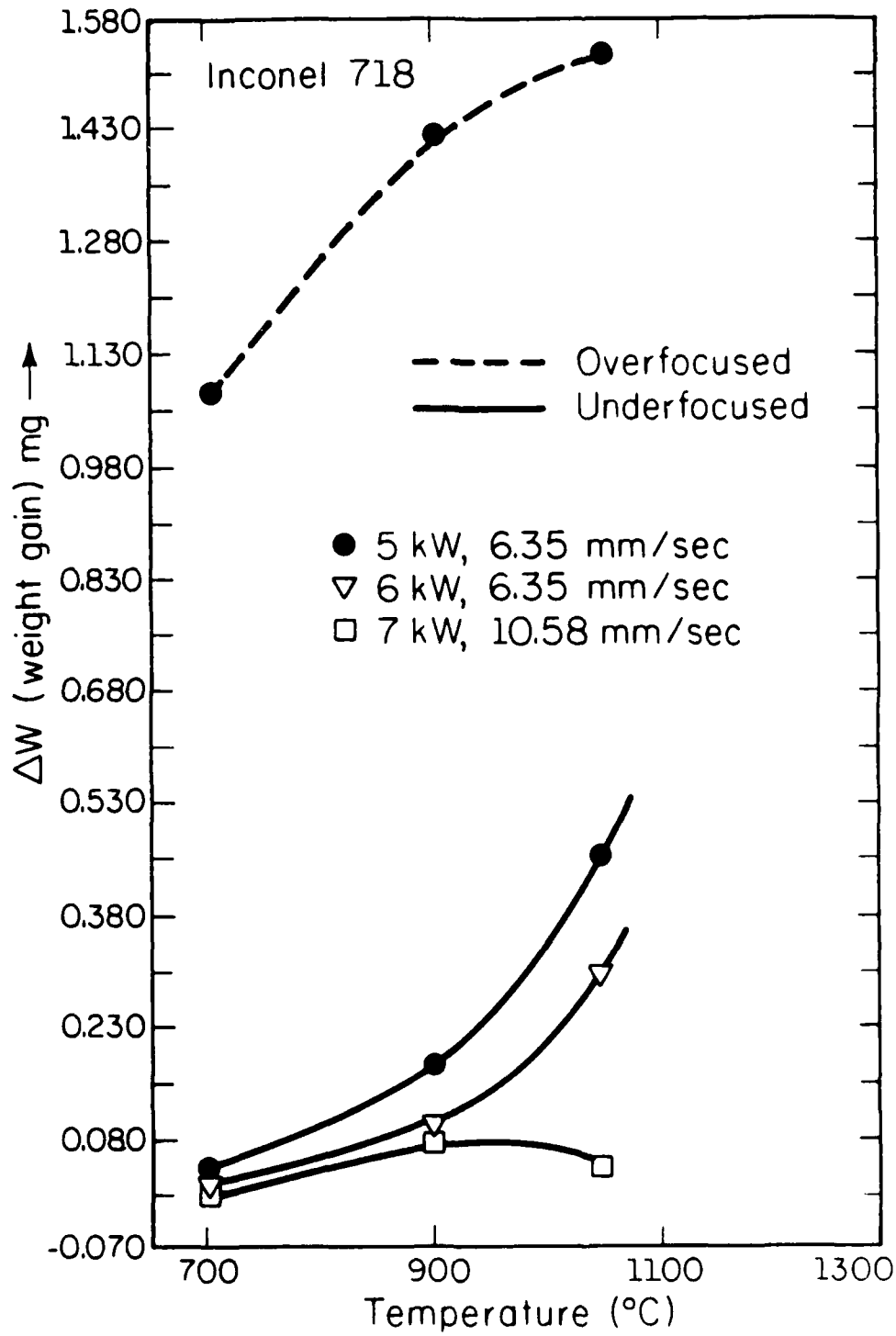


Figure 3 - A plot of weight gain versus temperature for different laser processing conditions.

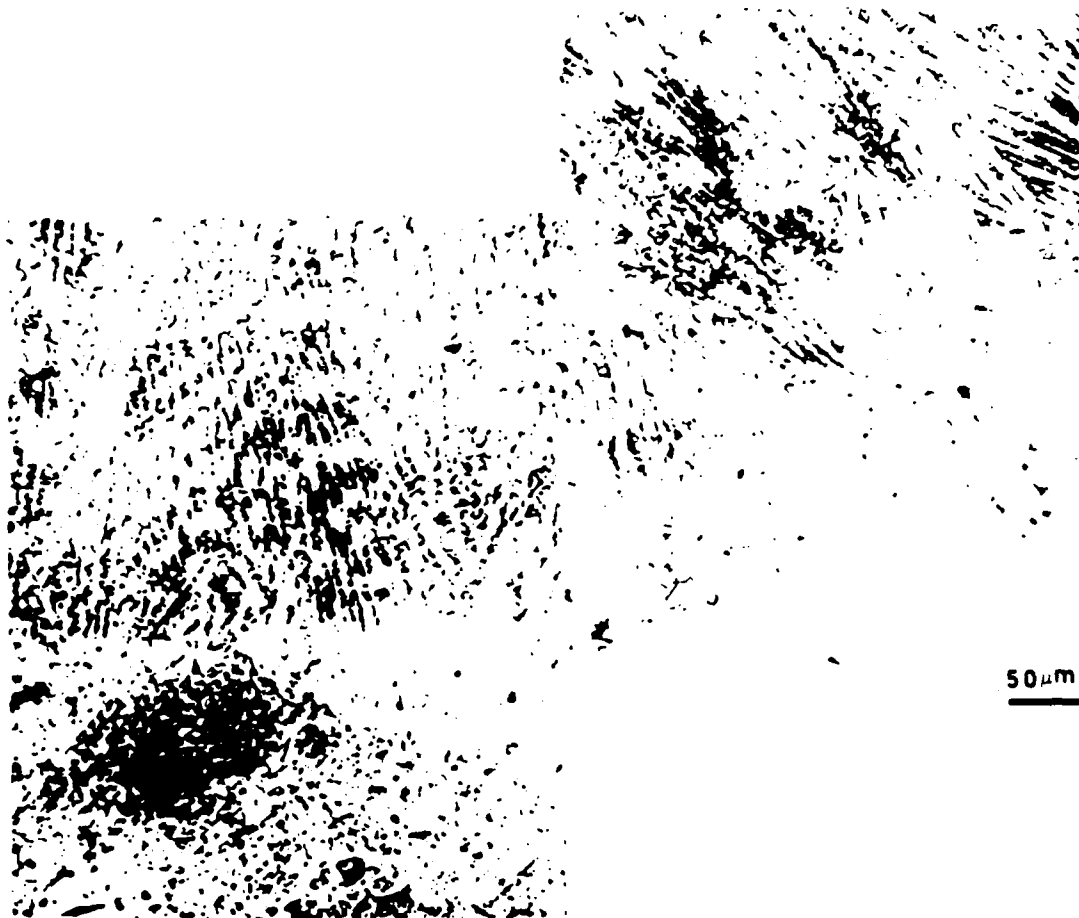


Figure 4 - Optical micrograph shows uniform microstructure in the laser clad region, good interaction between the laser clad substrate interface.

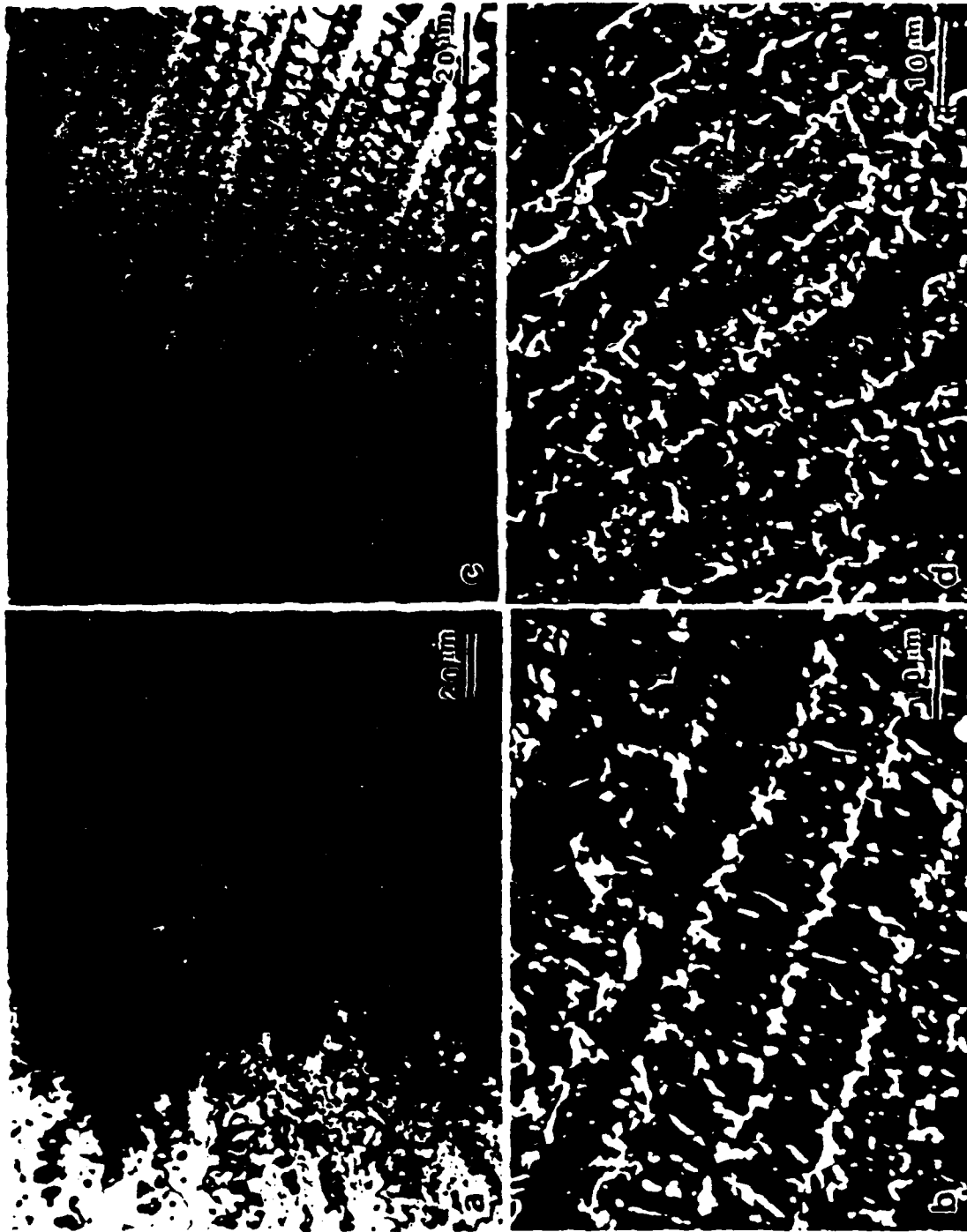


Figure 5 - Micrographs of laser clad regions for over-focused (a) and (b) and under-focused (b) and (c) laser beam (a) Optical: showing uniform distribution of second phase (b) SEM: showing distribution of Hf rich precipitates and undissolved Hf particles (c) Optical showing relatively large volume fraction of second phase (d) SEM: showing fine and large volume fraction of second phase as well as undissolved Hf particles.



Figure 6 - General survey of TEM sample of over focused laser clad alloy showing (a) and (b) undissolved Hf particles and Hf rich precipitates (c) dark field showing that matrix is having  $\text{Ni}_3\text{Al}$  ( $\gamma'$ ) type precipitate.

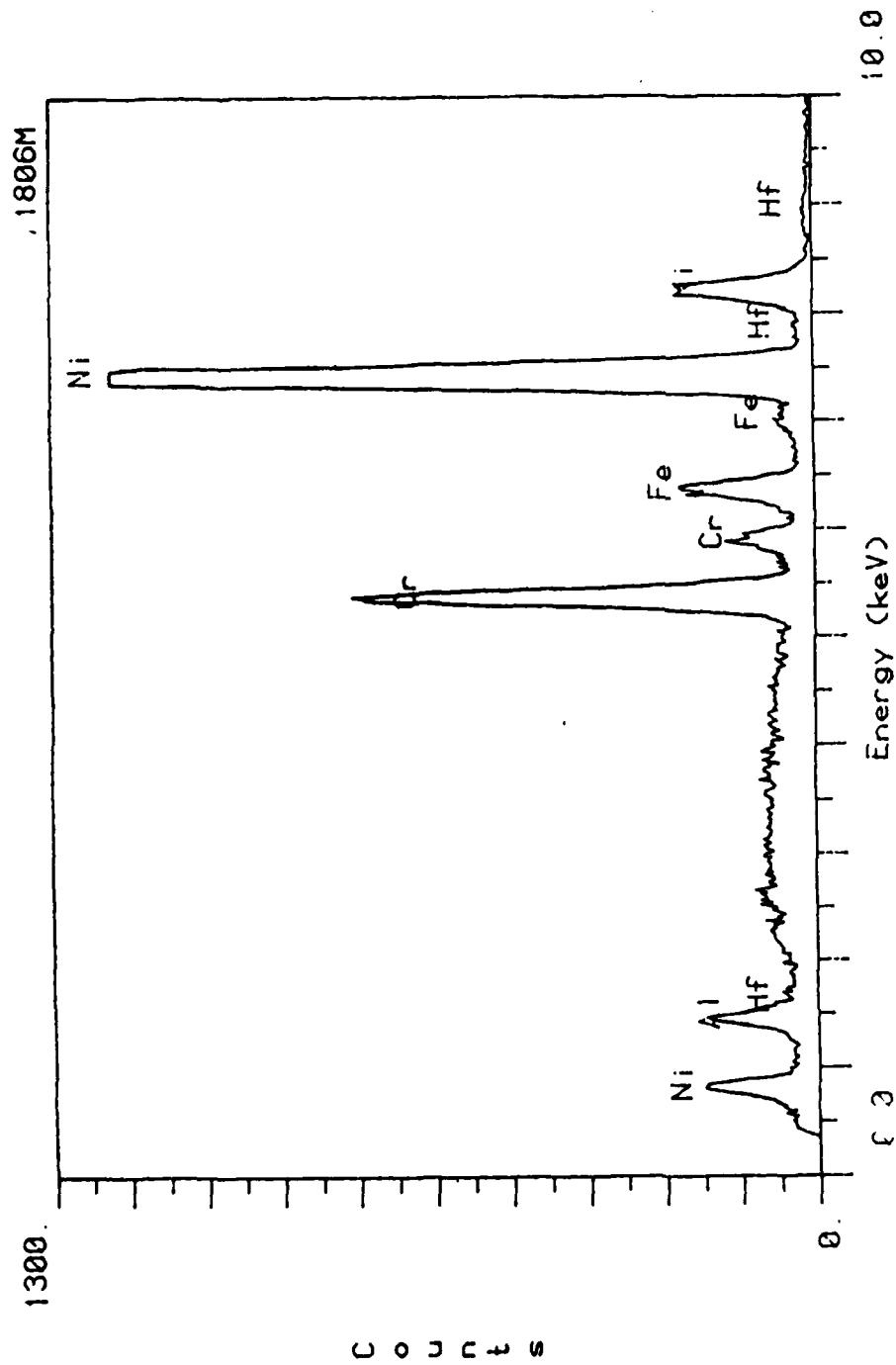


Figure 7 - STEM x-ray microanalysis from the matrix.

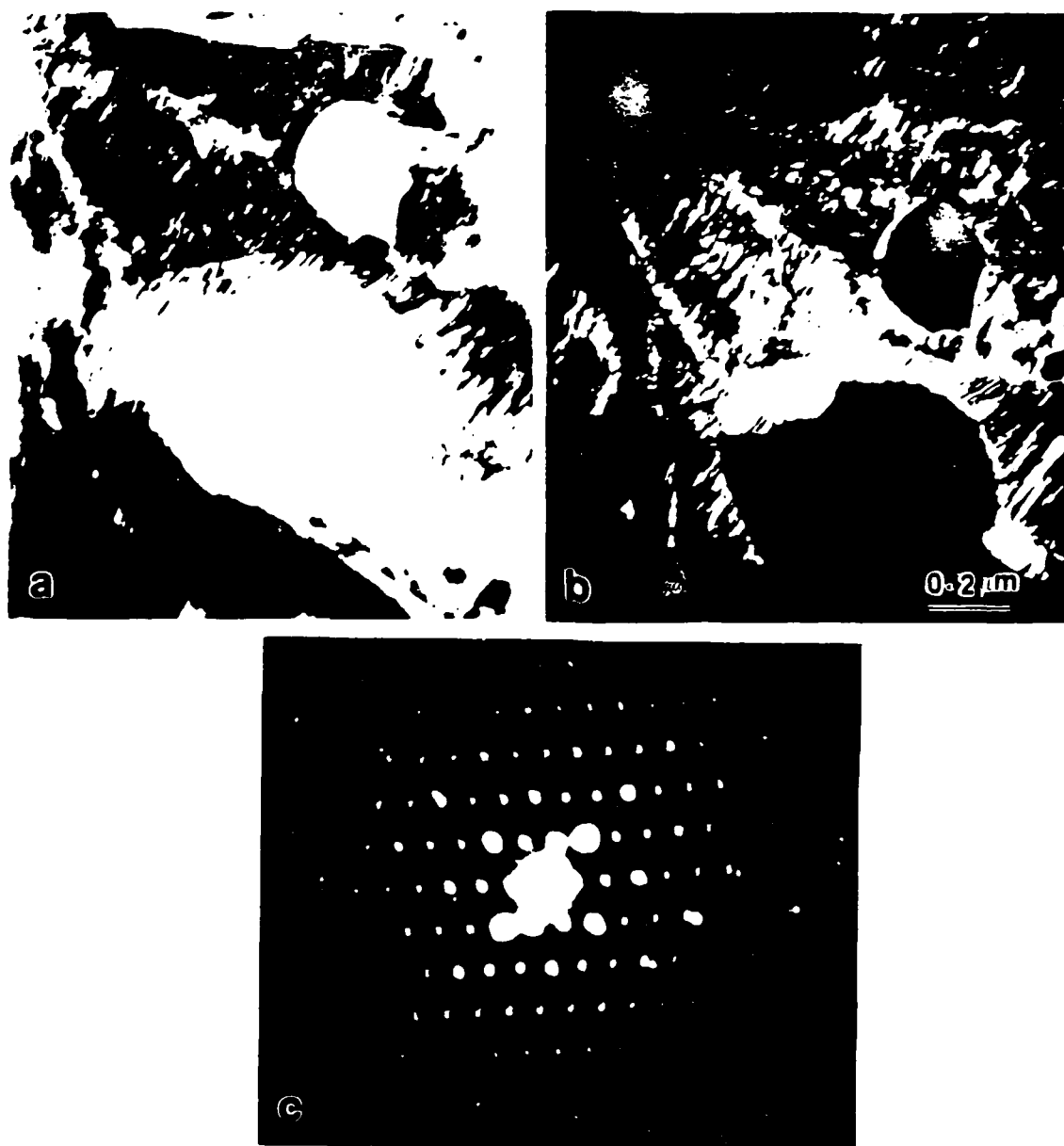


Figure 8 - Transmission electron micrograph of the laser clad sample showing the meta stable phases (a) bright field (b) dark field (c) corresponding diffraction pattern.



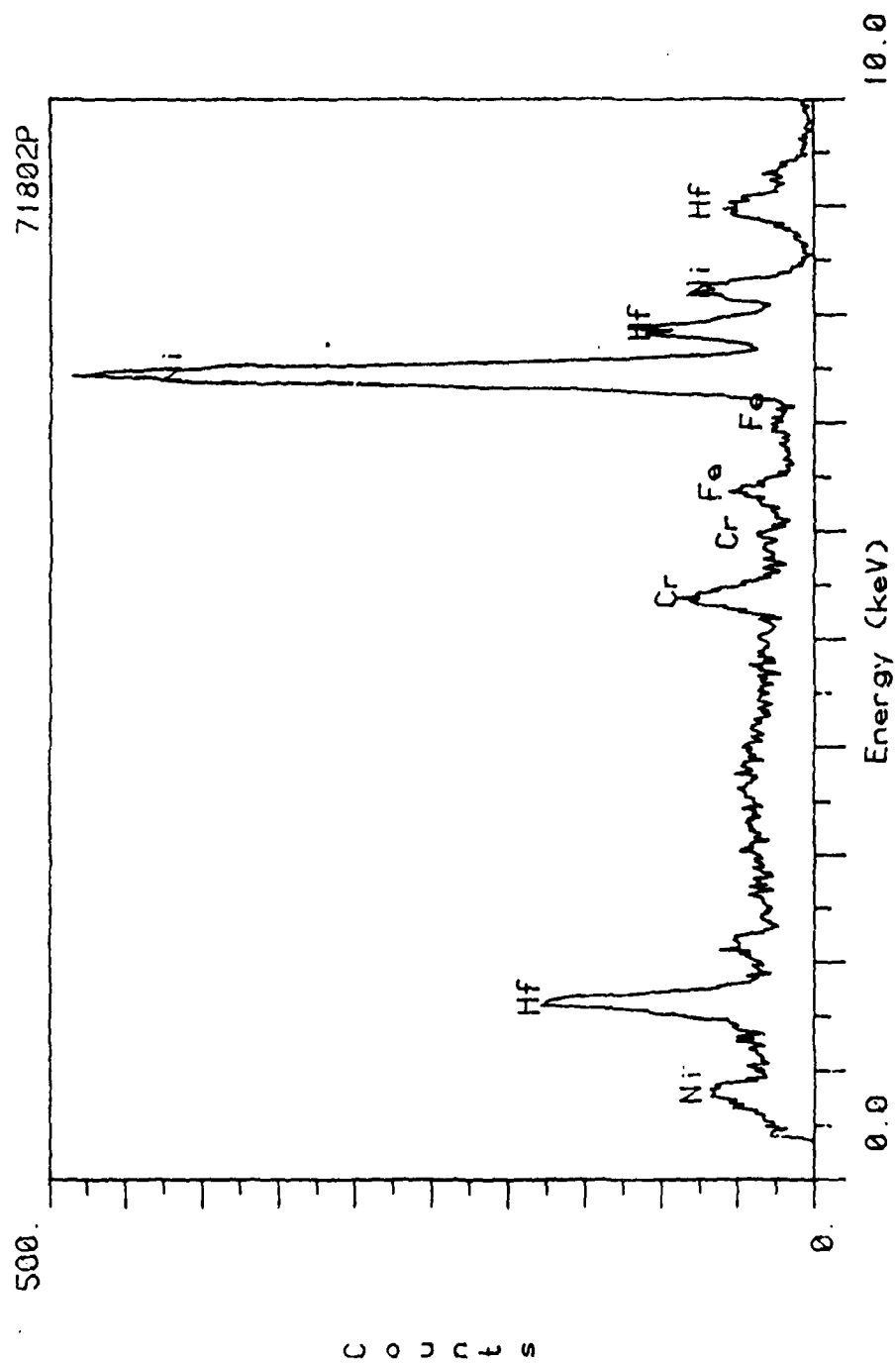


Figure 9 - STEM x-ray microanalysis from the second phase showing that the second phase is rich in Hf with small amount of Ni, Cr, and Al.

# LASER OPTICS DURING LASER CLADDING PROCESS

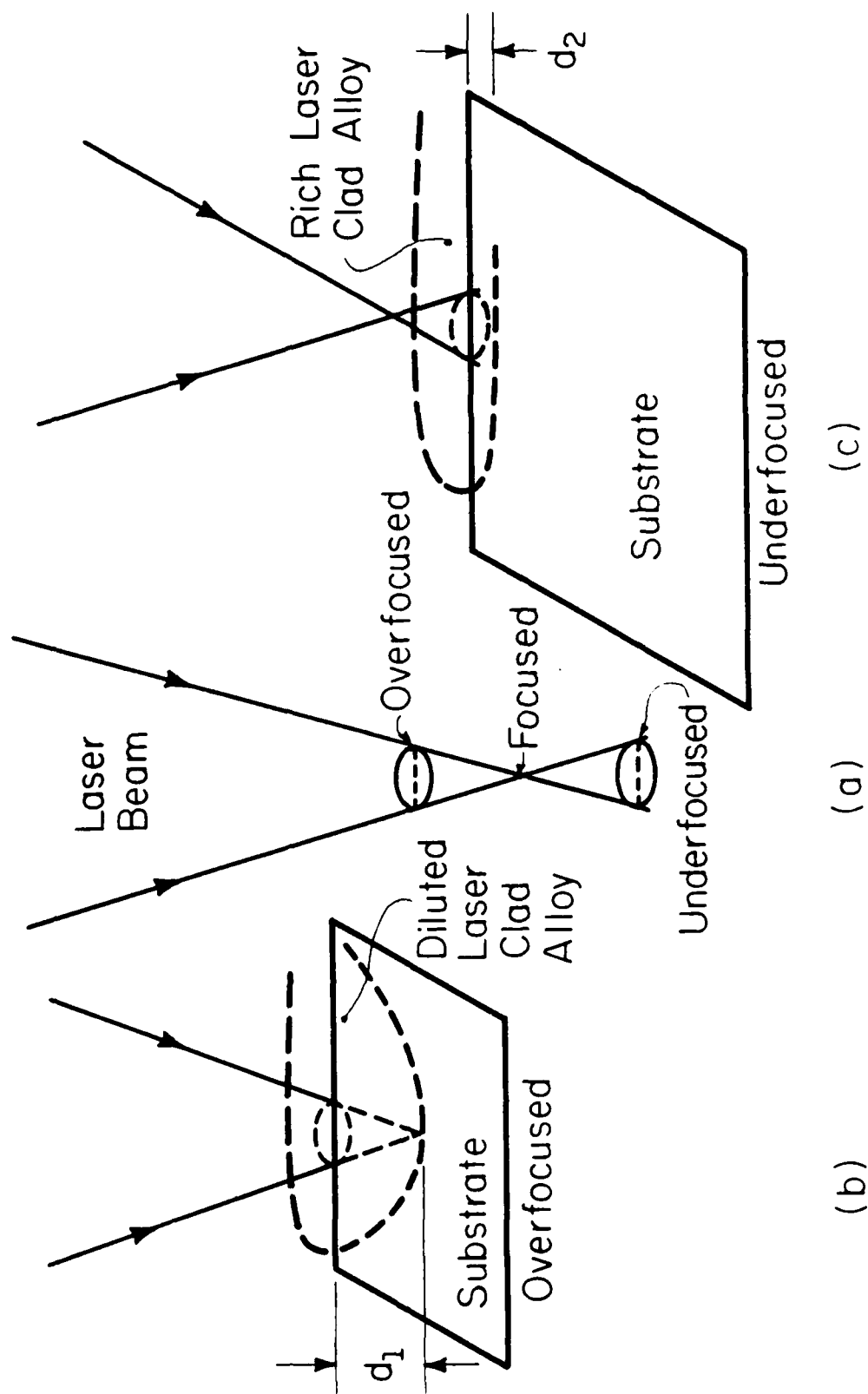


Figure 10 - Laser optics occurring during laser cladding process.

APPENDIX III  
ONE-DIMENSIONAL DIFFUSION MODEL FOR EXTENDED SOLID  
SOLUTION IN LASER CLADDING

A. Kar and J. Mazumder

Laser Aided Materials Processing Laboratory  
Department of Mechanical and Industrial Engineering  
University of Illinois at Urbana-Champaign  
1206 West Green Street  
Urbana, IL 61801

ABSTRACT

A mathematical model is presented for determining the composition of extended solid solution formed due to rapid cooling in laser cladding. This model considers diffusion mechanism for mass transport in a one-dimensional semi-infinite molten pool of the cladding material from which heat is removed by conduction through a one-dimensional semi-infinite solid substrate. The rate of solidification has been obtained by modeling the cooling process as a composite medium heat transfer problem. The discontinuity of the concentration field has been simulated using a nonequilibrium partition coefficient and then a non-similar exact solution for the mass transport equation has been obtained using a set of similarity variables which has been derived using Lie group theory.

## I. INTRODUCTION

Inherent rapid heating and cooling rate in laser surface modification provides an opportunity to produce novel materials without being restricted by equilibrium phase diagram. In laser cladding and alloying processes surface chemistry of materials can be significantly altered by simultaneous addition of alloying elements and their subsequent rapid solidification. High cooling rate ( $\approx 10^6$  K/sec) often leads to extension of solubility of the solute atoms and thus produce novel metastable materials. This process is dependent on energy, momentum and mass transport. Energy transport determines the rate of heating and cooling whereas momentum and mass transport determine the extent of mixing and final composition.

This paper is concerned with mathematical modeling of solute redistribution during laser cladding. The cladding material which could be a single element or a mixture of several elements is delivered to the surface of a solid substrate moving at a constant velocity, and is melted simultaneously using a laser beam. The molten pool of cladding material cools down mostly by conducting away heat through the solid substrate and by losing some of its energy to the ambient air by radiation and convection. A very good heat transfer model for CW laser material processing was developed by Mazumder and Steen<sup>1</sup>. Convection arising due to surface tension in a laser melted pool was considered by Chan, et al.<sup>2</sup>. They studied its effect on surface velocity, surface temperature, pool shape and the cooling rate. The distribution of matter by diffusion and convection, after it is delivered to such a pool was examined by Chande and Mazumder<sup>3</sup>.

There are not very many theoretical studies published in the literature to model laser surface cladding and alloying at a nonequilibrium cooling rate. For equilibrium partitioning of solute at the solid-liquid interface of

a binary alloy Tiller<sup>4</sup> et al. provided a quantitative analysis for transient and steady state conditions. In this work they avoided the heat transfer analysis by assuming that the process of solidification is taking place at a constant speed. Tien and Geiger<sup>5,6</sup> performed a heat transfer analysis of the solidification of a semi-infinite binary eutectic system. Muelhbauer<sup>7</sup> et al. obtained approximate solutions for the temperature distribution and the rate of phase change for one-dimensional solidification of a finite slab of a binary alloy. They considered a non-eutectic system where solidification takes place over a range of temperatures. Tsubaki and Boley<sup>8</sup> carried out both heat and mass transfer analysis for binary mixtures with concentration dependent freezing point and equilibrium partitioning of solute at the solid-liquid interface. In all these studies the objectives were either to analyze only the process of solidification under equilibrium as well as nonequilibrium cooling rate or to study the heat and mass transfer under equilibrium conditions using space-time variables. There has also been a considerable effort to predict the formation of extended solid solution under rapid cooling using thermodynamic variables such as free energy and chemical potential. The thermodynamic approach to solidification has been examined very well by Baker and Cahn<sup>9</sup>. Boettinger and Perepezko<sup>10</sup> have discussed the process of rapid solidification from the point of view of thermodynamics. Boettinger et al.<sup>11</sup> have also used the response function approach of Baker and Cahn<sup>9</sup> and stability analysis for microsegregation-free solidification. More about rapidly solidified materials can be found in Ref.<sup>12,13</sup>. The present study is concerned with the determination of composition of the extended solid solution formed due to rapid cooling in laser cladding using space-time variables.

## II. MATHEMATICAL MODEL

### Process Physics

The physical process of laser cladding involves pouring of cladding material powder onto the substrate to be clad by using a powder delivery system and simultaneously melting the powder using a laser beam. The pool of the cladding melt which is formed just below the laser beam solidifies by losing heat to the surrounding air, adjacent cladding and the solid substrate as it moves away from the laser beam due to the motion of the substrate. This produces a layer of cladding on the solid substrate and a liquid cladding pool below the laser beam (see Fig. 1(a)). Figure 1(a) shows an experimental set-up for laser surface cladding. The area ABCA shows the liquid pool of cladding melt which is in contact with the solid substrate along AB. It is also in contact along BC with the cladding formed on the substrate and the portion CA of the pool is exposed to an inert atmosphere to avoid oxidation of the cladding material. The shape of the strip of cladding will depend on the properties and the temperature of the cladding melt and the substrate, relative motion of the cladding with respect to the substrate and the characteristics of the cladding powder delivery system. In the present model the strip of cladding BCDEB (see Fig. 1(a)) has been considered to have semi-cylindrical shape (see Fig. 1(b)) and based on this the cladding radius ( $r_c$ ) is determined (see Eq. (18)). This paper is concerned with heat and mass transfer in the cladding melt ABCA to model extended solid solution during laser cladding. This liquid pool solidifies by conducting away heat to the substrate and to the solid cladding across AB and BC, respectively. Also, it loses some energy to the ambient inert gas across the free surface CA. But the loss of energy to the inert gas across the surface CA will be smaller than the heat loss due to conduction in the substrate and the cladding BCDEB.

However, the cladding BCDEB is formed from the liquid cladding melt just solidified and hence its temperature distribution is almost uniform and much higher than the temperature of the substrate which is immediately below the pool ABCA. So the heat loss across BC is much less compared to that across AB. Therefore, we can consider that the pool of cladding melt (ABCA) loses energy only in one direction through the surface at AB and to simplify the heat transfer calculations we assume that the pool extends up to infinity along AB as well as BC. Due to this assumption the cladding melt solidifies along AB and this freezing front moves upward in the direction of BC. The solid substrate has also been taken to be semi-infinite. The geometric configuration of this pool has been shown in Fig. 1(c) by rotating the pool 90 degrees in the clockwise direction. In this figure the freezing front has been shown to be planar. This is true when a pure metal solidifies. For a cladding melt of an alloy system, the freezing front develops curvature due to surface tension and also there could be dendrite and cellular growth at the solid-liquid interface. Moreover, rapid quenching may lead to growth due to spinodal decomposition and nucleation in the bulk of the liquid phase. The stability criterion of Mullins and Sekerka<sup>18</sup> of a planar interface during solidification of a dilute binary alloy shows that the planar interface will be unstable for both the nickel-hafnium and the nickel-aluminum systems considered in this study. The growth during solidification for these two cladding alloys has been shown in Figs. 10 and 11. Figure 10 shows the solidification of nickel-hafnium cladding powder on nickel substrate and the Fig. 11 shows the growth of nickel-aluminum cladding powder on nickel substrate. It can be seen from these two figures that there are dendritic growths for both cases, although the dendrites are less prominent for the nickel-aluminum alloy compared to those of nickel-hafnium system. Thus the

solid-liquid interface for nickel-aluminum system can be considered planar. Also for those systems where the size of dendrites is extremely small, the interface can be taken to be planar. Nevertheless, the dendrites will affect the diffusion of solute atoms at the freezing front. To simplify the mass transfer analysis, the freezing front has been assumed to be planar because the dendrite size is negligible for systems such as nickel-aluminum. Moreover, the trend predicted by the model is more important than the exact numerical values due to the paucity of high temperature materials data and simplifying assumptions. Besides this the present model has been developed based on a few more assumptions listed below.

- (1) The thermal conductivity and the thermal diffusivity for a mixture is the sum of the volume-averaged value of the respective transport properties of each element of the mixture,
- (2) The mass diffusivity of each element in the liquid phase is the average value of self-diffusivity over the room temperature and the initial temperature with modified activation energy for the mixture,
- (3) There is no diffusion of mass in the solid phase,
- (4) The solute segregated at the solid-liquid interface moves in the liquid phase by diffusion only,
- (5) The concentration of solute in the liquid alloy is equal to the nominal composition of the cladding powder mixture.
- (6) Change in solute concentration in the liquid phase does not alter its freezing point but it affects the heat flux across the solid-liquid interface, and
- (7) Only 50 percent of the laser energy has been assumed to be absorbed by the cladding material. Studies<sup>13</sup> show that the amount of laser energy absorbed by different materials is 37-60 percent.



Under these assumptions it is required to solve the one-dimensional heat conduction equation to obtain the speed of the freezing front which is then utilized to solve for the distribution of solute in the liquid phase. In laser processing of material usually the laser beam or the workpiece moves at a certain speed and when the laser melted pool is fully developed the speed of the freezing front and that of the laser beam or the workpiece are identical. This eliminates the need for solving the energy transport equation to determine the speed of solidification for fully developed pool. In the case of laser surface alloying the solidification progresses with segregation of solute atoms from the solid to the liquid phase and this alters the concentration of solute at the solid-liquid interface. This will affect the speed of the freezing front as well as the freezing point of the liquid. To take the former effect into account the energy transport equation has been solved while the latter one has been ignored in this model.

#### Mathematical Formulations

The governing equations for energy transport are:

(i) Region 1 (solid substrate)

$$\frac{\partial^2 T_1}{\partial x^2} = \frac{1}{\alpha_1} \frac{\partial T_1}{\partial t}; \quad t \geq 0, \quad -\infty < x \leq 0 \quad (1)$$

(ii) Region 2 (solidified cladding)

$$\frac{\partial^2 T_2}{\partial x^2} = \frac{1}{\alpha_2} \frac{\partial T_2}{\partial t}; \quad t > 0, \quad 0 \leq x \leq S(t) \quad (2)$$

(iii) Region 3 (liquid cladding)

$$\frac{\partial^2 T_3}{\partial x^2} = \frac{1}{\alpha_3} \frac{\partial T_3}{\partial t}; \quad t \geq 0, \quad S(t) \leq x < \infty \quad (3)$$

Here  $T_1$ ,  $T_2$ , and  $T_3$  are the temperatures and  $\alpha_1$ ,  $\alpha_2$ , and  $\alpha_3$  are thermal diffusivities of regions 1, 2, and 3, respectively.  $S(t)$  is the location of the solid-liquid interface at time  $t$ . If  $k_1$ ,  $k_2$ , and  $k_3$  are taken to be thermal conductivities of the regions 1, 2, and 3, respectively and if the ambient temperature, the freezing point of the cladding melt and the initial cladding pool mean temperature are denoted by  $T_0$ ,  $T_m$ , and  $T_f$ , respectively then the auxiliary conditions for the above heat transfer problem can be written as

$$T_1(-\infty, t) = T_0 \quad (4a)$$

$$T_1(x, 0) = T_0 \quad (4b)$$

$$\frac{\partial T_1}{\partial x} = \frac{k_2}{k_1} \frac{\partial T_2}{\partial x} \quad \text{at } x = 0 \quad (4c)$$

$$T_1(0, t) = T_2(0, t) \quad (4d)$$

$$T_2(x, t) = T_3(x, t) = T_m \quad \text{at } x = S(t) \quad (4e)$$

$$k_2 \frac{\partial T_2}{\partial x} - k_3 \frac{\partial T_3}{\partial x} = \rho L \frac{dS}{dt} \quad \text{at } x = S(t) \quad (4f)$$

where  $\rho$  is the density of the cladding melt and  $L$  is the latent heat of solidification. Note that the change in density, due to solidification, has been neglected here.

AD-A179 794

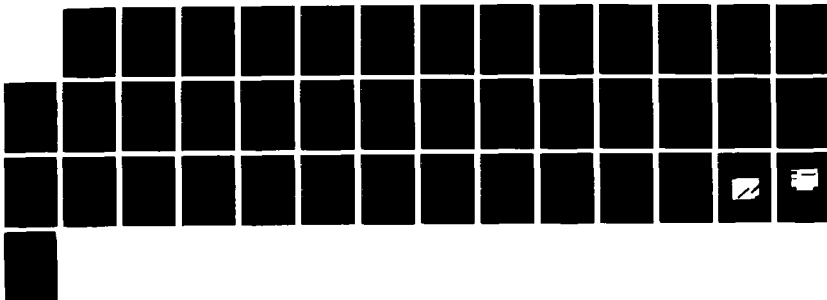
LASER CLADDING OF NI+CR+AL+RARE EARTH ALLOYS FOR  
IMPROVED OXIDATION AND H. (U) ILLINOIS UNIV AT URBANA  
DEPT OF MECHANICAL AND INDUSTRIAL ENG.  
J HAZUMDER ET AL. NOV 86 AFOSR-TR-87-0434

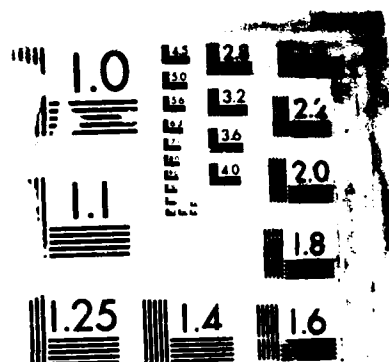
2/2

UNCLASSIFIED

F/G 11/6

NL





$$T_3(\infty, t) = T_f \quad (4g)$$

$$T_3(x, 0) = T_f \quad (4h)$$

$$S(0) = 0 \quad (4i)$$

The amount of solute rejected by the solidifying cladding and its transport in the liquid phase are governed by the following diffusion equation.

$$\frac{\partial C}{\partial t} - \frac{\gamma\sqrt{\alpha_3}}{\sqrt{t}} \frac{\partial C}{\partial x} = D \frac{\partial^2 C}{\partial x^2} \quad (5)$$

where  $c$  is the concentration of solute in the liquid phase,  $D$  is the mass diffusion coefficient and  $\gamma$  is a root of the transcendental Eq. (12). If  $C_0$  is the initial concentration of solute in the liquid phase and  $k_e$  denotes the equilibrium partition coefficient at the solid-liquid interface then the auxiliary conditions for the above mass transfer problem are

$$C(x, 0) = C_0 \quad (6a)$$

$$C(\infty, t) = C_0 \quad (6b)$$

$$D(1 + \frac{\gamma\sqrt{\alpha_3}}{\sqrt{t}} \beta) \frac{\partial C}{\partial x} = \frac{\gamma\sqrt{\alpha_3}}{\sqrt{t}} (k_e - 1)C \text{ at } x = 0 \quad (6c)$$

in a coordinate frame of reference moving with the solid-liquid interface. In the expression (6c),  $\beta = \lambda/D^*$ , where  $\lambda$  is the interatomic spacing and  $D^*$  is

the inter-diffusivity. This expression is obtained by incorporating into the mass balance equation at the solid-liquid interface an expression for non-equilibrium partition coefficient derived by Aziz<sup>15</sup>.

### Method of Solution

The multi-region heat transfer problem can be solved by the method used by Carslaw and Jaeger<sup>14</sup>. The temperature distributions in various regions are given by

$$T_1(\eta_1) = T_0 + \frac{\alpha_1 k_2 (T_m - T_0)}{\alpha_2 k_1 [1 + \text{Erf}(\gamma)]} [1 + \text{Erf}(\eta_1)] \quad (7)$$

$$T_2(\eta_2) = T_0 + \frac{\alpha_1 k_2 (T_m - T_0)}{\alpha_2 k_1 [1 + \text{Erf}(\gamma)]} \left[ 1 + \frac{\alpha_2 k_1}{\alpha_1 k_2} \text{Erf}(\eta_2) \right] \quad (8)$$

$$T_3(\eta_3) = T_f + \frac{T_m - T_f}{\text{Erfc}(\gamma)} \text{Erfc}(\eta_3) \quad (9)$$

where

$$\eta_i = x/2\sqrt{\alpha_i t}, \quad i = 1, 2, 3$$

and the location and the speed of the freezing front are given by

$$S(t) = 2\gamma (\alpha_3 t)^{1/2} \quad (10)$$

$$\dot{S}(t) = \gamma \sqrt{\alpha_3} / \sqrt{t} \quad (11)$$

Here  $k_2$  and  $\alpha_2$  are taken to be equal to  $k_3$  and  $\alpha_3$  respectively and  $\gamma$  is obtained from the following transcendental equation:

$$\frac{T_m - T_o}{1 + \text{Erf}(\gamma)} + \frac{T_m - T_f}{1 - \text{Erf}(\gamma)} = \sqrt{\pi} \rho \frac{\alpha_3}{k_3} L \gamma e^{\gamma^2} \quad (12)$$

After knowing the rate of formation of the solid phase the distribution of solute in the liquid phase can be obtained by solving the mass diffusion problem described by Eq. (5) and the associated conditions (6a-c). An exact solution for the above problem can be obtained by using similarity variables which are determined using Lie group theory. Details of this theory and its application for the solution of differential equations can be found<sup>16,17</sup>. Using this group theoretic approach the similarity variables can be found to be (See APPENDIX A).

$$y = \frac{x}{\sqrt{t}} \text{ and } \psi_n = \frac{C(\sqrt{t})^n}{A_n}, \quad n = 0, 1, 2, \dots, \infty \quad (13)$$

where  $A_n$ 's are constants to be determined later. To satisfy the boundary condition (6c) using these new variables the principle of superposition will be used by defining the concentration  $C$  as

$$C = \sum_{n=0}^{\infty} A_n \psi_n \frac{1}{(\sqrt{t})^n} \quad (14)$$

Using (13) and (14) the Eq. (5) and the auxiliary conditions (6a-c) can be written as

$$2D \frac{d^2 \psi_n}{dy^2} + (y + 2\gamma\sqrt{\alpha_3}) \frac{d \psi_n}{dy} + n \psi_n = 0 \quad (15)$$

$$\psi_n (y \rightarrow \infty) = C_o \delta_{no} \quad (16a)$$

$$\frac{d\psi_n}{dy} - \frac{\gamma\sqrt{\alpha_3} (k_e - 1)}{D} \psi_n = (1 - \delta_{no}) \frac{\gamma\sqrt{\alpha_3} (k_e - 1)}{D} \sum_{j=0}^{n-1} (-1)^{n-j} \psi_j \quad (16b)$$

where  $\delta_{no}$  is the Kronecker delta and  $A_n$ 's of expression (14) are given by

$$A_n = (8r\sqrt{\alpha_3})^n, \quad n = 0, 1, 2, \dots, \infty$$

For this problem four terms of the series (14) were computed by determining  $\psi_0$ ,  $\psi_1$ ,  $\psi_2$  and  $\psi_3$  from Eq. (15). These solutions are (see APPENDIX B)

$$\psi_0(r) = C_0 \left[ 1 - \frac{G \operatorname{Erfc}(\sqrt{2} r)}{(\sqrt{8/\pi}) \operatorname{Exp}(-4\gamma^2 \alpha_3/D) + G \operatorname{Erfc}(2\gamma\sqrt{\alpha_3}/D)} \right]$$

$$\psi_1(r) = - \frac{G \psi_0(r_0)}{r_0 + G} e^{-(r^2 - r_0^2)/2}$$

$$\psi_2(r) = - \frac{G[\psi_0(r_0) - \psi_1(r_0)]}{r_0 G + (r_0^2 - 1)} \cdot r e^{-(r^2 - r_0^2)/2}$$

$$\psi_3(r) = - \frac{G[\psi_0(r_0) - \psi_1(r_0) + \psi_2(r_0)]}{(r_0^2 - 1)G + r_0(3 - r_0^2)} (r^2 - 1) e^{-(r^2 - r_0^2)/2}$$

where

$$G = \gamma\sqrt{\alpha_3} (k_e - 1) \sqrt{2/D}, \quad r = (y + 2\gamma\sqrt{\alpha_3})/\sqrt{2D} \quad \text{and} \quad r_0 = \gamma\sqrt{2\alpha_3}/D$$



Using these expressions for  $\psi_0$ ,  $\psi_1$ ,  $\psi_2$  and  $\psi_3$  the concentration of solute in the liquid phase was computed using the Eq. (14) and then the corresponding concentration in the solid phase ( $C_s$ ) was obtained using the following expression derived by Aziz<sup>15</sup> for nonequilibrium partition coefficient.

$$\frac{C_s}{C} = \frac{\dot{S}(t)_B + k_e}{\dot{S}(t)_B + 1} \quad (17)$$

In the present model the inter-diffusivity  $D^*$  is taken to be equal to the mass diffusivity and the interatomic spacing  $\lambda$  is taken to be  $4\text{\AA}$  which is the average diameter of an atom. Other physical properties for the alloy were computed at its nominal composition using the following relationships:

$$\rho = 1 / \sum_{j=1}^n W_j / \rho_j$$

where  $n$  = total number of elements present in the liquid pool of cladding

$$L = \sum_{j=1}^n W_j L_j$$

$$\bar{k}_i(T) = \rho \sum_{j=1}^n \frac{W_j}{\rho_j} \bar{k}_{ij}(T)$$

$$k_i = \int_{T_0}^{T_f} \bar{k}_i(T) dT / (T_f - T_0)$$

$$\bar{C}_p(T) = \sum_{j=1}^n W_j \bar{C}_{pj}(T)$$

$$C_p = \int_{T_0}^{T_m} \bar{C}_p(T) dT / (T_m - T_0)$$

$$\bar{\alpha}_i(T) = \rho \sum_{j=1}^n \frac{W_j}{\rho_j} \bar{\alpha}_{ij}(T)$$

$$\alpha_i = \int_{T_0}^{T_f} \bar{\alpha}_i(T) dT / (T_f - T_0)$$

and the diffusion coefficient for the  $j$ -th solute in the liquid phase is

$$D_j = \int_{T_0}^{T_f} D_{oj} e^{-\frac{\bar{Q}}{RT}} dT / (T_f - T_0)$$

where  $D_{oj}$  is the self-diffusion coefficient of the  $j$ -th element and  $\bar{Q}$  is the activation energy for the mixture given by

$$\bar{Q} = \sum_{j=1}^n w_j Q_j$$

In all these expressions for thermophysical properties of the cladding powder mixture, the index  $i = 1, 2, 3$  refers to the solid substrate, solidified cladding and the liquid cladding region, respectively, and  $j = 1, 2, 3, \dots$ , refers to the  $j$ -th element of the cladding powder mixture. Here,  $w_j$  and  $w_j$  are the weight fraction and the mole fraction of the  $j$ -th element, respectively.  $\bar{k}_{ij}$  and  $\bar{\alpha}_{ij}$  denote respectively the thermal conductivity and the thermal diffusivity of the  $j$ -th element in the  $i$ -th region.  $C_{pj}$  is the specific heat of the  $j$ -th element. The thickness of the cladding can be determined by taking an over-all energy balance which yields the following expression for the radius ( $r_c$ ) of the semi-cylindrical strip of cladding:

$$r_c = \left[ \frac{2fP}{\{(T_f - T_0) C_p + L\} \pi v \rho} \right]^{\frac{1}{2}} \quad (18)$$

where  $f$  is the fraction of laser energy absorbed by the cladding material,  $P$  is the power of the laser beam incident on the material, and  $v$  is the speed of

the workpiece which can be related to the volumetric rate ( $q$ ) of powder delivery by

$$q = \frac{1}{2} \pi r_c^2 v \quad (19)$$

assuming that all of the delivered powder form cladding on the substrate.

### III. RESULTS AND DISCUSSION

#### Experimental Verification:

The results of the above model was compared with experimental data. Laser cladding was performed on nickel substrate with two different cladding materials of nominal composition 74% Ni and 26% Hf in one case and 74% Ni and 26% Al in the other case. The solid substrate was clad with these cladding materials which take the shape of an approximately semi-cylindrical strip of metal on the substrate (see Fig. 1(b)). Electron Probe Micro Analysis of these samples shows the concentration of Hf and Al in the matrix of Ni in excess of what is predicted by the equilibrium phase diagram. The present model predicts the composition of the extended solid solution quite well. These results have been presented in the Table I for  $T_f = 2035^\circ\text{K}$  for the Ni-Hf alloy and  $T_f = 1907^\circ\text{K}$  for Ni-Al alloy.

Table I Comparison of Theoretical Results with Experimental Results of Extended Solid Solution

Laser Power (Kw)	Laser Beam Diameter (mm)	Speed of the Work-piece (Inch/min)	Nominal Composition of the cladding material (wt. %)	Composition in the solid solution (wt. %)	
				Theoretical Results	Experimental Results
5	3	50	74% Ni, 26% Hf	3.05% Hf	3.58% Hf
5	3	50	74% Ni, 26% Al	27.3% Al	22% Al

The prediction of composition of the extended solid solution based on the present model is within 30% of the experimental results. This discrepancy may be due to some of the assumptions of this model. For example, solidification has been assumed to take place at a constant temperature which has been taken to be the freezing point of the cladding material at its nominal composition. But it is well known that the change in composition in the liquid phase will alter its freezing point. Also the present model utilizes an expression (17) for nonequilibrium partition coefficient which is applicable to dilute solution. Apart from these the presence of a two-phase zone between the solidus and the liquidus lines and the surface tension driven flow causing convection in the liquid pool will affect the mixing of solute in the liquid phase and thus alter its composition in the solid phase. Paucity of high temperature liquid metal data also contributes to the numerical error. However, the objective of this study is to determine the trend and thus understand the underlying process physics.

#### Parametric Results

The above model was used to study the effect of various important process parameters such as the cooling rate, cladding powder delivery rate on the composition of hafnium in nickel matrix. Results were obtained for ambient temperature  $T_0 = 293^\circ\text{K}$  and some of the process parameters were computed based on a laser beam of diameter 3 mm. Besides this the initial temperature of the cladding melt was chosen as an independent parameter for one set of results and the cladding thickness for another set of results for different values of laser power and the velocity of the workpiece. These parameters have been listed in Tables I and II.

Table II List of independent parameters ( $v$ ,  $P$ ,  $T_f$ ) and dependent parameters ( $r_C$ ,  $q$ )

[illegible]

Table II (continued)

Independent Parameters	Workpiece Velocity (Inch/min)	50								
		5			6			7		
	Laser Power (kW)									
	Initial Temperature (°K)	2000	2200	2400	2000	2200	2400	2000	2200	2400
Calculated Values	Cladding Thickness (mm)	2.76	2.64	2.54	3.02	2.90	2.78	3.27	3.13	3.00
	Powder Delivery Rate (mm <sup>3</sup> /sec)	253.3	231.7	214.5	303.2	279.6	257.0	355.5	325.7	299.2

Table III List of independent parameters ( $v$ ,  $p$ ,  $r_c$ ) and dependent parameters ( $T_f, q$ )

Independent Parameters	Workpiece Velocity (Inch/min)	30								
	Laser Power (kW)	5			6			7		
	Cladding Thickness (mm)	3.45	3.35	3.25	3.95	3.80	3.65	4.15	4.00	3.85
Calculated Values	Initial Temperature (°K)	2149	2292	2449	1948	2123	2320	2072	2247	2443
	Powder Delivery Rate (mm <sup>3</sup> /sec)	237.4	223.9	210.7	311.3	288.1	265.8	343.6	319.2	295.7
Independent Parameters	Workpiece Velocity (Inch/min)	40								
	Laser Power (kW)	5			6			7		
	Cladding Thickness (mm)	3.00	2.85	3.15	3.45	3.30	3.15	3.70	3.55	3.40
Calculated Values	Initial Temperature (°K)	2129	2383	1911	1911	2110	2337	1942	2129	2341
	Powder Delivery Rate (mm <sup>3</sup> /sec)	263.9	239.4	216.1	316.6	289.7	263.9	364.1	335.2	307.5



Table III (Continued)

Independent Parameters	Workpiece Velocity (Inch/min)	50								
	Laser Power (kW)	5			6			7		
Independent Parameters	Cladding Thickness (mm)	2.75	2.65	2.60	3.00	2.90	2.80	3.30	3.15	3.00
Calculated Values	Initial Temperature (°K)	2016	2189	2382	2035	2194	2369	1954	2167	2142
	Powder Delivery Rate (mm <sup>3</sup> /sec)	251.4	233.5	216.2	299.2	279.6	260.7	362.1	329.9	299.2

Results obtained based on the parameters of the Table II have been presented in Figs. 2 through 4. As can be seen in Fig. 2 the cooling rate at the solid-liquid interface drops sharply to almost equilibrium cooling rate within one second after the cladding melt starts freezing. Also it can be observed that the magnitude of the cooling rate of the liquid phase at the freezing point is higher for lower initial temperature of the liquid cladding material. This is to be expected because when the initial temperature  $T_f$  is lower the amount of thermal energy of the melt is less compared to when it is at a higher temperature. So when cladding materials of two different temperatures are brought in contact with a solid substrate of temperature 293°K, the melt of lower temperature will have to lose lesser amount of energy than the one which is at a higher temperature. For example, let us take a melt of temperature 2000°K and another one of 2200°K. When they are brought in contact with a solid substrate of temperature 293°K the first melt will cool down from 2000°K to the freezing point by conducting away its heat through the substrate with an initial driving force for heat transfer proportional to  $2000 - 293 = 1707^\circ\text{K}$ . The second melt on the other hand will first require some time to cool from 2200°K to 2000°K during which time the temperature of the solid substrate will rise from its initial temperature 293°K. As a result of this the melt will now have to cool from 2000°K to the freezing point with an initial driving force smaller than that for the first melt.

The extension of solubility in solid solution has also been studied as a function of cooling rate. It can be seen from Fig. 3 that the higher the cooling rate the higher is the composition of hafnium in nickel matrix. However it should be noted that same cooling rate for different initial melt temperature does not result in the same composition of hafnium in the solid solution. This is because the higher the initial temperature the longer it takes

to first form the solid phase at the interface of the substrate and the liquid cladding material and during this time the solute atoms diffuse away from the interface causing a formation of alloy lean with solute atoms. This is true if there is no adsorption between the solute atoms and the solid substrate. Another important process parameter considered in this study is the powder delivery rate. Its effect on the concentration of hafnium for different laser energy fluxes has been shown in Fig. 4. The shift in the concentration curves to the right as the laser energy flux and the cladding powder delivery rate are increased confirms the fact that an increasing powder delivery rate causes more cladding material on the substrate which requires more laser energy to melt in order to yield a pre-determined concentration of solute in the alloy. Powder delivery rate is a very important process parameter since it is related to the cladding thickness and the velocity of the workpiece as well as the initial temperature of the cladding material. It is equal to  $\frac{1}{2} \pi r_C^2 v$  and using this in the expression for  $r_C$  given above it can be related to  $T_f$ . Thus if the powder delivery rate is known then  $T_f$  is also known and then the velocity of the workpiece can be determined for a desired cladding thickness. It can also be related to laser-cladding interaction time by noting that  $\frac{1}{2} \pi r_C^2 v = \frac{1}{2} \pi r_C^2 B / (B/v)$  which is a ratio of cladding volume based on the beam diameter ( $B$ ) to the interaction time. In otherwords the powder delivery rate is equal to the cladding volume based on the beam diameter for unit interaction time.

Also, the weight-percentage of hafnium in the nickel-hafnium alloy and the initiated temperature of the cladding melt were computed for a set of independent parameters ( $v$ ,  $P$ ,  $r_C$ ) listed in Table III. These results have been shown in Figs. 5 through 9, for various values of laser-cladding interaction time and laser energy flux. Figure 5 provides a set of very important results

that are useful for selecting the process parameters to clad a material with an alloy of pre-determined composition and thickness. For example, the choice of the cladding thickness and the composition of the cladding alloy uniquely defines a curve as shown in Fig. 5 which corresponds to a particular value of the laser energy flux and the interaction time. The latter two parameters are related to the laser power,  $p$ , laser beam diameter,  $B$ , and velocity of the workpiece,  $v$ . Thus if one of the three process parameters,  $P$ ,  $B$ , or  $v$ , is selected along with  $r_c$  and the composition of the cladding alloy, then the other two parameters can be obtained from Fig. 5. After this, the volumetric rate of cladding powder delivery can be determined from Eq. (19). Figures 6, 7, 8 and 9 show the effect of cladding thickness on the initial temperature of the cladding melt and the effect of the latter variable on the cooling rate. As can be seen from Fig. 6, the initial temperature decreases with the increase in  $r_c$  for the same laser energy flux and the interaction time and Figs. 7, 8 and 9 show that the lower the initial melt temperature, the higher the cooling rate. Thus if a higher cooling rate is needed, the initial melt temperature has to be chosen from the results of Figs. 7, 8 and 9 and then Fig. 6 has to be used to determine the cladding thickness.

## CONCLUSION

The present work examines the extension of solid solubility based on the transport of energy and mass. Solute transport has been considered to take place only in the liquid phase while the energy transport has been considered in both solid and liquid phases. Effect of nonequilibrium cooling rate on solute segregation at the freezing front has been taken into account by considering a nonequilibrium partition coefficient. Using this the mass transfer problem has been solved analytically in a frame of reference moving with the freezing front with a velocity determined from the heat transfer problem. These mathematical solutions have been utilized to study the effect of various process parameters on the concentration of solute in an alloy. As mentioned above the cooling rate is found to drop sharply within one second after the solidification starts and it is also higher for lower initial melt temperature. The hafnium concentration in the nickel-hafnium alloy is found to be higher for higher cooling rate and also more laser energy is required to obtain an alloy of a given composition at a higher powder delivery rate than that for a lower rate of powder delivery.

Also it can be seen from Fig. 4 that the composition of hafnium does not depend on the parameters called laser-cladding interaction time, defined by the ratio of the laser beam diameter to the velocity of the workpiece, whereas it does depend on the interaction time as shown in Fig. 5. This is because the set of initial temperature is the same (see Table II) for the former case but it is different (see Table III) for the latter one. Another interesting feature that can be observed from the Fig. 5 is that same composition of hafnium is obtained in the alloy for different cladding thickness by varying the laser energy flux and the interaction time. This is because the initial temperature of the cladding material and hence the cooling rate are the same even

though other parameters are different (see Figs. 6, through 9). So it can be concluded that the choice of the initial temperature determines the composition of the alloy. Once the initial temperature of the cladding melt is fixed, other process parameters can be determined by selecting any two of the three parameters,  $r_c$ ,  $v$ , and  $P$  and the third one will then have to be determined from Eq. (18).

## ACKNOWLEDGMENTS

This work was made possible by a grant from Air Force of Scientific Research (Grant No. AFOSR 85-0333). Dr. A. Rosenstein is the program manager. The authors also like to acknowledge the help provided by Dr. J. Singh for electron probe microanalysis and the micrographs.

## REFERENCES

1. J. Mazumder, and W. M. Steen, *J. Appl. Phys.*, 51, 941 (1980).
2. C. Chan, J. Mazumder, and M. M. Chen, *Met. Trans. A.*, 15A, 2175 (1984).
3. T. Chande, and J. Mazumder, *J. Appl. Phys.*, 57, 2226 (1985).
4. W. A. Tiller, K. A. Jackson, J. W. Rutter, and B. Chalmers, *Acta Meta.*, 1, 428 (1953).
5. R. H. Tien, and G. E. Geiger, *J. Heat Transfer*, 89C, 230 (1967).
6. R. H. Tien, and G. E. Geiger, *J. Heat Transfer*, 90C, 27 (1968).
7. J. C. Muelhbauer, J. D. Hatcher, D. W. Lyons, and J. E. Sunderland, *J. Heat Transfer*, 95C, 324 (1973).
8. T. Trubaki, and B. A. Boley, *Mech. Res. Comm.*, 4, 115 (1977).
9. J. C. Baker, and J. W. Cahn, in *Solidification*, papers presented at a seminar of the American Society for Metals, Seminar Coordinated by T. J. Hughel, and G. F. Bolling (American Society for Metals, Metals Park, OH, 1971) pp. 23-58.
10. W. J. Boettinger, and J. H. Perepezko, in *Proceedings of Rapidly Solidified Crystalline Alloys*, edited by F. K. Das, B. H. Kear, and C. M. Adam (Metallurgical Society of American Institute of Metallurgical Engineers, Warrendale, PA, 1986), pp. 21-58.
11. W. J. Boettinger, S. R. Coriell, and R. F. Sekerka, *R. F.*, *Mat. Sci. Eng.*, 65, 27 (1984).
12. W. J. Boettinger, in *Proceedings of Rapidly Solidified Amorphous and Crystalline Alloys*, edited by B. H. Kear, B. C. Giessen, and M. Cohen (North-Holland, New York, 1982), Vol. 8, pp. 15-31.
13. L. J. Li, and J. Mazumder, in *Proceedings of Laser Processing of Materials*, edited by K. Mukherjee, and J. Mazumder, (Metallurgical Society of American Institute of Metallurgical Engineers, Warrendale, PA, 1985), pp. 35-50.
14. H. S. Carslaw, and J. C. Jaeger, *Conduction of Heat in Solids*, 2nd. Ed., (Clarendon Press, London, 1959), pp. 282-296.
15. M. J. Aziz, *J. Appl. Phys.*, 53, 1158 (1982).
16. G. W. Bluman, and G. D. Cole, *Similarity Methods for Differential Equations*, (Springer-Verlag, New York, 1974).
17. L. V. Ovsiannikov, *Group Analysis of Differential Equations*, (Translation edited by W. F. Ames), 1st ed. (Academic Press, New York, 1982).
18. W. W. Mullins, and R. F. Sekerka, *J. Appl. Phys.*, 35, 444 (1964).



## APPENDIX A

The similarity variables given by the expression (13) can be obtained by using Lie group theory. To apply this theory to Eq. (5) let us define

$$K = \gamma \sqrt{a_3}$$

and

$$\theta = \sqrt{t}.$$

This transforms Eq. (5) to the following form

$$\frac{1}{2} C_{\theta} - K C_x - \theta C_{xx} = 0 \quad (\text{A.1})$$

where the subscripts refer to the partial differentiation of  $C$  with respect to the subscript variable.

We define the group generator for (A.1) as

$$U = \xi(x, \theta, C) \frac{\partial}{\partial x} + \eta(x, \theta, C) \frac{\partial}{\partial \theta} + \delta(x, \theta, C) \frac{\partial}{\partial C} \quad (\text{A.2})$$

Then the twice-extended operator becomes

$$\begin{aligned} U'' = & \xi \frac{\partial}{\partial x} + \eta \frac{\partial}{\partial \theta} + \delta \frac{\partial}{\partial C} + \xi' \frac{\partial}{\partial C_{\theta}} + \xi \frac{\partial}{\partial C_x} + \eta'' \frac{\partial}{\partial C_{\theta\theta}} + \xi'' \frac{\partial}{\partial C_{xx}} + \\ & + \gamma'' \frac{\partial}{\partial C_{x\theta}} \end{aligned} \quad (\text{A.3})$$

where

$$\eta' = \delta_{\theta} + \delta_C C_{\theta} - C_X \xi_{\theta} - C_X C_{\theta} \xi_C - C_{\theta} \eta_{\theta} - C_{\theta}^2 \eta_C$$

$$\xi' = \delta_X + \delta_C C_X - C_X \xi_X - C_X C_{\theta} \eta_C - C_X C_{\theta} \eta_C - C_{\theta} \eta_X - C_X^2 \xi_C$$

$$\begin{aligned} \eta'' = & -C_{X\theta}(\xi_{\theta} + \xi_C C_{\theta}) - C_{\theta\theta}(\eta_{\theta} + \eta_C C_{\theta}) + \delta_{\theta\theta} + \delta_{\theta C} C_{\theta} + \delta_C C_{\theta\theta} + \\ & + C_{\theta}(\delta_{C\theta} + \delta_{CC} C_{\theta}) - C_{X\theta} \xi_{\theta} - C_X(\xi_{\theta\theta} + \xi_{\theta C} C_{\theta}) - C_{X\theta} \xi_C C_{\theta} - \\ & - C_X C_{\theta}(\xi_{C\theta} + \xi_{CC} C_{\theta}) \\ & - C_{\theta\theta} C_{\theta}(\eta_{\theta} + \xi_C C_X) - C_{\theta}(\eta_{\theta\theta} + \eta_{\theta C} C_{\theta}) - 2\eta_C C_{\theta} C_{\theta\theta} - \\ & - C_{\theta}^2(\eta_{C\theta} + \eta_{CC} C_{\theta}) \end{aligned}$$

$$\begin{aligned} \xi'' = & -C_{XX}(\xi_X + \xi_C C_X) - C_{X\theta}(\eta_X + \eta_C C_X) + \delta_{XX} \\ & + 2C_X \delta_{CX} + C_X^2 \delta_{CC} + \delta_C C_{XX} - C_X(\xi_{XX} + \xi_{XC} C_X) - \\ & - \xi_X C_{XX} - C_X^2(\xi_{CX} + \xi_{CC} C_X) - 2C_X C_{XX} \xi_C - C_{\theta}(\eta_{XX} + \eta_{XC} C_X) - \\ & - C_{\theta X}(\eta_X + C_X \eta_C) - C_{\theta} C_{XX} \eta_C - C_{\theta} C_X(\eta_{CX} + \eta_{CC} C_X) \end{aligned}$$

$$\begin{aligned}
Y'' = & -C_{XX}(\xi_\theta + \xi_C C_\theta) - C_{X\theta}(\eta_\theta + \eta_C C_\theta) + \delta_{X\theta} + \delta_{XC} C_\theta + \\
& + \delta_C C_{X\theta} + C_X(\delta_{C\theta} + \delta_{CC} C_\theta) - \xi_X C_{X\theta} - C_X(\xi_{X\theta} + \xi_{XC} C_\theta) - \\
& - 2C_X C_{X\theta} \xi_C - C_X^2(\xi_{C\theta} + \xi_{CC} C_\theta) - \eta_X C_{\theta\theta} - C_\theta(\eta_{X\theta} + \eta_{XC} C_\theta) - \\
& - \eta_C(C_X C_{\theta\theta} + C_\theta C_{X\theta}) - C_X C_\theta(\eta_{C\theta} + \eta_{CC} C_\theta)
\end{aligned}$$

For Eq. (A.1) to admit any group, it is required that it be invariant relative to the twice-extended operator, that is

$$U''(\frac{1}{2} C_\theta - KC_X - \theta C_{XX}) \equiv 0 \quad (A.4)$$

on the manifold defined by Eq. (A.1).

When the expression (A.4) is expanded and the coefficients of  $C_X$ ,  $C_\theta$ ,  $C_{X\theta}$ ,  $C_X^2$ ,  $C_X^3$ ,  $C_X C_\tau$ ,  $C_{X\theta} C_X$ ,  $C_\theta^2$  and  $C_\theta C_X^2$  are equated to zero, we obtain the following set of overdetermined partial differential equations:

$$-\frac{\eta}{2\theta} + \frac{\delta_C}{2} - \frac{\eta_\theta}{2} + K \eta_X + \frac{1}{2}(2\xi_X - \delta_C) + \theta \eta_{XX} = 0$$

$$\frac{K\eta}{\theta} - \frac{1}{2}\xi_\theta - K(\delta_C - \xi_X) - K(2\xi_X - \delta_C) - \theta(2\delta_{XC} - \xi_{XX}) = 0$$

$$\frac{1}{2}\xi_C + \frac{3}{2}\xi_C - 2\eta_{XC} = 0$$

$$2K\xi_C + \theta(\delta_{CC} - 2\xi_{XC}) = 0$$

$$2\theta\eta_x = 0$$

$$2\theta\eta_c = 0$$

$$\theta\xi_{cc} = 0$$

$$\eta_c = 0$$

$$\eta_{cc} = 0$$

$$\frac{1}{2} \delta_\theta - K\delta_x - \theta\delta_{xx} = 0$$

This system of group determining equations were solved for the coordinate functions  $\xi$ ,  $\eta$  and  $\delta$ . The solution yields the following four-parameter group generator:

$$U = (C_3x + C_4) \frac{\partial}{\partial x} + C_3\theta \frac{\partial}{\partial \theta} + (C_1C + C_2) \frac{\partial}{\partial C}$$

which decomposes into the following four generators:

$$U_1 = \frac{\partial}{\partial C}$$

$$U_2 = C \frac{\partial}{\partial C}$$

$$U_3 = \frac{\partial}{\partial x}$$

$$U_4 = x \frac{\partial}{\partial x} + \theta \frac{\partial}{\partial \theta}$$

The group  $U_4$  yields the widely used similarity variable  $x/\theta$ , i.e.  $x\sqrt{t}$ . However this similarity variable does not leave the interface condition (6c) invariant. To obtain a set of similarity variables that will be admitted by the Eq. (5) as well as by the initial and boundary conditions (6a-c) we observe that a linear combination of Lie groups of a differential equation is also a group for the differential equation.

So, we combine  $U_2$  and  $U_4$  to obtain

$$U_5 = x \frac{\partial}{\partial x} + \theta \frac{\partial}{\partial \theta} - nC \frac{\partial}{\partial C}, \quad n = 0, 1, 2, \dots, \infty$$

which yields  $x\sqrt{t}$  and  $C(\sqrt{t})^n/A_n$  as similarity variables. Here  $A_n$  is an arbitrary constant.

## APPENDIX B

The Eq. (15) is a linear second order ordinary differential equation with variable coefficient. Exact analytical solution for this equation for different values of  $n$  can be obtained as follows:

Letting  $\gamma = (\gamma + 2\gamma/\alpha_3)/\sqrt{20}$ , the Eq. (15) can be written as

$$\frac{d^2\psi_n}{dr^2} + r \frac{d\psi_n}{dr} + n \psi_n = 0, \quad n = 0, 1, 2, \dots, \infty \quad (B.1)$$

For  $n = 0$ , we have

$$\frac{d^2\psi_0}{dr^2} + r \frac{d\psi_0}{dr} = 0 \quad (B.2)$$

and its solution can be easily found.

For  $n = 1$ , we have

$$\frac{d^2\psi_1}{dr^2} + r \frac{d\psi_1}{dr} + \psi_1 = 0 \quad (B.3)$$

which can be written as

$$\frac{d}{dr} \left( \frac{d\psi_1}{dr} \right) + \frac{d}{dr} (r \psi_1) = 0$$

for which the solution is

$$\psi_1(r) = [H_1 + F_1 \int_{r_0}^r e^{\beta^2/2} d\beta] e^{-r^2/2}$$

where  $H_1$  and  $F_1$  are two arbitrary constants.

For  $n = 2$ , we have

$$\frac{d^2 \psi_2}{dr^2} + r \frac{d\psi_2}{dr} + 2 \psi_2 = 0 \quad (\text{B.4})$$

To solve this equation we first differentiate (B.1) with respect to  $r$  to get

$$\frac{d^2 p}{dr^2} + r \frac{dp}{dr} + (n+1)p = 0 \quad (\text{B.5})$$

where

$$p = \frac{d\psi_n}{dr}$$

Now the Eqs. (B.4) and (B.5) are identical if  $\psi_2 = p$  and  $n = 1$ . So

$$\psi_2 = \frac{d\psi_1}{dr}$$

which can be determined from the solution  $\psi_1(r)$ . In this way the solutions of (B.1) can be obtained from

$$\psi_n(r) = \frac{d^{n-1} \psi_1}{dr^{n-1}} \text{ for } n \geq 2.$$

## LIST OF FIGURES

Figure 1(a) Schematic diagram of laser surface cladding  
(b) Three-dimensional view of the cladding and the substrate  
(c) Geometric configuration used in the present model. (The model substrate and the solidification of the model cladding have been shown after rotating the pool ABCA (see Fig. 1(a)) by 90 degrees clockwise)

Figure 2 Variation of cooling rate of the liquid phase with time at the freezing front

Figure 3 Effect of cooling rate on the composition of hafnium in the solid phase at the freezing front

Figure 4 Parametric dependence of the composition of hafnium in the solid phase at the freezing front at 0.2 sec. after solidification begins, on laser energy flux

Figure 5 Variation of hafnium composition at the freezing front in nickel-hafnium alloy relative to the cladding thickness at 0.2 sec. after solidification begins

Figure 6 Effect of cladding on the initial temperature of the cladding melt

Figure 7 Effect of initial temperature on the cooling rate at 0.2 sec after solidification begins for laser-cladding interaction time 0.24 sec

Figure 8 Effect of initial temperature on the cooling rate at 0.2 sec after solidification begins for laser-cladding interaction time 0.18 sec



Figure 9 Effect of initial temperature on the cooling rate  
at 0.2 sec after solidification begins for  
laser-cladding interaction time 0.14 sec

Figure 10 Microstructure of nickel-hafnium  
cladding on nickel substrate

Figure 11 Microstructure of nickel-aluminum  
cladding on nickel substrate

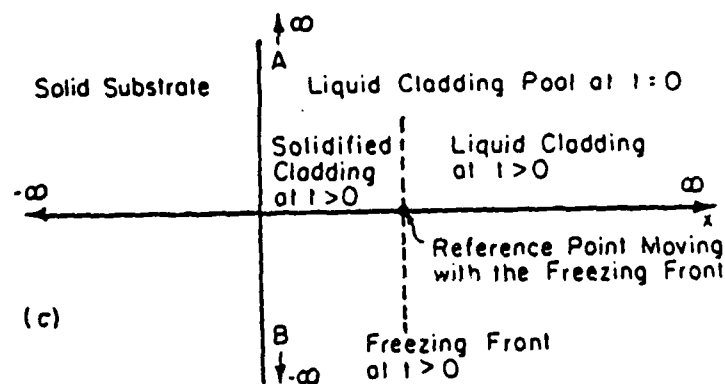
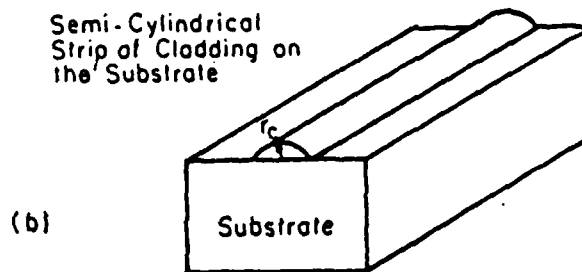
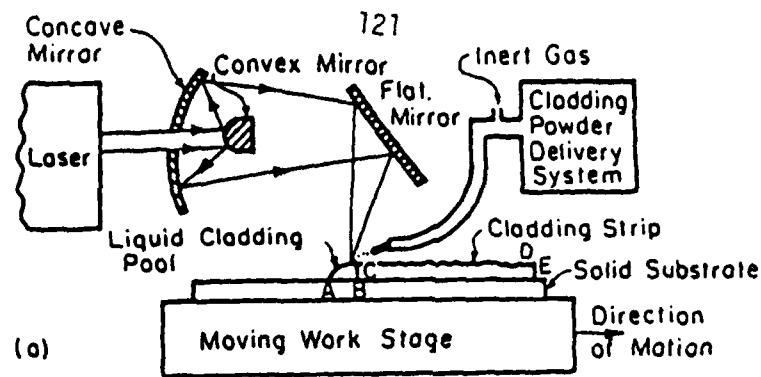


Figure 1(a) Schematic diagram of laser surface cladding

(b) Three-dimensional view of the cladding and the substrate

(c) Geometric configuration used in the present model. (The model substrate and the solidification of the model cladding have been shown after rotating the pool ABCA (see Fig. 1(a)) by 90 degrees clockwise)

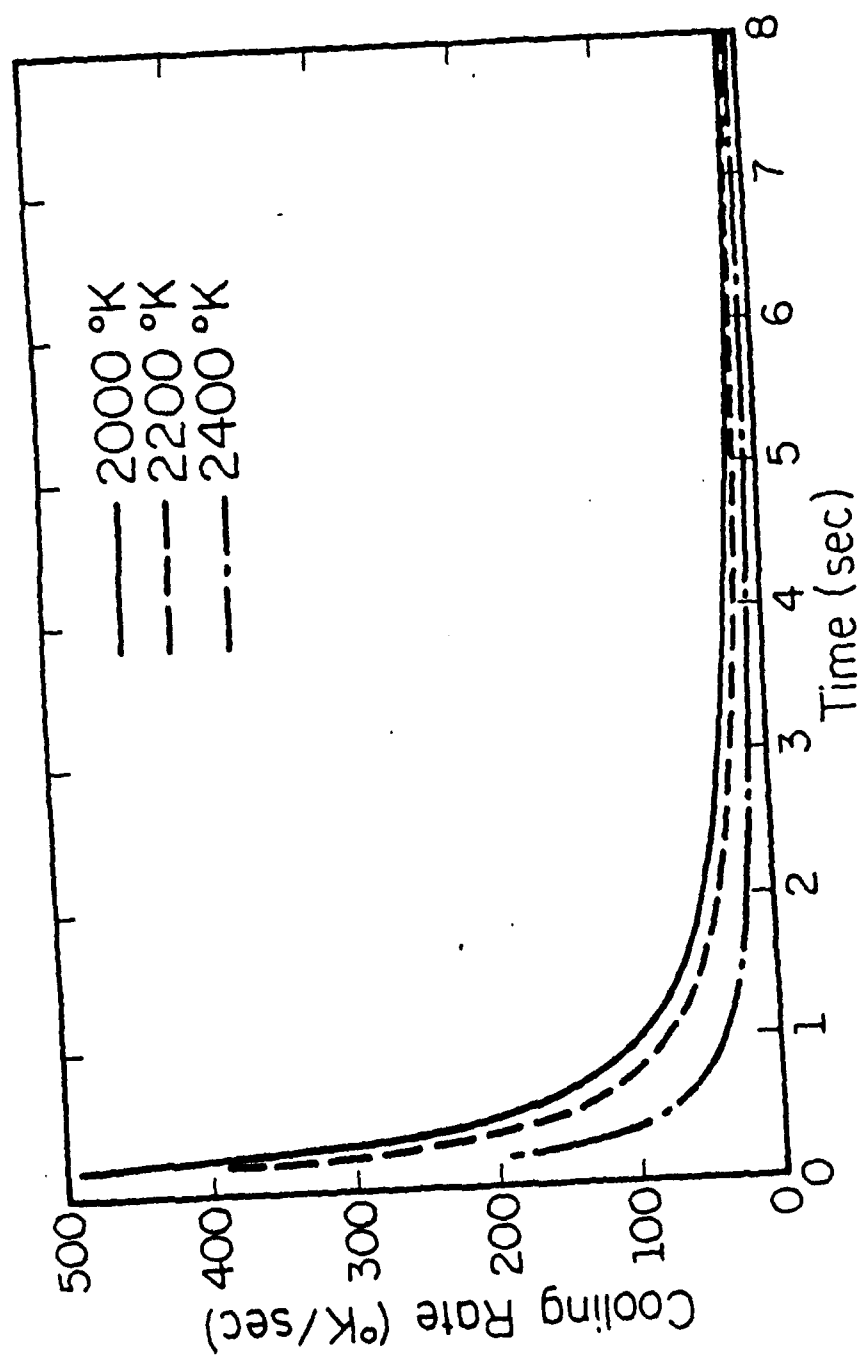


Figure 2 Variation of cooling rate of the liquid phase  
with time at the freezing front

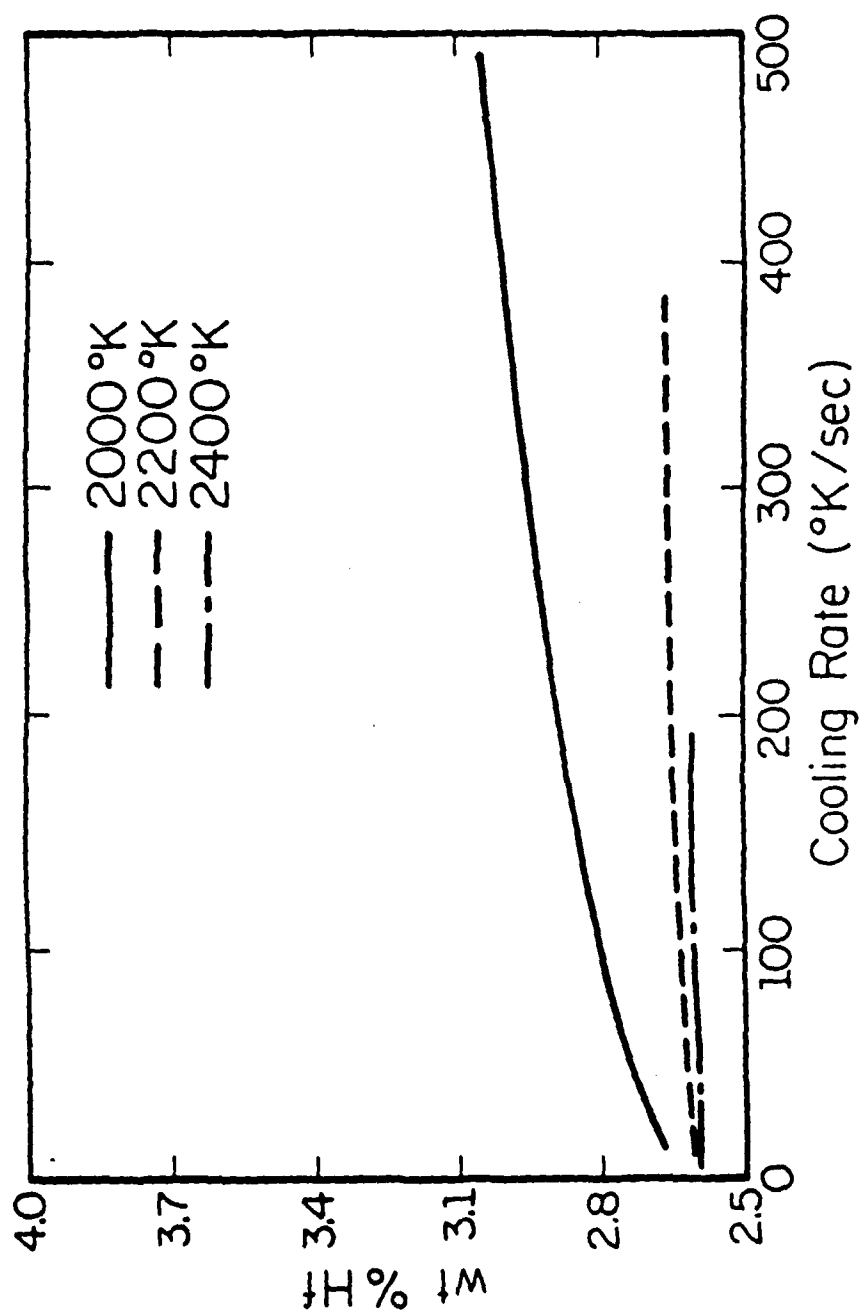


Figure 3 Effect of cooling rate on the composition of hafnium in the solid phase at the freezing front

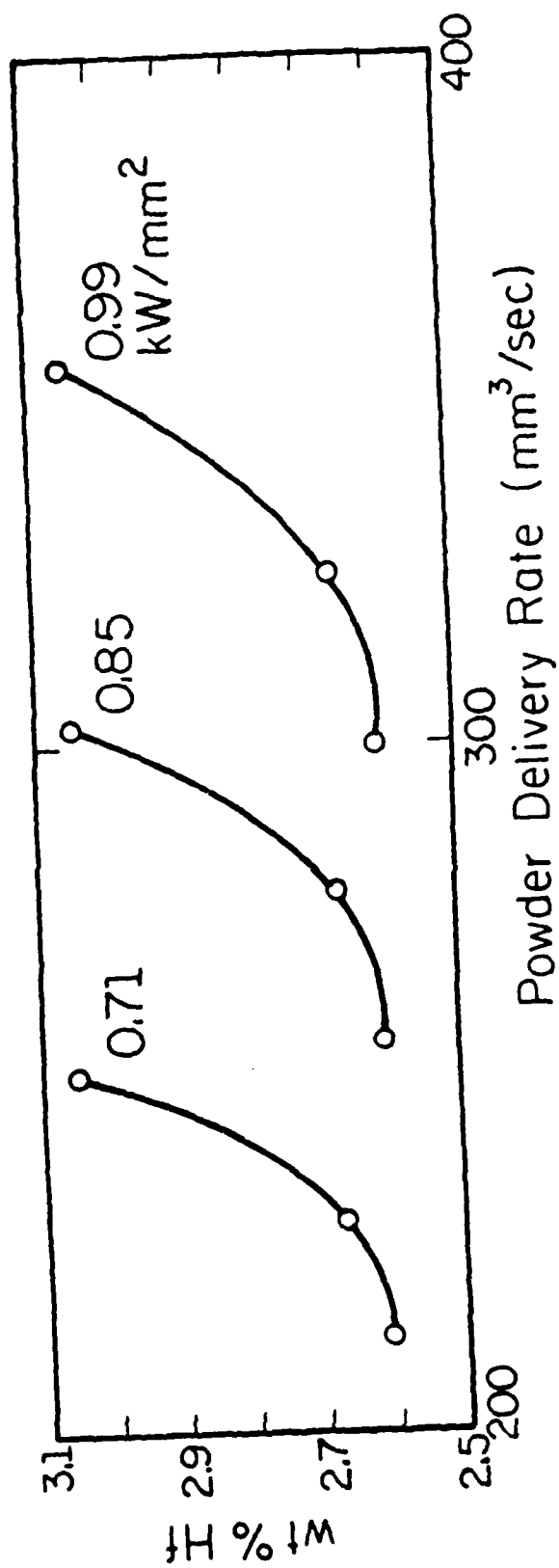


Figure 4 Parametric dependence of the composition of hafnium in the solid phase at the freezing front at 0.2 sec. after solidification begins, on laser energy flux

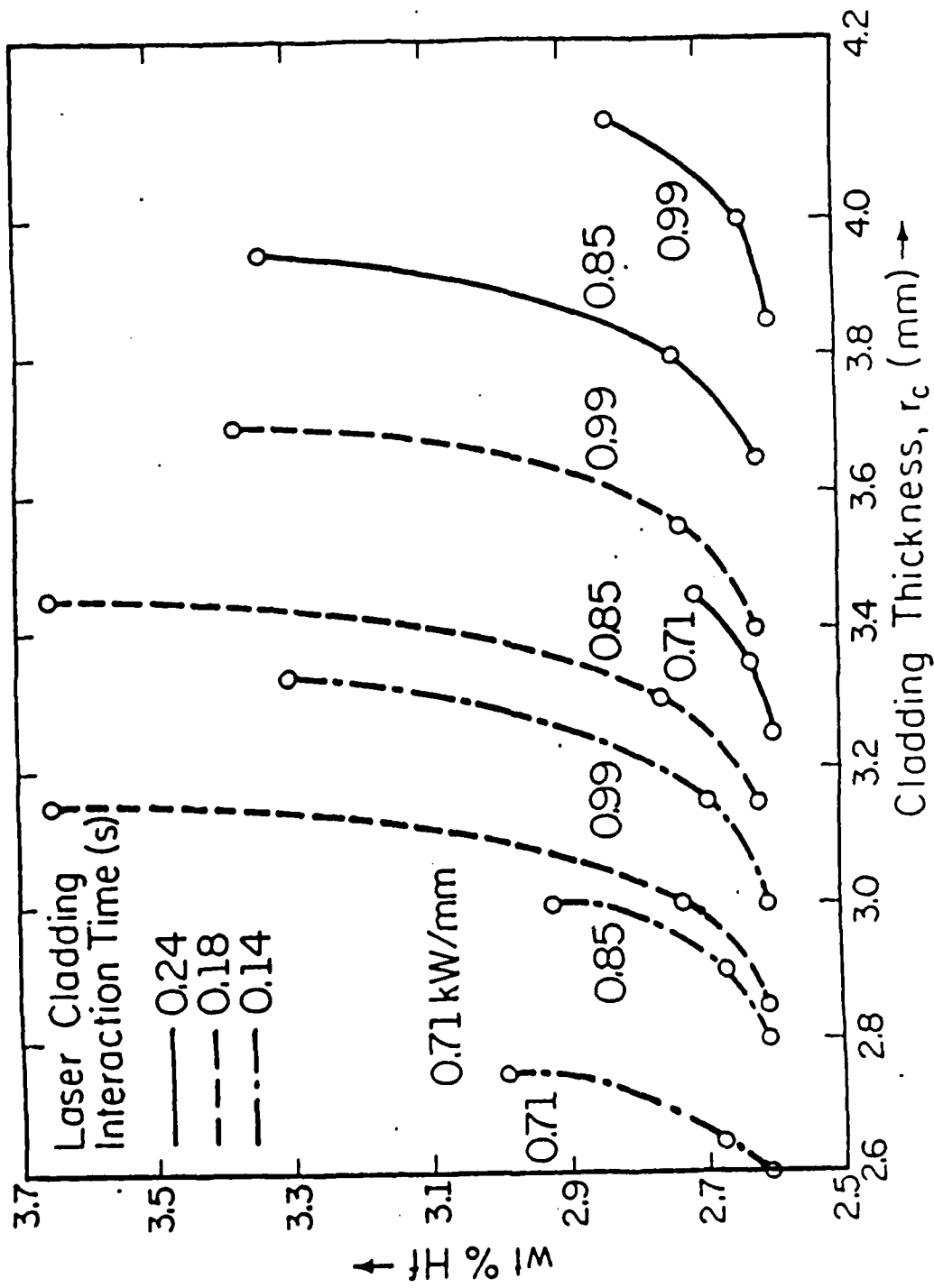


Figure 5 Variation of hafnium composition at the freezing front in nickel-hafnium alloy relative to the cladding thickness at 0.2 sec. after solidification begins

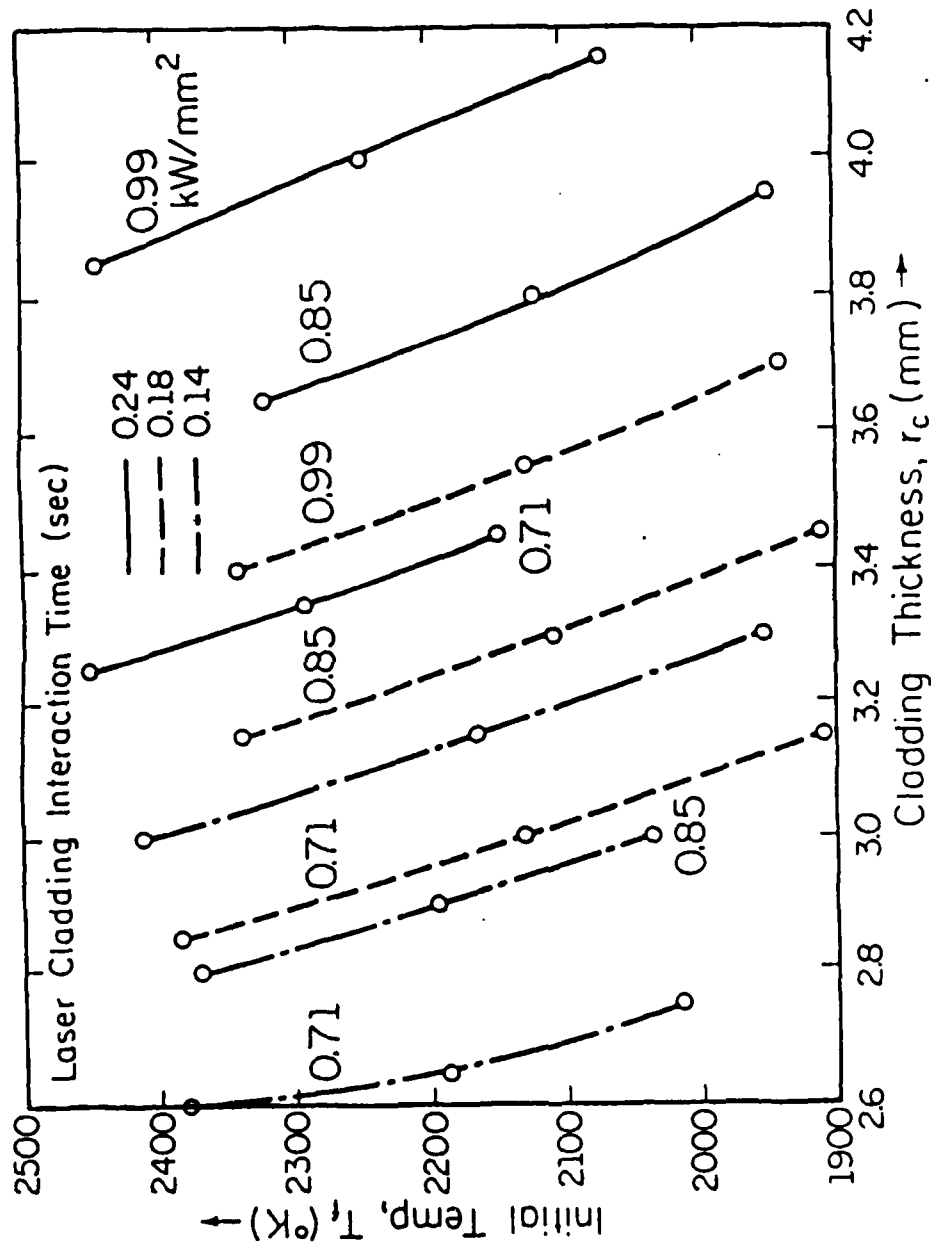


Figure 6 Effect of cladding on the initial temperature of the cladding melt

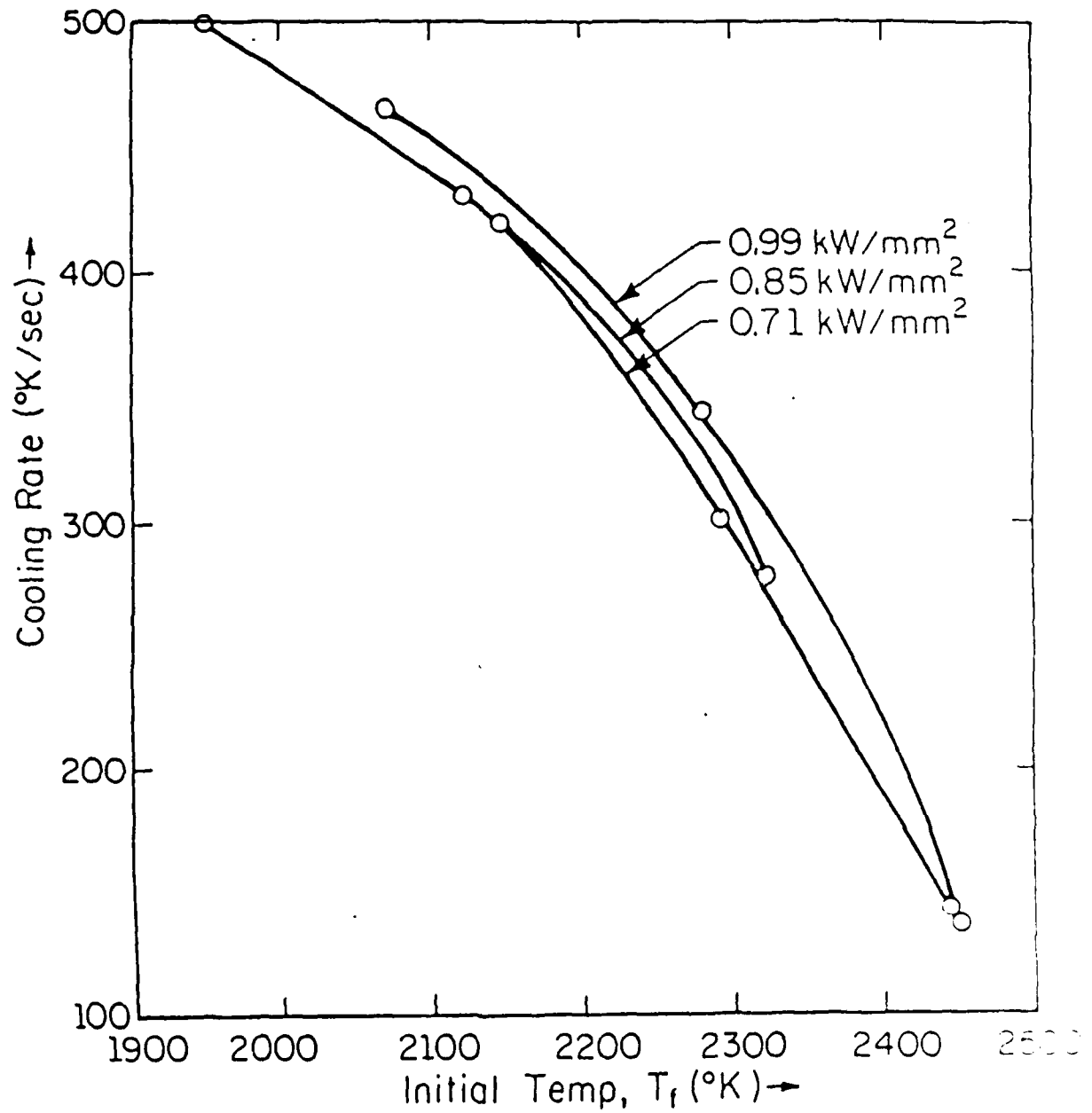


Figure 7 Effect of initial temperature on the cooling rate at 0.2 sec after solidification begins for laser-cladding interaction time 0.24 sec



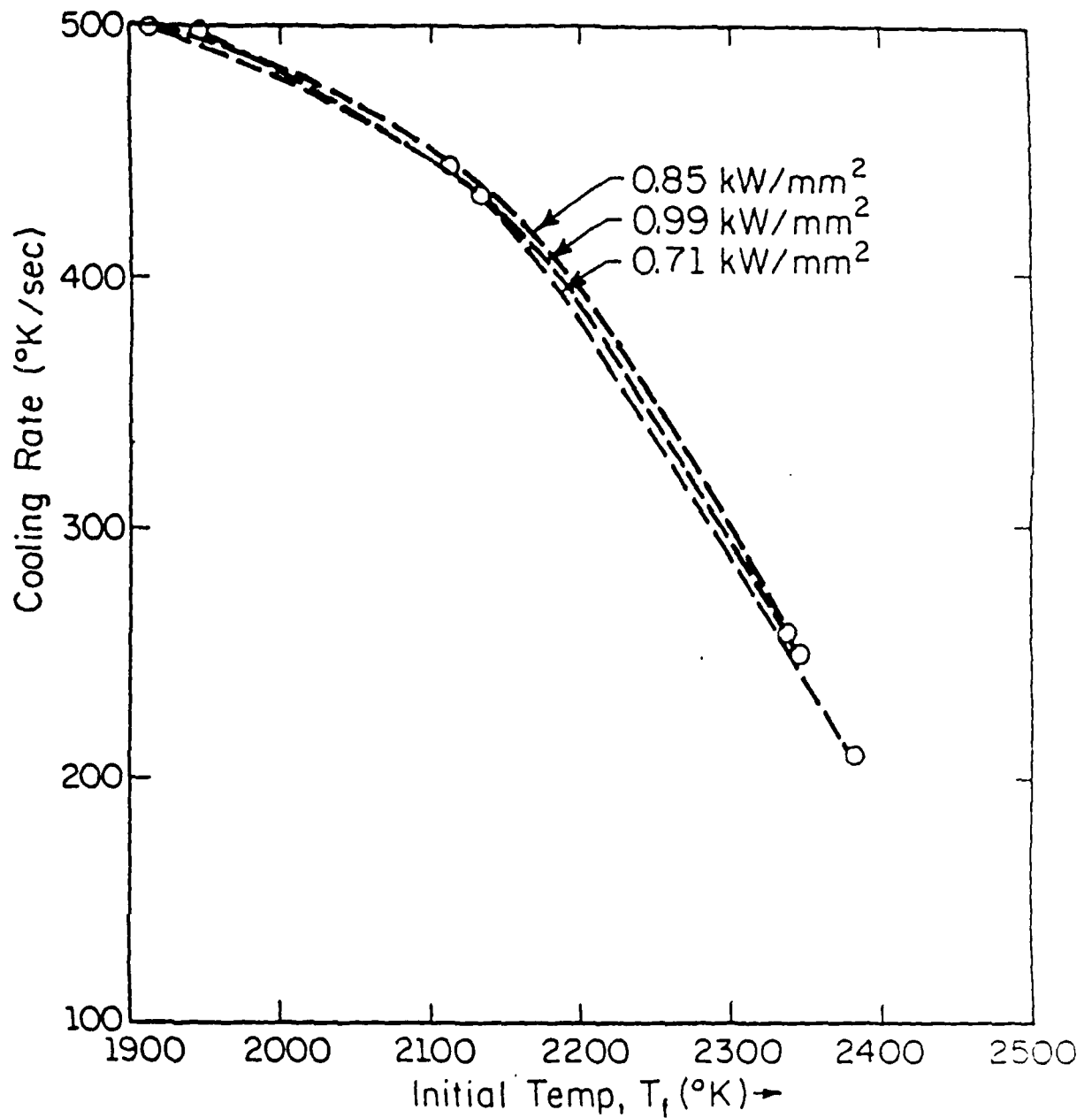


Figure 8 Effect of initial temperature on the cooling rate at 0.2 sec after solidification begins for laser-cladding interaction time 0.18 sec

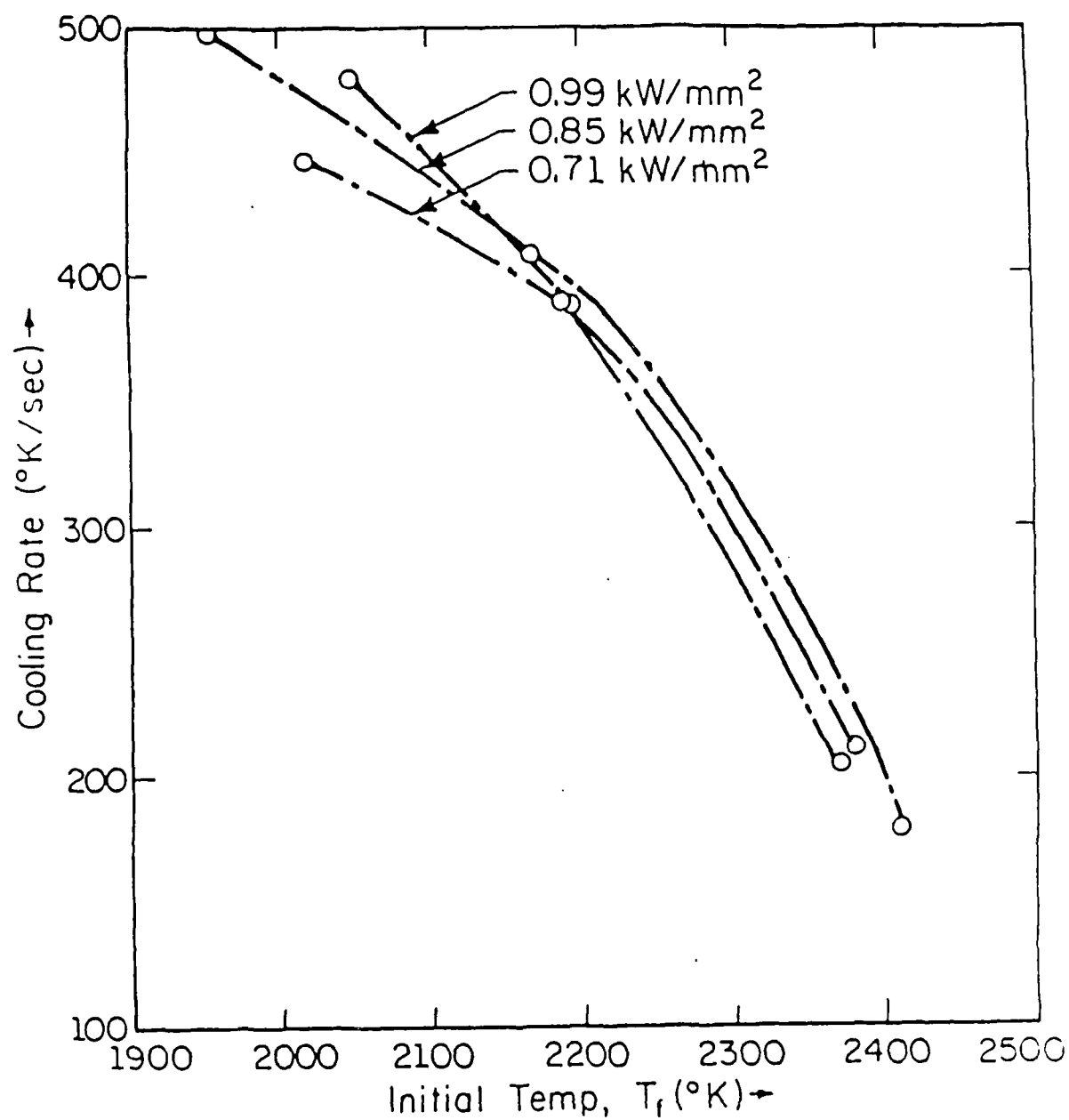


Figure 9 Effect of initial temperature on the cooling rate at 0.2 sec after solidification begins for laser-cladding interaction time 0.14 sec

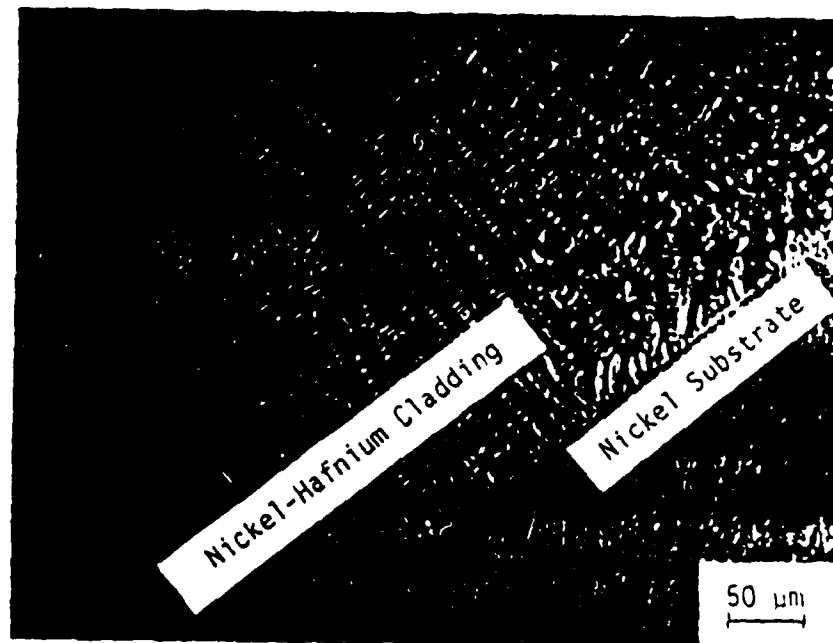


Figure 10 Microstructure of nickel-hafnium  
cladding on nickel substrate

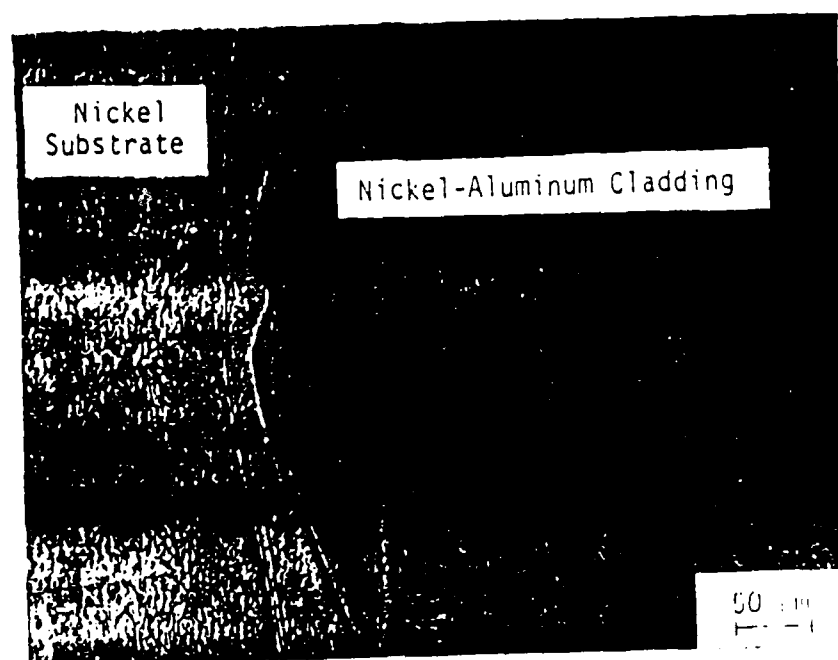


Figure 11 Microstructure of nickel-aluminum  
cladding on nickel substrate

END

5-87

DTic